MORPHOLOGICAL VARIABILITY ANALYSIS OF PHYSIOLOGIC WAVEFORM FOR PREDICTION AND DETECTION OF DISEASES

A Dissertation
Presented to
The Academic Faculty

By

Ismail Sadiq

In Partial Fulfillment
of the Requirements for the Degree
Doctor of Philosophy in the
School of Electrical and Computer Engineering
College of Engineering

Georgia Institute of Technology

December 2022

MORPHOLOGICAL VARIABILITY ANALYSIS OF PHYSIOLOGIC WAVEFORM FOR PREDICTION AND DETECTION OF DISEASES

Thesis committee:

Dr. Gari D. Clifford
Department of Biomedical Engineering
Georgia Institute of Technology and Emory University

Dr. Vince D. Calhoun
Department of Electrical and Computer Engineering
Georgia Institute of Technology

Dr. Omer T. Inan
Department of Electrical and Computer Engineering
Georgia Institute of Technology

Dr. A. Fatih Sarioglu
Department of Electrical and Computer Engineering
Georgia Institute of Technology

Dr. David V. Anderson
Department of Electrical and Computer Engineering
Georgia Institute of Technology

Dr. Aris P. Georgakakos
Department of Civil and Environmental Engineering
Georgia Institute of Technology

Date approved: November 18, 2022

The scientific observer of nature is a kind of mystic seeker in the act of prayer.

Dr. Allama Muhammad Iqbal

For my parents, teachers and siblings.

ACKNOWLEDGMENTS

It has been a long and gruelling, yet gratifying, journey that has finally come to an end. I look back in amusement and jubilation at lessons I learned and roads traveled to arrive at this point. It has indeed been a very memorable experience and the final destination of graduating from one of the most prestigious institutions is truly humbling, I am grateful to everyone who helped along the way.

I would first like to thank my parents Aftab Sadiq and Rubina Yasmin, who always supported me and lead me by example. Both my parents are a cornerstone of integrity, intelligence and energy. I would like to thank my siblings Fatima Sadiq, Sulaiman Sadiq and Hamza Sadiq for always being there when I needed their support.

I would like to thank mentors, staff and colleagues at Georgia Tech and Emory.

- Dr. Gari D. Clifford for providing me with the opportunity to join his lab as a Ph.D. student. I deeply appreciate his support and guidance over the years.

- Dr. Amit J. Shah for valuable clinical insight into the research that was related to the individuals with post-traumatic stress disorder.

- Dr. Matthew E. Oster for valuable clinical insight into the research that was related to the neonates with coarctation of the aorta.

- Dr. Omer T. Inan, Dr. David V. Anderson, Dr. Vince D. Calhoun, Dr. A. Fatih Sarioglu and Dr. Aris P. Georgakakos for their valuable feedback and guidance on my research work.

- Dr. Qiao Li, Dr. Shamim Nemati, Dr. Ali Bahrami Rad, Dr. Reza Sameni and Dr. Guilia Da Poian for generously giving their time for the useful discussions we had and the feedback they provided on my research work.

- To my lab members Camilo Valderrama, Mohsin Salari, Nick Shu, Zifan Jiang, Shafaat Shiekh, Samuel Waters, Pradyumna Suresha and Ayse Cakmak.

I would next like to thank all the teachers for their support. Dr. Shoab Khan for his guidance and mentoring while I worked at the Center for Advanced Research in Engineering. I would also like acknowledge Mr. Inayat Malik and Mr. Asim Rasheed, who instilled self-belief and motivation in me.

Finally I would like to thank the funding bodies for sponsoring the research presented in this thesis: The National Science Foundation (award 1636933), National Institute of Health/National Heart, Lung and Blood Institute (awards R01HL136205, K23HL127251, R01-HL109413-06 and R03HL146879) and the Orefice Family Foundation.

TABLE OF CONTENTS

LIST OF TABLES

LIST OF FIGURES

LIST OF ACRONYMS

ABP arterial blood pressure

Acc accuracy

ACS acute coronary syndrome

AF average rate of fall

ANS autonomic nervous system

AR average rate of rise

AUROC area under the receiver operating characteristic curve

BAcc balanced accuracy

BP blood pressure

bpm beats per minute

BR breathing rate

BW baseline wander

CAPS-5 clinician administered PTSD scale fifth edition

CHD coronary heart disease

CHF congestive heart failure

CHOA Children's Healthcare of Atlanta

COA coarctation of the aorta

CT computed tomography

CV cross validation

DBN deep belief network

DBP diastolic blood pressure

DCNN deep convolutional neural network

DSM-5 diagnostic statistical manual for mental disorders fifth edition

DTW dynamic time warping

ECG electrocardiogram

EM electrode movement

EMR electronic medical record

F1 F1-score

FDR false detection rate

GA Georgia

GRACE global registry of acute coronary events

HR heart rate

HRV heart rate variability

ICU intensive care unit

IRB institutional review board

LDA linear discriminant analysis

LOOT leave one out testing

LOS length of stay

MA muscle artifact

MAP mean arterial pressure

MEWS modified early warning system

MF maximum rate of fall

MMA modified moving average

MR maximum rate of rise

MV morphological variability

MVM morphological variability magnitude

NARV non-alternan repolarization variability

NN normal beat to normal beat

NPV negative predictive value

NSR normal sinus rhythm

NSTDB noise stress test database

PAT pulse arrival time

PCA principal component analysis

PCL-5 PTSD checklist-5

pctl percentile

PPG photoplethysmogram

PPV positive predictive value

PTBDB Physikalisch-Technische Bundesanstalt database

PTSD post traumatic stress disorder

RNN recurrent neural network

rpm respirations per minute

RR R peak to R peak

SBP systolic blood pressure

SIRS systemic inflammatory response syndrome

SM spectral method

SNR signal-to-noise ratio

SOFA sequential organ failure assessment

SQI signal quality index

TIMI thrombolysis in myocardial infarction

TWA T-wave alternan

VCG vector cardiogram

VET Vietnam era twins

SUMMARY

For many years it has been known that variability of the morphology of high-resolution ($\sim$30-1000 Hz) physiological time series data provides additional prognostic value over lower resolution ($\leq$ 1Hz) derived averages such as heart rate (HR), breathing rate (BR) and blood pressure (BP). However, the field has remained rather ad hoc, based on hand-crafted features.

Using a model-based approach we explore the nature of these features and their sensitivity to variabilities introduced by changes in both the sampling period (HR) and observational reference frame (through breathing). HR and BR are determined as having a statistically significant confounding effect on the morphological variability (MV) evaluated in high-resolution physiological time series data, thus an important gap is identified in previous studies that ignored the effects of HR and BR when measuring MV. We build a best-in-class open-source toolbox for exploring MV that accounts for the confounding factors of HR and BR. We demonstrate the toolbox's utility in three domains on three different signals: arterial BP in sepsis; photoplethysmogram in coarctation of the aorta; and electrocardiogram (ECG) in post-traumatic stress disorder (PTSD). In each of the three case studies, incorporating features that capture MV while controlling for BR and/or HR improved disease classification performance compared to previously established methods that used features from lower resolution time series data.

Using the PTSD example, we then introduce a deep learning approach that significantly improves our ability to identify the effects of PTSD on ECG morphology. In particular, we show that pre-training the algorithm on a database of over 70,000 ECGs containing a set of 25 rhythms, allowed us to boost performance from an area under the receiver operating characteristic curve (AUROC) of 0.61 to 0.85. This novel approach to identifying morphology indicates that there is much more to morphological variability during stressful PTSD-related events than the simple periodic modulation of the T-wave amplitude. This

research indicates that future work should focus on identifying the etiology of the dynamic features in the ECG that provided such a large boost in performance, since this may reveal novel underlying mechanisms of the influence of PTSD on the myocardium.

CHAPTER 1
INTRODUCTION

1.1 Motivation

In modern medicine, the dynamics of medical data are rarely used, with static point-of-care values dominating diagnostics. Changes, rates of change, variances, or spans of data are considered. These are coarse statistical measures that do not consider time or consider it at very few points. A minority of studies had demonstrated utility in the dynamics of the variability of physiological waveform data over short-term time scales (minutes to hours), generally known as MV. However, most publications tended to limit studies to the ECG and no agreed standards existed for noise rejection, confounding repeat-ability.

Several studies used time-series data extracted from physiological signals for disease prediction [1, 2]. The time-series, sampled at 0.5 Hz for a few of the studies, were considered high-resolution in comparison to the frequency of standard patient readings acquired by clinicians for diagnosis. Similarly, studies measured variation in the instantaneous heart beat intervals to determine a state of disease. These time series measured variability over changes in intervals and statistics of variation were computed over longer windows e.g. 5-10 minutes [3, 4]. These previous approaches captured only a subset of information within the entire waveform signal.

This research aimed to measure beat to beat shape variability termed MV in physiological waveforms to classify individuals into diseased and non-diseased states. Moreover, the confounding effects of factors like heart rate and breathing rate were identified and mitigation strategies were provided. The physiological waveforms studied included the ECG, arterial blood pressure (ABP) and photoplethysmogram (PPG). These were typical waveforms encountered in standard patient care. An open-source toolbox was designed and

applied to 3 different medical problems, explained in the following paragraphs, to demonstrate the broad applicability of the technique.

Post-traumatic stress disorder is a chronic disabling psychiatric condition characterized by a persistent maladaptive reaction to the exposure to severe psychological stress, including re-experiencing trauma, hyper-vigilance, and hyper-arousal [5, 6, 7, 8]. The MV in the ECG was analyzed for individuals with a history of PTSD and controls. PTSD is a risk factor for adverse cardiovascular and metabolic changes. PTSD patients have been reported to have an increased risk of hypertension, hyperlipidaemia, obesity and cardiovascular disease. Chronic stressors over a long duration of time lead to increased neuroendocrine response which adversely effects the body. The mechanisms responsible for the link of PTSD to cardiovascular disease are dysregulated autonomic response through sympatho-adrenal medulary axis resulting in catecholamine release and disrupted hypothalamo pituauitary aderanal axis. Repeated sympathetic system response eventually affects cardiovascular health [9]. This results in myocardial electrical instability which can progress to arrhythmias and reduce heart rate variability and baroreflex functions, aggravating risk for cardiac events [10]. Controlled experiments measuring MV of an ECG demonstrated a significant increase in cardiac electrical instability in a state of elevated stress compared to a baseline state [11, 12]. Recently deep learning models have matched or outperformed human experts for disease detection [13, 14]. The utility of a novel approach for training a deep learning model on ECG waveform signals for detecting PTSD was evaluated.

Sepsis is defined as a life-threatening organ dysfunction caused by a dysregulated host response to infection. Sepsis onset is considered to be associated with a drop in systolic and mean arterial blood pressure [15]. The MV of ABP was analyzed in a cohort of individuals admitted to an intensive care unit (ICU) that did or did not develop sepsis. Previous studies had not considered MV of ABP as a predictor of sepsis onset, thus motivating the analysis to determine an association of changes in MV of ABP waveform with sepsis onset in an individual.

Coarctation of the aorta (COA) is a congenital narrowing of the descending aorta that restricts blood supply to the lower half of the body, figure 2.7, possibly leading to cardiac shock resulting in death. The MV of PPG waveforms was measured between PPG waveform signals acquired from an upper extremity compared to a lower extremity, in a cohort of neonates with or without COA. Studies suggested a pressure gradient in blood pressure between the upper and lower extremities could be used to detect COA [16]. Similarly the maximum blood flow rate in the descending aorta was determined to be lower than the ascending aorta [17]. Furthermore, PPG signals were used to reliably measure the dynamics of blood flow [18].

1.2 Objectives and outline of the thesis

The research objective was to develop a standardized set of algorithms for measuring MV of physiological waveforms and demonstrate their utility on problems belonging to different medical domains. Furthermore, each problem involved measuring variability in a different signal modality demonstrating the broad applicability of the algorithms. The confounding effects of HR and BR were determined when measuring MV in the waveform of ECG signals, mitigation strategies were suggested. Previous studies had completely ignored these factors when measuring MV; therefore, we identified a significant gap in previous literature. Additionally, current methods for evaluating MV were mainly limited to ECG. No standardized methods existed for measuring MV or performing the necessary pre-processing steps, e.g., noise removal/noise rejection in noisy segments of the waveform data. The algorithms were distributed as part of an open-source toolbox [3], so other researchers may use and adopt them as a standard. Specifically, the utility of the algorithm was demonstrated in the following domains. First, identification of individuals with a history of PTSD and controls by measuring morphological variability in ECG waveform. Second, predicting sepsis onset by measuring morphological variability in ABP waveform from individuals admitted to the ICU. Third, detection of COA in a neonate population by

measuring morphological variability in a PPG signal waveform.

The outline of the thesis is as follows.

- Chapter 1 introduces the research area, cites limitations of current analysis methods and provides motivation for the proposed research.
- Chapter 2 covers the clinical background information relevant to the research domain.
- Chapter 3 provides a review of the literature associated with the research domain.
- Chapter 4 explains the methods used for measuring MV in the physiological waveform data and variability in time-series data.
- Chapter 5 describes the analysis performed to determine the HR and BR combinations that significantly confounded MV measured in physiological signals. The mitigation strategies for dealing with these factors are also examined. MV of ECG was computed on a group of individuals with and without a history of PTSD. Evaluation of MV was followed by classification of PTSD status using MV features, before and after accounting for the effects HR and BR.
- Chapter 6 applied the MV algorithm to ECG data to identify individuals with and without a history of PTSD. The MV features were used in addition to heart rate variability (HRV) [3] features, known to be associated with PTSD, to determine if MV features added predictive value to the PTSD classification task.
- Chapter 7 discusses application of the MV algorithm to measure variability in ABP waveform to predict sepsis onset in a retrospective group of individuals that developed sepsis while admitted to the ICU.
- Chapter 8 discusses how MV of the PPG waveform was used to detect COA in a population of neonates.

- Chapter 9 demonstrates a novel deep learning approach for classifying individuals with and without a history of PTSD. The approach was compared to the classification of PTSD status using a hand-crafted feature of T-wave alternans (TWA) [19].

- Chapter 10 concluded the analyses performed in the thesis and mentioned future directions to extend the research topic.

1.3 Contributions

The contributions of the research are listed as follows:

- A novel class of algorithms for measuring MV in physiological waveform signals was developed. The technique was benchmarked on public ECG datasets including the normal sinus rhythm (NSR), congestive heart failure (CHF) and sudden cardiac death (SCD) databases on PhysioNet [20]. [This work appears in chapters 4 and 6. The work for chapter 4 was published in [21]]

- HR and BR were identified as confounding factors when evaluating a class of existing and developed cardiovascular MV metrics. [This work appears in chapter 5 and was published in [21]].

- The application of the MV algorithms on three distinct medical problems using different signal modalities was demonstrated, i.e. ECG, ABP and PPG. For each analysis, we demonstrated incorporating features extracted from waveform data improved classification results compared to previous studies. [The work appears in chapters 6, 7 and 8. The work for chapter 8 was published in [22]]

- A novel deep learning algorithm for measuring MV and detecting cardiac arrhythmia was developed. The deep learning algorithm was used to classify PTSD status with an AUROC of 0.85 by pre-training on large data set of ECGs annotated for normal sinus rhythm and cardiac arrhythmias. The result suggested pretraining a deep neural

network on data similar to target data improved classification performance. [The work appears in chapter 9. The pre-print may be viewed at [23].]

- An open-source toolbox to harmonize a class of morphological variability approaches was disseminated and confounding factors were identified. The toolbox may be used by other researchers and adopted as a standard for measuring MV in physiologic signal waveforms.

CHAPTER 2
CLINICAL BACKGROUND

The application of the algorithms for measuring MV of physiologic waveform signals was demonstrated on ECG for PTSD detection, ABP for prediction of sepsis onset and PPG for detecting COA. The following sections review the related background clinical knowledge relevant to each medical problem analyzed.

2.1 Analysis of electrocardiogram for PTSD detection

2.1.1 Post-traumatic stress disorder

PTSD is a psychiatric disorder occurring in normal individuals exposed to traumatic events over a long duration. Symptoms include guilt, reliving the trauma in dreams, numbness, lack of involvement with reality, or recurrent thoughts and images. PTSD may affect individuals of any ethnicity, age and gender. Females are twice more likely to be affected than men. In the US, 3.5% of the adult population was affected by PTSD. Furthermore, most individuals developed symptoms within three months; however, it may take longer. In some cases, the effects of PTSD subsided over time. Other individuals needed help from family, friends and clergy. Most required professional treatment in the form of group therapy or medication. Earlier treatment resulted in improved outcomes for patients [24]. Part of the objective of this current research was to use computational biomarkers that measured morphological variability of the ECG to detect PTSD.

Recent studies have shown PTSD as a risk factor for arrhythmogenesis in a group of war veterans [10, 25]. It was observed that heightened stress and emotion experienced by individuals with PTSD affected cardiac depolarization and repolarization cycles, manifesting as elevated MV of the ECG [26, 11, 12], which is predictive of cardiac arrhythmia.

Cardiac ventricular arrhythmias are one of the leading causes of mortality due to cardiac disease [27] . An important mitigation strategy was early detection so that timely preventive measures could be taken. A diverse amount of clinical information was also generally incorporated to aid in risk stratification after acute coronary syndrome (ACS). Risk scores like the Global Registry of Acute Coronary Events (GRACE) and Thrombolysis in Myocardial Infarction (TIMI) incorporated cardiac risk factors and biomarker data. However, these existing metrics only captured a subset of high-risk patients [28, 29]. There was a need to identify the significant number of patients who suffered from similar fatal arrhythmias leading to ACS but were not captured using existing metrics. Computational biomarkers measuring MV in ECG presented a solution [30].

2.1.2 Electrocardiogram

A heart consists of 4 chambers, two atria and two ventricles. Blood enters the heart through the atria and exits through the ventricles. Deoxygenated blood from the body enters the right atrium and oxygenated blood from the lungs enters from the left atrium. Blood passes through the right and left atria, entering the right and left ventricles. The flow of blood between the atria and ventricles is controlled by the atrioventricular valves, the pulmonary and aortic valves control the flow of blood as it exits through the ventricles. The right ventricle pumps blood to the lungs for oxygenation and the left ventricle pumps blood to the body. The structure of the heart is described in figure 2.1.

The electrical activity of the heart is described by an ECG. The heart comprises of muscle (myocardium) that periodically contracts (depolarizes), causing blood to circulate throughout the body. Each heartbeat cycle consists of systole and diastole. During systole, an electric current passes through the heart in a coordinated manner to cause an effective contraction, resulting in a measurable change in potential. An amplified recording of the change in potential is called an ECG. Each cardiac cycle is initiated by a mass of pacemaker cells in the SA node. The cells fire an electrical impulse that propagates through the

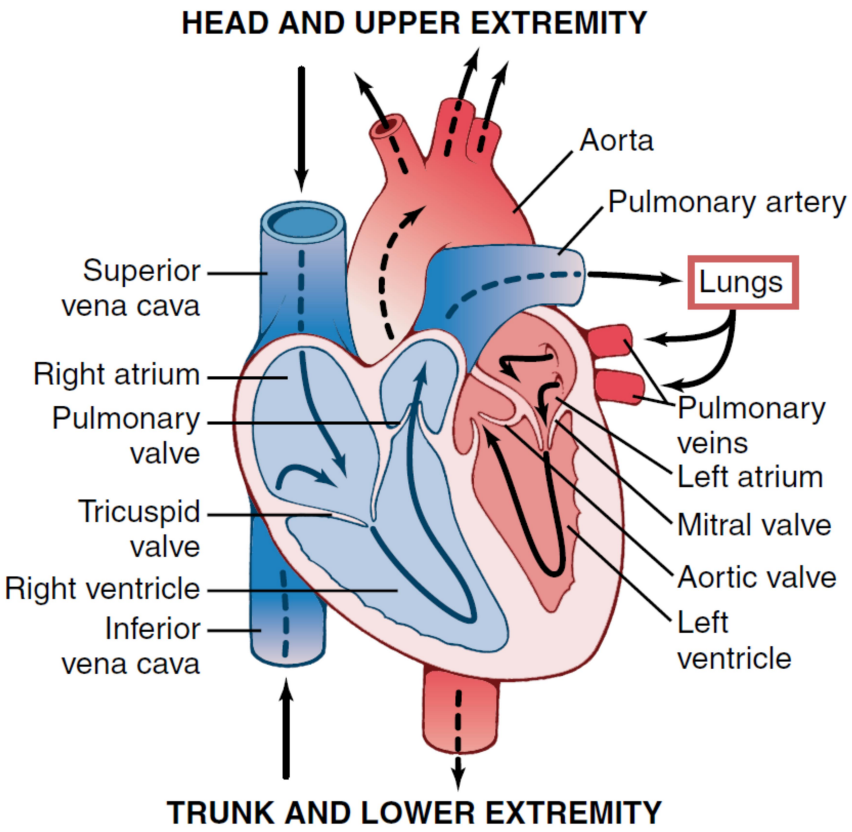

Figure 2.1: The structure of the heart, blood flow through the hearts chambers and valves is illustrated. The figure has been reprinted from [31] with permission.

conduction pathways in the heart during each beat. The impulse originates at the SA node and travels to the atrioventricular (A-V) node, where the impulse is delayed before passing into the ventricles through the A-V bundle. The impulse then passes through the left and right bundle branches of Purkinje fibers and is conducted to all parts of the ventricles, causing contraction. During ventricular contraction, the atria relax to their original state or repolarize. The cardiac cycle ends after the ventricles also have relaxed and repolarized. Figure 2.2 illustrates the pathways of the conduction system of the heart.

A typical ECG consists of a P wave, a QRS complex and a T wave, figure 2.3. The P wave is caused by atrial depolarization before contraction. The QRS complex is caused by ventricular depolarization and the T wave is caused by ventricular repolarization as the muscle recovers from depolarization. The wave for atrial repolarization is eclipsed by

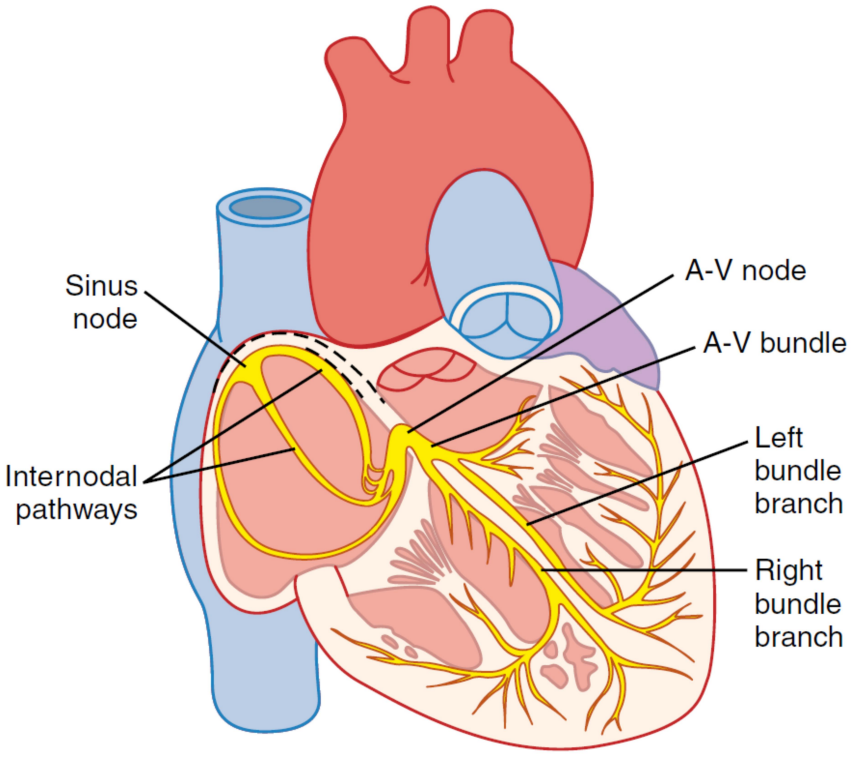

Figure 2.2: The electrical conduction pathways of the heart are illustrated. The figure was reprinted from [31] with permission.

ventricular depolarization. The interval between the end of the QRS complex (J point) and the end of the T wave is known as the ST-T segment and represents the ventricular repolarization activity of the heart.

The standard 12-lead ECG configuration is a combination of the following three lead configurations. The bipolar limb leads, labeled as I, II and III, are measured as the voltage difference between the left arm, right arm and left leg. See figure 2.4a. The augmented unipolar leads, denoted as aVF, aVL and aVR, are measured as the voltage difference between either the left arm, right arm, left leg and the average of the remaining two leads. The six precordial leads, labeled V1, V2,...V6, are positioned on the front and the left side of the chest and measured relative to a central terminal defined as the average of the voltages measured on the right arm, left arm and left leg. See figure 2.4b.

The Frank lead system [32] measures the heart's electrical activity in the orthogonal X, Y and Z directions. The electrical activity is measured using a linear combination of 7

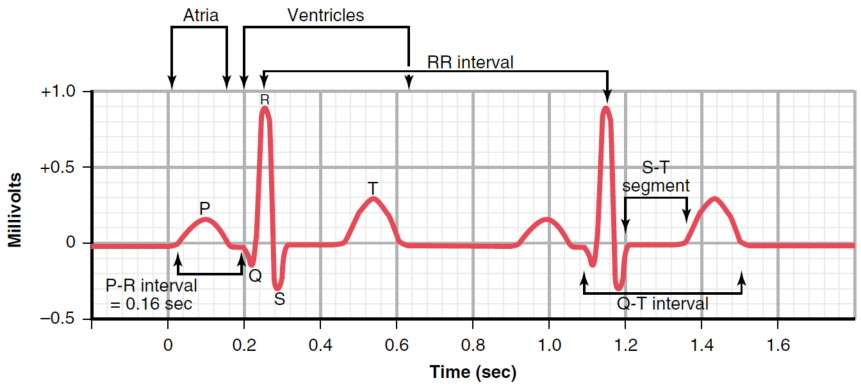

Figure 2.3: A typical ECG beat. The figure was reprinted from [31] with permission.

leads placed on the chest, back, neck and left ankle. The resulting X, Y and Z leads, termed the vectorcardiogram (VCG), provide a view of the heart's electrical activity from the left side, below and front side.

The polarity and morphology of individual ECG waves are dependent on electrode placement. An electrode will not capture an electrical wavefront traveling perpendicular to the direction of the vector defined by the lead. Additionally, the amplitude of a wave is dependant on the distance between the heart and the electrode.

2.2 Analysis of arterial blood pressure for prediction of sepsis onset

2.2.1 Sepsis

Sepsis is defined as a life-threatening organ dysfunction caused by a dysregulated host response to infection. The chemicals released from the immune system to fight an infection cause inflammation throughout the entire body resulting in injury to its tissue and organs. Patients in the ICU are more at risk of sepsis since they are already immunocompromised. Other individuals at risk of sepsis include older adults, pregnant women, children younger than 1 year of age, people who have chronic conditions such as diabetes, kidney or lung disease. Patients with sepsis experience a sudden drop in blood pressure before going into septic shock [15]. Early treatment of sepsis with antibiotics and intravenous fluids improves the chances of survival. Sepsis is globally considered to be a major cause of mortality. Over

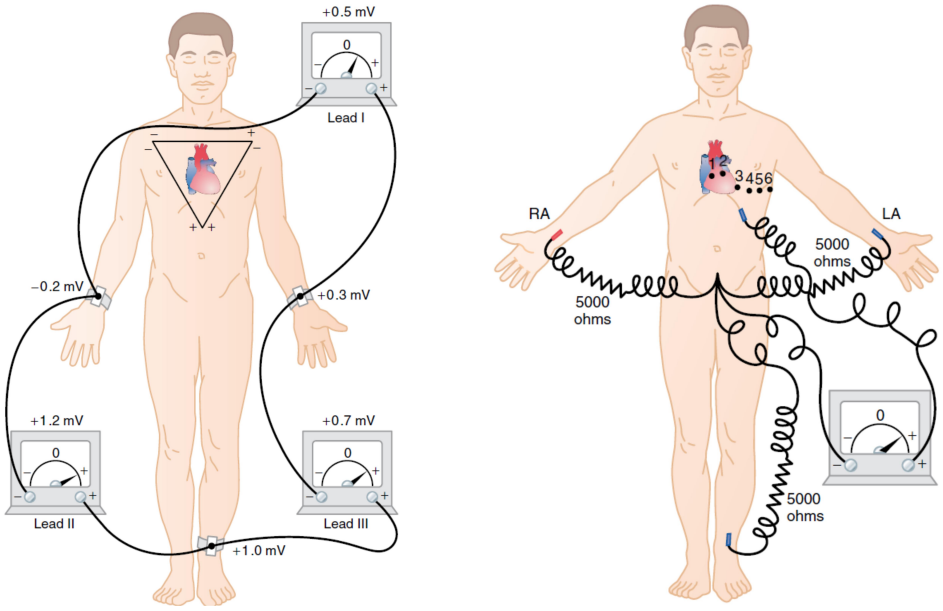

(a) (b)

Figure 2.4: **(a)** ECG electrode configuration for the limb leads. **(b)** ECG electrode configuration for the precordial leads. The figure was reprinted from [31] with permission.

700,000 people suffer from severe sepsis in the US alone, costing more than $20 billion in healthcare annually [33].

2.2.2 Arterial blood pressure waveform

Invasive arterial blood pressure is measured using an arterial blood pressure line. The setup consists of an arterial line placed in the arm connected by a non-compressible tubing filled with a saline solution to a pressure transducer. The transducer converts changes in pressure to electric signals displayed on a bedside monitor. The arterial line setup is displayed in figure 2.5.

A typical arterial blood pressure waveform is illustrated in figure 2.6 left. The wave starts at its nadir at the beginning of the systolic phase. The left ventricle ejects blood into the aorta causing aortic pressure to increase. The peak value is achieved at peak systole and is called systolic pressure. The pressure drops after peak systole, forming a dicrotic notch that indicates the closure of the aortic valve and the end of systole. During the diastolic

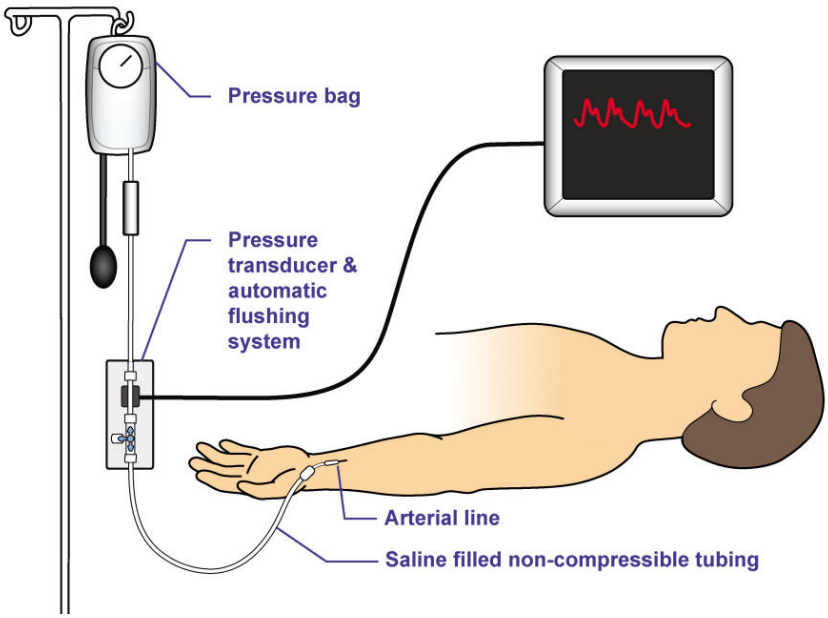

Figure 2.5: The setup for instrumentation used for measuring invasive arterial blood pressure is illustrated. The figure was reprinted from [34] and according to the copyright may be used for educational purposes.

phase, the ventricles relax and pressure continues to drop to a minimum value until the end of the cycle. The minimum pressure is achieved at the end of the diastolic phase before the ventricles are about to enter systole and is called the diastolic pressure. The normal value for systolic blood pressure is less than 120 mmHg and diastolic blood pressure is less than 80 mmHg. The mean arterial pressure is computed by integrating the area under the ABP wave for a cycle. The pulse pressure is defined as the difference between the systolic and diastolic pressures. Additionally, the HR can be computed by finding the difference between corresponding points in a cycle between successive waves. The breathing rate can be computed by measuring the pulse pressure variability.

Damping of the electrical signal affects the shape of the arterial blood pressure waveform. Underdamping overshoots the blood pressure and causes the systolic blood pressure to increase and the diastolic blood pressure to decrease, figure 2.6 right. Overdamping causes the systolic blood pressure to decrease and the diastolic blood pressure to increase, reducing the gap between the 2 pressure readings, figure 2.6 center. Overdamping is com-

monly caused by bubbles being present in the saline liquid or if a long compliant tubing is used.

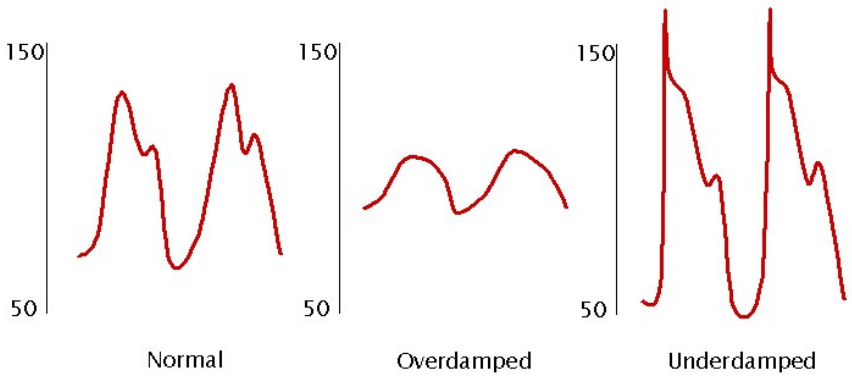

Figure 2.6: Left: Typical arterial blood pressure waveforms corresponding to 2 cardiac cycles. Center: overdamped ABP waves. Right: underdamped ABP waves. The figure was reproduced from [34] and may be used for non-commercial or educational purposes.

2.3 Analysis of photoplethysmogram for detection of coarctation of the aorta

2.3.1 Coarctation of the aorta

COA is a congenital narrowing of the descending aorta that supplies blood to the lower half of the body, figure 2.7. It can be mild or severe; mild cases might not be detected until adulthood. In severe cases, the heart must pump harder to force blood through the narrow part resulting in high blood pressure in the upper part of the body and heart damage. The neonate may develop CHF. COA is one of the most common congenital heart diseases and accounts for approximately 7% of all cases [35], each year 4 per 10,000 births [36] or approximately 1600 newborns are affected. Despite this prevalence, it frequently eludes detection in both the prenatal and neonatal periods [37]. Coarctation of the aorta remains challenging to diagnose before clinical deterioration. Despite current screening methods, infants with coarctation may present with life-threatening cardiogenic shock requiring urgent hospitalization and intervention. These infants are at high risk of mortality because

of the lack of a convenient screening test with high accuracy. Convenient procedures, e.g., cuff pressure measurement to establish a pressure difference between an upper and lower extremity, lack accuracy [38, 16, 39]. Procedures that have the desired level of accuracy, e.g. tracing blood flow using magnetic resonance imaging (MRI) [40, 41], are expensive and are not as readily available. Alternatively, PPG monitors are ubiquitous in any clinical environment. An accurate screening test using PPG with high sensitivity will significantly increase the survival rate of infants affected by COA.

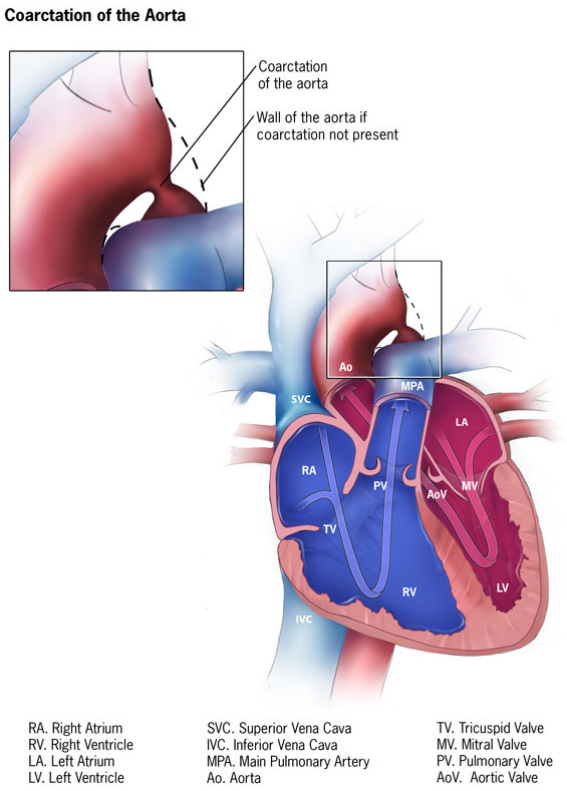

Figure 2.7: A coarctation in the descending aorta is illustrated. The figure was reprinted from the public domain at the CDC's Facts about Coarctation of the Aorta [36].

2.3.2 Photoplethysmogram

PPG uses an optical measurement technique to detect microvascular blood volume changes in tissues [42]. It has widespread clinical applications, such as in pulse oximeters, vascular diagnostics and digital beat-to-beat blood pressure measurement systems. The PPG sensor

comprises a light source to illuminate the tissue (e.g., skin) and a photodetector to measure the minute variations in light intensity caused by changes in perfusion in the catchment volume. PPG is mostly employed non-invasively and operates at a red or a near-infrared wavelength, figure 2.8.

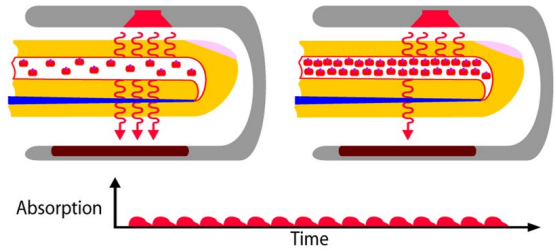

Figure 2.8: The mechanism for measuring PPG waveforms is illustrated. The figure was reproduced from www.howequipmentworks.com.

The depth to which light penetrates the tissue for a given intensity of optical radiation depends on the operating wavelength [43]. The main constituent of tissue is water that absorbs light very strongly in the ultraviolet and the longer infrared wavelengths. The shorter wavelengths of light are also strongly absorbed by melanin. There is, however, a window in the absorption spectra of water that allows visible (red) and near-infrared light to pass more easily, thereby facilitating the measurement of blood flow or volume at these wavelengths. Thus, the red or near-infrared wavelengths are often chosen for the PPG light source [44].

The most recognized waveform feature is the peripheral pulse, and it is synchronized to each heartbeat. The pulsatile component of the PPG waveform is often called the 'AC' component and usually has its fundamental frequency, typically around 1 Hz, depending on HR. This AC component is superimposed onto a large quasi-DC component that relates to the tissues and the average blood volume. This DC component varies slowly due to respiration, vasomotor activity and vasoconstrictor waves, Traube Hering Mayer (THM) waves and also thermoregulation. These characteristics are also body site-dependent [45]. With suitable electronic filtering and amplification both the AC and DC can be extracted for subsequent pulse wave analysis. Figure 2.9 shows the decomposition of a PPG wave-

form signal into AC and DC components. The pulsatile variation in the PPG signal is mainly attributed to changes in the arterial blood volume. For this reason, changes in the PPG waveform can be attributed to arterial blood flow. Aoyagi first measured PPG signals in their current form in 1972. Since then, a myriad of devices were developed which measure the oxygen saturation in blood, blood volume, and monitor other hemodynamic measurements like fluid responsiveness and BR [46].

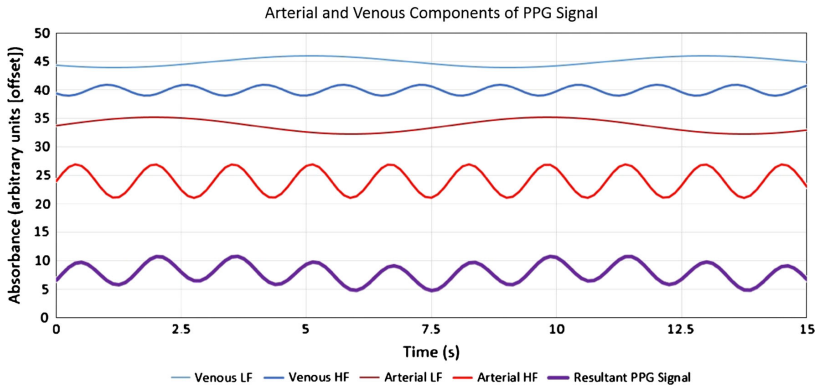

Figure 2.9: The decomposition of PPG waveform into its arterial and venous blood flow components. Reprinted by permission from Springer Nature Springer Nature, Canadian Journal of Anesthesia, Bartels *et al.* [47], © 2015.

CHAPTER 3
LITERATURE REVIEW

The literature review is organized as follows. Section 3.1 reviews literature on MV analysis of ECG and detection of PTSD. The ECG data was acquired from male veterans that served in Vietnam and did or did not develop PTSD. Section 3.2 reviews literature on clinical and computational methods that use features extracted from the ABP waveform to predict sepsis onset. To our knowledge, MV of the complete blood pressure waveform was not used for predicting sepsis onset. The data was obtained from bedside monitors or medical staff records for patients admitted to the ICU at Emory University Hospital, Atlanta, Georgia (GA) [2]. Section 3.3 reviews literature associated with the detection of coarctation of the aorta and analysis of PPG signals. The PPG signals were recorded from a neonate population admitted to the ICU at Children's Healthcare of Atlanta (CHOA). PPG signals were recorded from both an upper and lower limb for each neonate before corrective surgery.

3.1 Morphological variability of ECG in post-traumatic stress disorder

3.1.1 Cardiovascular disease

Ventricular arrhythmias caused SCD [27]. One mitigation strategy was early detection to take preventive measures promptly. Risk scores like the TIMI and GRACE incorporated cardiac risk factors and biomarker data [48, 49] but only captured a subset of subjects at medium to high risk of ACS and SCD. Current methods for identifying subjects at low to medium risk of heart disease were not very sensitive. Computational biomarkers provided a solution. Studies on MV of T waves were extensively documented in the literature. TWA or repolarization alternans are a phenomenon where T wave variability appeared in an every other beat pattern. Morphology changes like TWAs and ST-segment elevation were

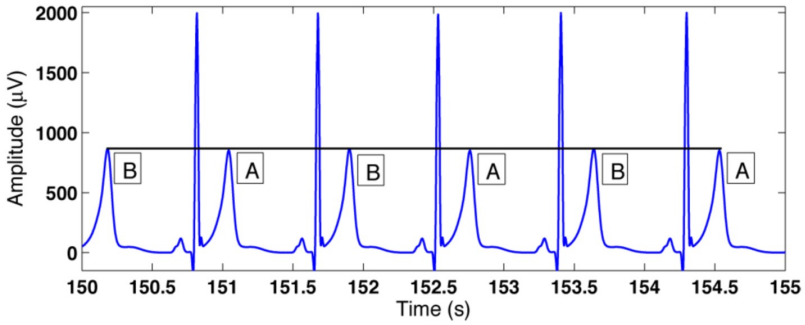

Figure 3.1: ECG with TWAs in a 'ABABAB...' pattern. The figure was reprinted from [52], © 2011 IEEE.

studied extensively to identify possible correlations with arrhythmia onset [50, 51]. Current methods for TWAs detection involved identifying changes in amplitude of adjacent T waves (in an 'ABABAB . . . ' pattern), figure 3.1.

TWAs were first observed at the beginning of the 20th century [53, 54], with interest continuing in the following decades [55, 56]. However, they were rarely observed until Adam *et al.* measured non-visible microvolt level changes in the T wave amplitude in the 1980s with the aid of computers [19]. Following this discovery, TWA patterns were observed more frequently and interest grew. Currently established methods for measuring TWAs included the modified moving average (MMA) method and the spectral method (SM) [57]. However, such techniques were susceptible to high false-positive detection since they did not incorporate robust noise rejection methods. Violeta *et al.* proposed a method that involved TWA detection using multiple leads [58]. The multiple leads provided added spatial information, i.e., the ECG was recorded from different leads giving information on the electrical conduction along different axes. The authors performed a periodic component analysis (πca) transformation, with a period of 2 beats, on the ECG leads to find projections that maximized the variability in the transformed signal with a period of 2 beats. The πca transformation facilitated TWA detection if TWAs were present. Also, the distribution of noise was modeled as Laplacian. Only TWA measurements that were comparably higher than a noise threshold were considered significant, thus reducing

the false positive detection rate. Nemati *et al.* developed a non-parametric surrogate-based statistical significance test that modeled the noise as a gamma distribution to determine a noise threshold [52]. TWA measurements above this threshold were considered statistically significantly higher than the baseline noise level. Nemec *et al.* detected T wave variability with a more complex pattern [59]. They quantitatively measured non-alternan variability (NARV) in T waves, which is variability in a non-alternating pattern or with a period greater than or equal to 2 beats. The authors quantified the maximum variability in the re-polarization segment of the ECG in a series of N consecutive beats. The process is illustrated in figure 3.2.

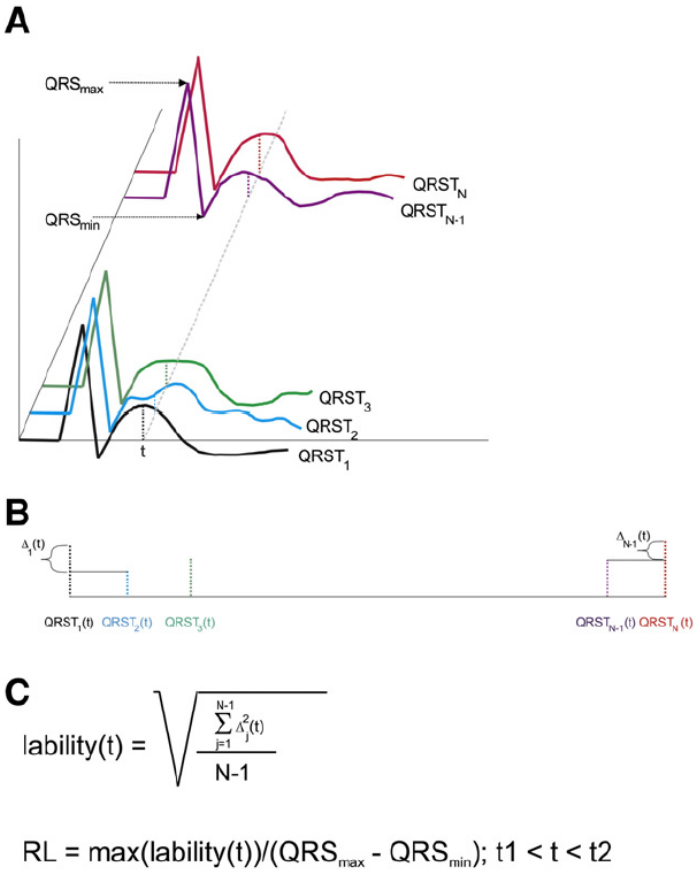

Figure 3.2: The process for measuring NARV is illustrated. The figure was reprinted from [59] © 2016, with permission from Elsevier.

In step A, the ST-T segments in N consecutive ECG beats were isolated and aligned. The maximum and minimum points of a QRS complex were detected to determine a nor-

malization factor. In step B, the difference in corresponding time instants was determined between consecutive beats and called $\Delta_i(t)$, the subscript i corresponded to the beat index. In step C, the RMS value of the differences in amplitude was computed for each time instant t and was referred to as 'lability'. The time instant with maximum lability was considered to represent maximum variability in the re-polarization segment. However, no form of noise rejection was mentioned to prevent measurements from segments affected by noise.

Other studies have investigated the surface ECG to measure ventricular re-polarization through variations in the T wave shape [60] and width [61]. Additionally, there was attention towards QRS morphological variability in terms of the de-polarization of the ECG [30, 63, 64, 65, 66, 67, 68, 69, 70, 62]. Liu *et al.* measured morphological variability in the complete ECG beat, including the QRS complex and T wave [30], with a period ranging from 2 to 7 beats over 24 hours. A few studies looked at the timing variability of the de-polarization plus re-polarization, i.e., the variability of the QT interval [26] and change in Tpe, the distance from QRS peak to the end of the T wave.

However, studies measuring ECG variability other than TWAs were limited. The study detailed in this thesis developed a generalized approach for measuring MV of the QRS complex, termed morphological variability magnitude (MVM). Unlike TWA detection, the MVM metric captured variability in non-binary sequences with a period greater than 2 beats.

3.1.2 Confounding factors

Elevated QRS morphological variability and TWA were predictors of heart failure [30, 71]. However, it is unclear whether the elevated changes in the MV of ECG were due to abnormalities in the heart's conduction system or are caused by the irregular breathing rates of the subjects. Cheyne-Stokes breathing is an abnormal breathing pattern that commonly occurs in patients with CHF [72]. It was well known that the amplitudes of each

component of the ECG change with breathing effort and non-stationary noise [73, 74]. Earlier works demonstrated that HR dependence at varying BR significantly affected TWA measurements, particularly in sleep, where breathing patterns were observed [75]. These HRs may have falsely triggered elevated TWA estimates any published noise thresholding approaches may not have rejected. It was unclear if these effects contributed to MV. In particular, periodic breathing that was approximately a multiple of HR may have caused elevated MV rather than abnormalities in the heart's conduction system. Previous studies had not considered this breathing-heart rate interaction effect as a confounding factor. The coupled effect of HR and BR may have led to an over-estimate of MVM and TWA, hence affecting the predictive value and clinical utility of these metrics. Supported by results in section 5.2.3A and section 5.2.3B, poor signal quality and high BRs, at various HRs will artificially inflate the quantification of MV in the signal.

Estimating the BR from physiological signals like ECG and PPG is well-studied. The established methods were extensively reviewed and benchmarked on simulated as well as ECG and PPG data acquired from real subjects [76]. BRs at particular HRs were more confounding to MV measurements. This was tested on synthetic ECG data based on real ECG morphologies at certain HRs and BRs [77, 78]. The synthetic ECG acted as a gold standard to determine HR/BR pairs for which the changes in morphology were statistically significant, compared to MV in an ECG signal free of respiratory effects. A non-parametric surrogate-based statistical significance test similar to [52] was used to determine HR/BR combinations for which MV changes in the signal with respiration were statistically significantly higher than MV changes measured in a signal without respiration effects.

3.1.3 Post-traumatic stress disorder

PTSD, a chronic disabling psychiatric condition, is a major problem amongst veterans, with a lifetime prevalence of 15 to 19%. In the United States, treatment costs were USD $8300 on average per veteran annually [79]. Early detection could lead to an early start in

the recovery cycle, delayed treatment of the disorder would prolong suffering and may reduce treatment efficacy [80]. Delaying treatment may also cause the symptoms to become worse and result in a poor quality of life [81]. Vaccarino *et al.* published a seminal study that established PTSD as an independent risk factor for subclinical and clinical coronary heart disease (CHD) [10]. The study performed by Vaccarino *et al.* used data from the Vietnam Era Twin Registry and conclusively showed there was little evidence suggesting factors other than PTSD, like shared environmental factors, adverse health behaviors and depression, had a causal effect on CHD. Moreover, the study showed PTSD was directly related to reduced heart perfusion, leading to CHD. In addition, Shah *et al.* found that PTSD was associated with autonomic inflexibility [25]. Shah *et al.* found individuals with PTSD had lower HRV compared to controls, consistent with other studies that showed low HRV due to PTSD was representative of heightened sympathetic and reduced parasympathetic activity [82, 83]. In particular, low-frequency heart rate variability (LF HRV), a marker of autonomic inflexibility and predictive of future death risk, was reduced by nearly 50% in those with PTSD versus controls. A major concern, based on these findings, was that PTSD could increase the risk of ventricular tachyarrhythmia and SCD through autonomic dysregulation [84]. The clinical implications for this could be large. Unfortunately, few studies investigated this.

Although most research was conducted on data from male veterans in the United States, recent studies examined a non-veteran population in Europe [85] and women [86]. Furthermore, some studies have shown that CHD caused by PTSD resulted in secondary PTSD in the same individual, in that they formed a closed reinforcement loop [87]. Therefore therapy for such individuals needed to be psychiatric as well as cardiovascular disease preventive [88].

Studies had also linked individuals with PTSD as having an increased resting HR compared to healthy individuals [89]. Reinertsen *et al.* used novel HRV to differentiate a cohort of individuals with PTSD from control individuals [4]. Studies that identified PTSD status

by measuring sleep quality through actigraphy demonstrated encouraging results [90, 91]. Incorporating HRV information in addition to actigraphy might lead to an improvement in accuracy for PTSD identification [92]. However, when using biometric data, almost all previous work focused on these heart rate dynamics as a proxy for sympathovagal stress [93]. A few studies analyzed speech [94] and skin conductance [95] to detect elevated stress.

In this study, we computed the MV of the QRS complex and T wave to identify cardiovascular stressors and used these, in addition to HRV features, to differentiate active or current PTSD individuals from recovered or past PTSD and control individuals. The motivation for this stemmed from the fact that increased stress levels were positively correlated with TWA amplitude and MV in the ECG beat with a period greater than 2 beats [11, 12]. Stress increased the catecholamine level, which had a direct sympathetic effect on the heartbeat and BR. This sympathetic response affected the ability of the sarcoplasmic reticulum to transport calcium ions, affecting the cycle of the ECG beat [96].

A. Machine learning for detecting post-traumatic stress disorder

In hospitals, PTSD assessments are performed as structured clinical interviews by experienced healthcare workers. The clinician-administered post-traumatic stress disorder scale (CAPS-5) is the gold standard for PTSD diagnosis and consists of a 30-item questionnaire that can take from 45-60 minutes to complete [97]. The CAPS-5 can be used to make a current PTSD diagnosis (past month), lifetime PTSD diagnosis (worst month) or a PTSD assessment over the past week, depending on the period for which the individual is examined. The response to each item on the questionnaire is noted as a severity score on a scale of 0-4. Zero corresponds to the absence of symptoms and four corresponds to the highest level of severity. The responses in the interview are highly subjective and can vary depending on the openness or consistency of the subject and the skill of the clinician/rater. The overall process of PTSD assessment is time-consuming and burdensome on the healthcare workers, aside from the existence of variability in the subject's responses or rater's skill in

administering the survey. Improving the screening test for PTSD with machine learning would reduce the burden on the healthcare providers and shorten the latency in the time to treatment for individuals who had PTSD.

Previous studies trained machine learning algorithms to learn to classify PTSD status from the responses for self-reported PTSD surveys. Wshah *et al.* [98] trained an ensemble of classifiers on a reduced set of responses from the PTSD checklist-5 (PCL-5) that were collected through smartphones. Ilhan *et al.* [99] used a similar approach of training a classifier on responses to a questionnaire similar to the PCL-5. The authors used feature selection to remove uninformative questions which improved classification performance. Jiang *et al.* [97] trained a random forest classifier on the responses to the 'self-administered interview for the DSM-5' (SCID-5), diagnostic statistical manual for mental disorders is abbreviated as DSM-5. They achieved an accuracy, a sensitivity, a specificity, a positive predictive value (PPV), a negative predictive value (NPV) and an AUROC, all above 0.9 using the top 14 response features determined using the Gini impurity [100]. The results suggested that structured interviews for PTSD screening could be abbreviated without losing accuracy, thus reducing the burden on clinicians.

The inter-subject variability in the responses to the questionnaire and inter-rater variability remained high, however. Other more objective features have been sought. Marmar *et al.* [101] extracted features from speech recorded from a group of veterans with or without PTSD to determine PTSD status. Speech signals were easily recorded and transmitted. The 18 most important features for PTSD classification were determined through 'shaving' and used to train a random forest classifier. Schultebrauks *et al.* [102] trained a deep belief network (DBN) on features extracted from audio and video recorded for individuals who had undergone a traumatic event and were being evaluated for PTSD.

3.2 Prediction of Sepsis by measuring morphological variability of ABP

Sepsis is a potentially life-threatening complication of an infection. Without rapid diagnosis and treatment, it can lead to multiorgan failure and death. The onset is difficult to diagnose as the signs and symptoms are subtle and subclinical. Furthermore, evidence suggests that every hour of delayed treatment can contribute up to an 8% chance of mortality in adults [103]. This highlighted the importance of early diagnosis and treatment, thereby decreasing sepsis-related morbidity and mortality.

The clinical gold standard for detecting sepsis included the systemic inflammatory response syndrome (SIRS) [104], modified early warning system (MEWS) [105] and sequential organ failure assessment (SOFA) [106] scores. Each of these scores was used to track infection by monitoring changes in patient vitals, routinely monitored as part of a patient's electronic medical records (EMR). According to a new Sepsis-3 definition introduced in 2016 by Singer *et al.* [15], patients were suspected of having an infection if they met two or more of the SIRS conditions. Singer *et al.* validated their definition with clinical trials using 1.3 million encounters. The validation study results may be considered too general and lack the resolution and accuracy to make effective predictions on a personalized basis. Incorporating clinical information obtained at a higher resolution in the prediction process may lead to improved prediction accuracy.

Recently machine learning algorithms, including deep neural networks, outperformed the clinical gold standard for sepsis prediction [107, 108]. Tracking a large number of features simultaneously enabled machine learning algorithms to identify more complex cases of sepsis. Nemati *et al.* used high-resolution HR and BP time-series data and information from EMRs to predict sepsis onset [109]. Mayaud *et al.* used the entropy of the HR in their sepsis prediction model [110]. Kamaleswaran *et al.* [1] and Van Wyk *et al.* [111] trained their sepsis prediction models using statistical features extracted from time-series data for HR, systolic blood pressure (SBP), diastolic blood pressure (DBP), mean arterial blood

pressure (MAP), BR and peripheral oxygen saturation (SpO_2), in addition to white blood cell count. The time-series data were sampled at 1-minute intervals. Shashikumar *et al.* computed entropy-based features from the MAP time series [2]. Using only entropy-based features from the MAP and HR time series, the authors achieved an out-of-sample AUROC of 0.67, classifying septic patients from the control group. However, no clinically validated system existed, which accurately predicted the real-time onset of sepsis in adults admitted to the ICU.

In contrast to previous studies and motivated by the work of Liu *et al.* [30], this study aimed at determining if beat-to-beat variation in the morphology of the ABP waveform was predictive of sepsis onset. Liu *et al.* showed that increased MV of the ECG was predictive of ACS in low to moderate risk patients. To our knowledge, MV of the complete ABP waveform was not considered a possible feature in a previous studies and may add predictive value. Hypotension was known to be associated with sepsis [112]. This research benchmarked MV of blood pressure to transient hypotensive event detection when predicting sepsis onset.

3.3 Morphological variability of PPG in coarctation of the aorta

Pulse oximetry analysis from different extremities is performed on neonates to identify critical congenital heart disease (CCHD) [113]. Newborns are screened for CCHD by detecting hypoxemia [114]. The algorithmic approach is illustrated in figure 3.3.

Pulse oximetry analysis for screening did well to detect cyanotic mixing lesions using only numeric oxygen saturation values. Of the 12 CCHDs, COA was the most common yet had the worst false-positive rate and only 46% sensitivity with current screening methods [115, 116, 117]. Even with prenatal ultrasound and pulse oximetry screening, the majority (53–62%) of COA cases were late diagnoses [116, 117] and many such infants were presented to medical care only once they were in life-threatening extremis.

Current newborn screens were inadequate to detect COA, but repurposing existing tech-

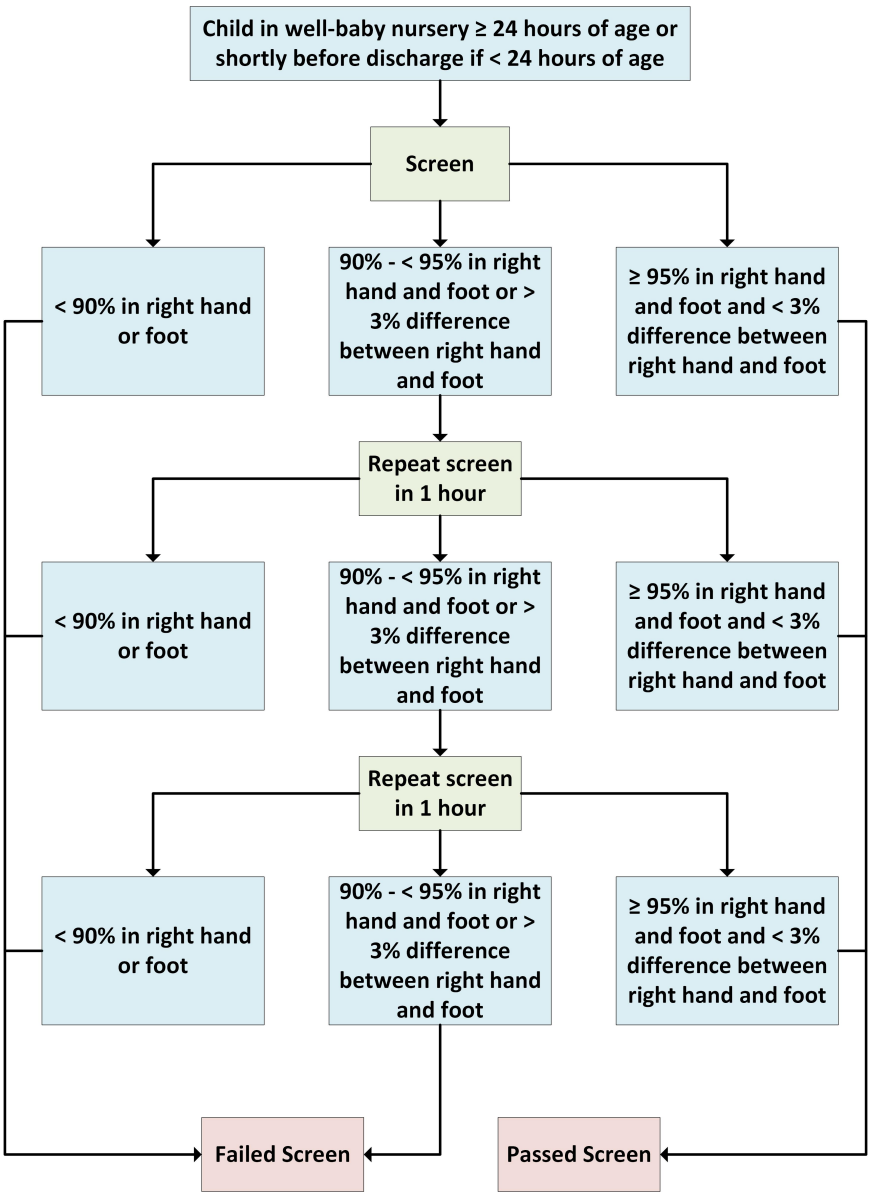

Figure 3.3: Example of neonatal pulse oximetry screening algorithm. Note that an indeterminate zone merited repeated screening in order to attempt to minimize false positives.

nology allowed for more timely diagnosis by analyzing waveform data instead of using integer values of arterial oxygen saturation. PPG was routinely observed as a live waveform on pulse oximetry machines and is a composite of multiple waves. The composite waves have shown promise in detecting changes in peripheral perfusion, blood pressure and local vasomotor tone [47]. Comparing waveform analysis with current non-invasive blood pressure monitoring, pulse oximetry technology may be equal to if not better than current non-invasive techniques [47]. The clinical utility of analyzing PPG waveforms was demonstrated in newborns with COA to quantify physical exam characteristics such as diminished lower extremity pulses and pulse arrival time between extremities [118]. Additional studies had shown promise in PPG signals identifying the presence of significant patent ductus arteriosus in premature infants [119] and using PPG as a useful marker to trend cardiac output and stroke volume [120]. The purpose of the study was to incorporate PPG waveform data to develop an algorithm that increased the sensitivity of detection of COA compared to existing methods.

Similar studies which detected COA are discussed as follows. Itu *et al.* approximated the pressure gradient between the coarctation using fluid dynamics [121]. The authors approximated the blood flow rate and the diameter of the coarctation using information extracted from PPG signals and computed tomography (CT) scan images. They substituted these approximations into their fluid dynamics model and estimated the pressure gradient. Their test results showed they were able to estimate the pressure gradient more accurately than doppler and cuff pressure measurement at the arm and leg. The findings also suggested that the maximum rate of flow may be higher in the ascending aorta compared to the descending aorta in individuals with COA, figure 3.4.

Nielsen *et al.* used cardiac magnetic resonance imaging to gather information on the morphometry of the aorta and the blood flow rates in the individuals with coarctation and compare them to a control group [122]. They used a logistic regression classifier to build a prediction model using the best features that allowed separability between the coarcta-

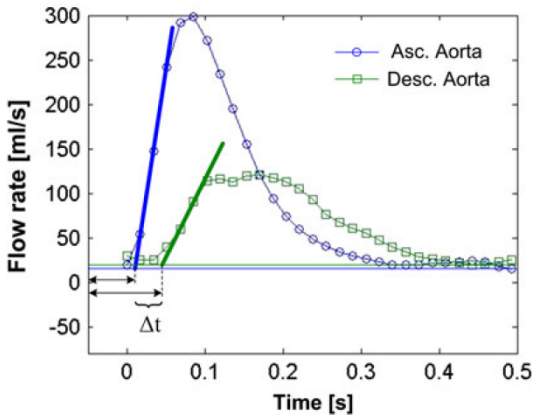

Figure 3.4: The maximum rate of blood flow in the ascending aorta was observed to be higher compared to the descending aorta for subjects with coarctation of the aorta by Itu *et al.* The figure was reprinted by permission from Springer Nature Customer Service Centre GmbH: Springer Nature, Annals of Biomedical Engineering, Itu *et al.* [121], © 2012.

tion and control group. The most discriminative features included the indexed smallest aortic cross-sectional area and rate-corrected descending aorta flow duration. figure 3.5a illustrated the complete list of flow rate features measured. The authors achieved a correct classification rate of 90% on their validation set. This result confirmed that non-invasive modalities like MRI could be used to distinguish between mild and moderate or severe cases of COA as accurately as cardiac catheterization. Cardiac catheterization was considered the gold standard for measuring pressure gradient in arteries.

Other studies conducted on PPG signals were analyzed and possible features extracted from the PPG signal were considered. Sharkey *et al.* estimated the pulse arrival time (PAT) by measuring the delay between the QRS peak in ECG and the associated PPG wave onset at a distal location [124]. Chan *et al.* lowpass filtered a PPG signal with a 0.5 Hz cutoff frequency and showed it effectively had the same spectral properties as a time series extracted from the mean, peaks and troughs [123]. The mean series was evaluated by computing the area under each wave and dividing by the duration of the wave, figure 3.5b. The authors additionally performed principal component analysis (PCA) on the PPG signal. They used the principal components to remove artifacts due to motion from the PPG signal, making feature extraction more robust to noise and artifacts.

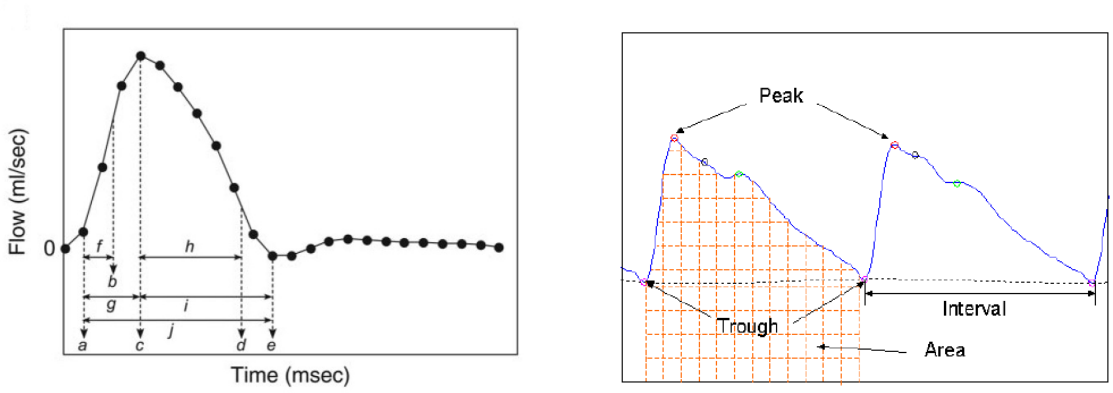

(a) (b)

Figure 3.5: **(a)** The figure was reprinted with permission from [122] (https://doi.org/10.1016/j.accreview.2005.08.092). It illustrates the blood flow parameters measured by the authors. The parameters are, **a.** flow onset, **b.** peak acceleration, **c.** peak flow, **d.** peak deceleration, **e.** cessation of flow, **f.** time to peak acceleration, **g.** rise time, **h.** time from peak flow to peak deceleration, **i.** fall time and **j.** duration of flow. **(b)** The figure illustrates the features, including mean, trough and peak of the PPG wave evaluated by Chan *et al.* The figure was reprinted from [123], © 2006 IEEE.

Sierra-Galan *et al.* showed that athletes treated for coarctation of the aorta as infants may experience effects of the coarctation after periods of stressful physical exercise [125]. They observed diastolic tailing in one such athlete who experienced sporadic headaches after lengthy training sessions [125, Figure 2]. At maximum physical stress, the difference in the maximum rate of flow between the ascending and the descending aorta was larger as compared to rest.

CHAPTER 4
QUANTIFICATION OF MORPHOLOGICAL VARIABILITY IN CARDIOVASCULAR TIME SERIES

The methods used in this research for measuring variability in physiologic waveform signals are described in the following sections. The methods were evaluated on three databases. Each was recorded using a different signal modality, namely ECG, ABP and PPG. The ECG data were obtained from a cohort of war veterans from the Vietnam Era Twins (VET) registry with a history of PTSD and age-matched controls without a history of PTSD. The ABP signals were recorded from individuals admitted to the ICU at Emory University Hospital, Atlanta, GA, that did or did not develop sepsis during their admission. The PPG signals were recorded from neonates less than 30 days of age that were or were not born with a congenital heart defect of COA. Institutional review board (IRB) approval was obtained for performing each study.

The methods described below measured variations within a R peak to R peak (RR) interval time series or physiolgic signal waveform morphology like ECG. The variation in ECG waveform was measured between, successive QRS complexes, T waves and the entire beat on a beat-to-beat basis. In addition to these variables, the MV algorithm was also used to measure beat-to-beat variation in ABP waveforms and also between PPG signals obtained from the body's upper and lower extremities.

4.1 Heart rate variability

HRV measures the variation across time between successive heartbeats and is controlled by the autonomic nervous system (ANS). The ANS is an aspect of the nervous system which regulates involuntary physiological mechanisms such as HR, BP and BR. The ANS can be further classified into the sympathetic, parasympathetic and enteric nervous systems.

HRV features were computed by measuring variation in the RR interval time-series extracted from an ECG recording. The RR interval time-series was computed for each ECG analysis window by performing R peak detection and computing the difference in time between successive beats. Premature and late beats were removed by comparing the pre-RR interval, the RR interval with the previous beat, to the mean of the previous and following five beats. If the pre-RR interval for a beat deviated by more than 20% as compared to the average RR interval, the beat was excluded. The resulting time-series of beat intervals, referred to as the normal beat to normal beat (NN) interval time-series, was free of premature or late beats not representative of the sino-atrial node and was used in further analysis.

ECG data from individuals with a history of PTSD and age-matched controls were used to extract the HRV metrics listed in table 4.1. The HRV metrics were derived using the open-source toolbox developed by Vest *et al.* [3].

The individuals with or without a history of PTSD were classified as active PTSD, recovered from PTSD or controls. MV-based features were extracted and used in addition to HRV features to evaluate classification performance. Details of the analysis were added to chapter 6. HRV features, when evaluated from quiescent windows, were shown to improve the classification of individuals with PTSD [4]. The quiescent windows were defined as the analysis windows with the lowest HR. Each feature was computed for 5, 10-minute long quiescent windows for each individual. The ECG lead with the highest signal quality index (SQI) [126] was used to measure the HRV parameters for each window. A SQI closer to one indicated the ECG window was less affected by external noise. Details of the SQI algorithm were provided in section 4.3.1. The mean was computed across the windows to obtain a feature value for each individual.

4.2 T-wave alternans

The TWA detection algorithm developed by Nemati *et al.* [52] and a modified version explained in section 4.2.1, were applied for ECG data analysis. The algorithm by Nemati *et*

Table 4.1: The HRV features evaluated on the ECG data acquired from the individuals with and without a history of PTSD are listed.

HRV feature	**Definition**
NN_{mean}	The mean of the NN interval time series.
NN_{mode}	The mode of the NN interval time series.
NN_{median}	The median of the NN interval time series.
$NN_{variance}$	The variance of the NN interval time series.
NN_{skew}	The skew of the NN interval time series.
NN_{kurt}	The kurtosis of the NN interval time series.
RMSSD	Root mean square of the succesive interval differences.
pNN50	Percentage of intervals that differ by more than 50 ms.
NN_{IQR}	The inter-quartile range of the NN interval time series.
SDNN	Standard deviation of the NN interval time series.
ULF	Cumulative energy in the 0.0001 - 0.003 Hz band of the power spectrum derived from the NN interval time series.
VLF	Cumulative energy in the 0.003 - 0.04 Hz band of the power spectrum derived from the NN interval time series.
LF	Cumulative energy in the 0.04 - 0.15 Hz band of the power spectrum derived from the NN interval time series.
HF	Cumulative energy in the 0.15 - 0.40 Hz band of the power spectrum derived from the NN interval time series.
LF/HF	Ratio of LF to HF.
TTLPWR	Total cumulative energy in the 0.0001 - 0.40 Hz band in the spectrum derived from the NN interval time series.
AC	The acceleration capacity of the heart derived from the NN interval time series.
DC	The deceleration capacity of the heart derived from the NN interval time series.

al. applied the MMA method for TWA detection and used a surrogate statistical test based on a reshuffling of the T waves to determine the noise threshold. The noise threshold was used to determine when the TWA detection was not a false-positive detection, explained further in section 5.2.2. The MMA algorithm is an established technique in literature. We determined HR and BR pairs that caused false-positive detection of TWA with varying signal-to-noise ratio (SNR), explained in further detail in section 5.2.

4.2.1 T-wave alternan detection: A modified approach

TWAs [127] were measured using a modified approach when analyzing Holter ECGs from individuals with or with PTSD, described in section 6.2.1. We used a TWA detection scheme that combined two best-in-class published methods by Monasterio *et al.* [58, 128] and Nemati *et al.* [52]. The ECG was analyzed in 64 beat windows with 50% overlap. The SQI, explained in section 4.3.1A, of every lead in each window was measured to determine clean leads used in further analysis. The periodic component analysis (πca) transformation was applied to the clean leads in each window to maximize variability in the ECG with a period of 2 beats. Subsequently, the statistical reshuffling algorithm developed by Nemati *et al.* was applied to each transformed lead to test for significant TWAs [52]. Leads with significant TWAs were kept, those without significant detection were affected by noise and set to 0. The inverse πca transformation was applied to TWA amplitude values of the leads with significant detection and the TWA amplitude was estimated in μVs. In case of no significant TWA detection, clean leads with a high SQI were assigned a 0 μV amplitude for the current window. This allowed clean windows with no significant detection to be considered when computing the mean TWA amplitude in each lead. The flowchart provided in figure 4.1 outlines this methodology.

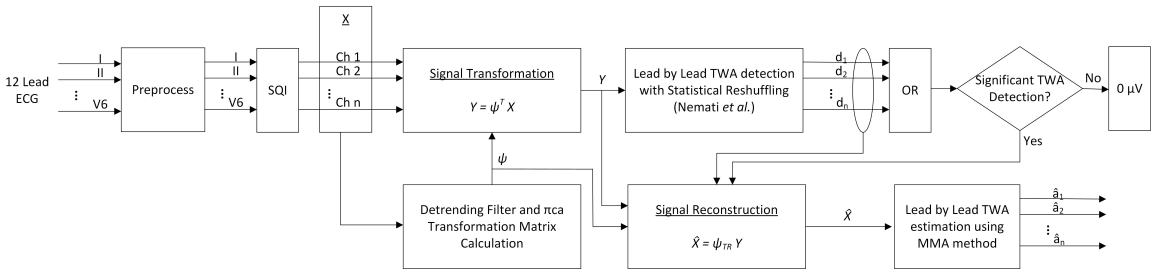

Figure 4.1: Flowchart describing the algorithm used to compute TWAs, using a combination of the methods developed by Nemati *et al.* [52] and Monasterio *et al.* [58]

4.3 Morphological variability magnitude

4.3.1 Morphological variability magnitude in the ECG

A. Preprocessing

The preprocessing of the ECG involved accounting for noisy data windows and detecting fiducial points before performing subsequent analysis. The baseline wander was removed from each signal using the two-step median filters implemented previously by De Chazal *et al.* [129]. These two median digital filters, with orders $f_s/5$ and $3f_s/5$, were applied sequentially to estimate the baseline wander in the signal sampled at f_s Hz. The filter with order $f_s/5$ removed the QRS complexes and P waves. The filter with order $3f_s/5$ removed the T waves. The baseline wander estimate was then subtracted from the original signal. Following baseline wander removal, fiducial points were detected on the ECG signal with the wavelet-based algorithm developed by Martinez *et al.* [130] and used when evaluating MV on the ECG signal.

When evaluating MV over the ECG database of individuals with PTSD, the signal was passed through the SQI algorithm following baseline wander removal to ensure morphological changes measured were minimally affected by noise. The SQI algorithm used two separate fiducial point detection algorithms, one noise sensitive and the other robust to noise. When the detected fiducial points for each agreed, the signal was likely to be clean.

B. Morphological variability magnitude algorithm

The MV of the QRS complex in an ECG was measured using the approach explained below. The first step of the QRS morphology analysis consisted of isolating the QRS complexes in the signal by detecting the onset and offset times of each complex. Then, for each pair of adjacent beats, the QRS complexes were dynamically time-warped (DTW) to align the waveform and be the same length. Time warping was performed using the 'DTW' function in Matlab. The function stretched the 2 QRS complexes or T waves onto a common interval such that the sum of Euclidean distances between corresponding points was minimum. To stretch the QRS complexes, DTW repeated each element of either input as many times as necessary to achieve the minimum sum of Euclidean distances between corresponding points [131]. DTW also caused different points in the two complexes to align with respect to the underlying physiological phenomenon, i.e., peak systole aligned to peak systole. The sum of the squared difference was calculated between them, and repeated between successive QRS complexes over the entire five-minute window of data to create a squared difference (SD) series. Finally, the SD series was converted to the beat-quency domain [132]. As reported by Liu *et al.* [30], the morphological variation for cardiovascular patients was found to be highest in every 2-7 beat period of the ECG prior to the onset of acute myocardial infarction. Similar to previous work, we measured the energy in the power spectrum (beat-quency domain) of the SD series in the range of every 2-7 heartbeats and labeled it the MVM. The methodology is summarized in figure 4.2.

When computing MVM for ECG signals acquired from humans, the QRS complexes in each analysis window were aligned by R peaks and isolated over median QRS onset to the J point interval. This was done to prevent noise from affecting annotations, leading to erroneous measurements. The 90^{th} percentile of the MVM measurements, evaluated from each 5-minute window, was computed and abbreviated as MVM_{90}.

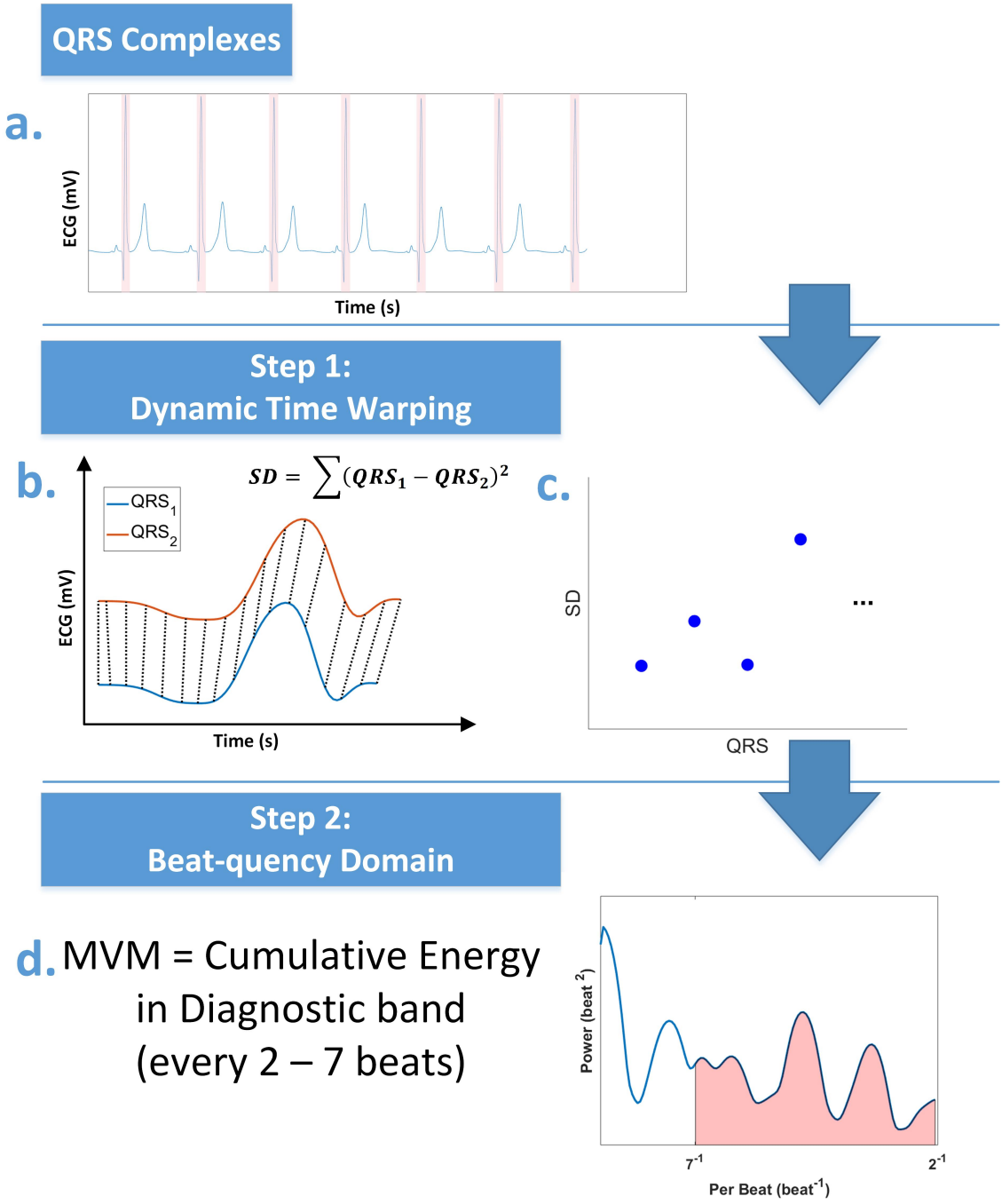

Figure 4.2: Illustration of the process for calculating MVM. a) The QRS complexes in each five-minute window of ECG were isolated. b) Dynamic time warping was performed between successive complexes and the sum of their squared difference was computed. c) These squared differences, SD series, were computed for the entire five-minute window and transformed to the beat-quency domain, analogous to the frequency domain, by applying the Fourier transform. d) The cumulative energy was measured in the range of every 2-7 heartbeats, as reported by [30]. The figure was reprinted from [21]. DOI:10.1088/1361-6579/abd237. © Institute of Physics and Engineering in Medicine. Reproduced by permission of IOP Publishing. All rights reserved.

4.3.2 Morphological variability magnitude in arterial blood pressure

A. Morphological variability magnitude algorithm for ABP

MV of the ABP was computed in a cohort of individuals that did or did not develop sepsis during their stay in the ICU in order to determine if MV of ABP could be used as a predictor of sepsis onset. MV was computed using a variation of the algorithm, described in section 4.3.1B, on 5 minute non-overlapping windows over the 10 hours of available data for each individual in the analysis cohort. To ensure the data used in our computations was optimal/not affected by noise, we used 5-minute windows with a high signal quality index for ABP [133]. Bad quality beats were removed from the sequence before computing the MV of the blood pressure waves.

Blood pressure waves were isolated using automatically computed onset and offset points [134]. The median wave for each 5-minute window was calculated and served as a reference for measuring each wave's variability. For each window, the waves were normalized by the median difference between onset of the blood pressure wave and its peak. Each wave was DTW with the median reference wave, and the sum of SD was computed between the two waves. Subsequently, taking the Fourier transform of this SD series gave a spectrum in the beat-quency domain [132]. The cumulative energy in the diagnostic band of every 2-7 waves of the spectrum was computed as the MV. Figure 7.1 in chapter 7 summarizes the process.

B. Hypotension Analysis

Hypotension was defined as a drop in MAP below 65 mm Hg [135] causing an individual to feel drowsy. Hypotension was associated with sepsis onset, as can be inferred from the definition of the SOFA score [106]. Hypotensive events were measured to predict sepsis onset and served as a benchmark for predicting sepsis onset with MV of ABP. As demonstrated by Hug *et al.*, automated hypotension detection was underutilized when detecting a

drop in MAP or SBP associated with sepsis onset [112]. Similar to Hug *et al.*, the blood pressure waveform data was processed in 10-second non-overlapping windows with a high SQI value. For each processed 10 second window the median MAP and SBP values were computed and stored. If the window was determined to be noisy based on a low SQI, the previously calculated median value was appended for the current window. 3600 sample long MAP and SBP time series resulted for each patient and were used to discover transient hypotensive events. As characterized by Hug *et al.*, a hypotensive event was observed when a sudden drop in blood pressure of 20 mmHg or more caused the MAP to drop below 70 mmHg or SBP to drop below 90 mmHg within a 1-minute window. The event ended when the MAP and SBP rose above 70 mmHg and 90 mmHg respectively.

The definition of transient hypotension by Hug *et al.* was optimized for our application. The optimal parameter set is illustrated in figure 4.3. The window for computing the median blood pressure serving as the reference for measuring pressure drops, the minimum pressure drop and the thresholds below which the MAP and SBP drop were classified as low blood pressure were varied. The window size varied from 1 minute to 10 minutes in increments of 1 minute. The pressure drop varied from 5 mmHg to 30 mmHg in increments of 2 mmHg. The threshold for the drop in MAP was varied from 50 mmHg to 90 mmHg in increments of 5 mmHg. For SBP, the threshold varied from 70 mmHg to 110 mmHg. For each set of values, the number of hypotensive event onsets per hour was counted and used for classification. A hypotensive event triggered when either the MAP or SBP dropped below the respective threshold. The classification results were presented for parameters that gave the highest 10-fold cross-validation (CV) average AUROC.

4.4 Morphological variability of the photoplethysmogram waveform

We retrospectively identified a cohort of neonates admitted to the cardiac intensive care unit who required surgical repair for COA. For each neonate, features were derived from the PPG waveform acquired from different peripheral sites located on the upper and lower half

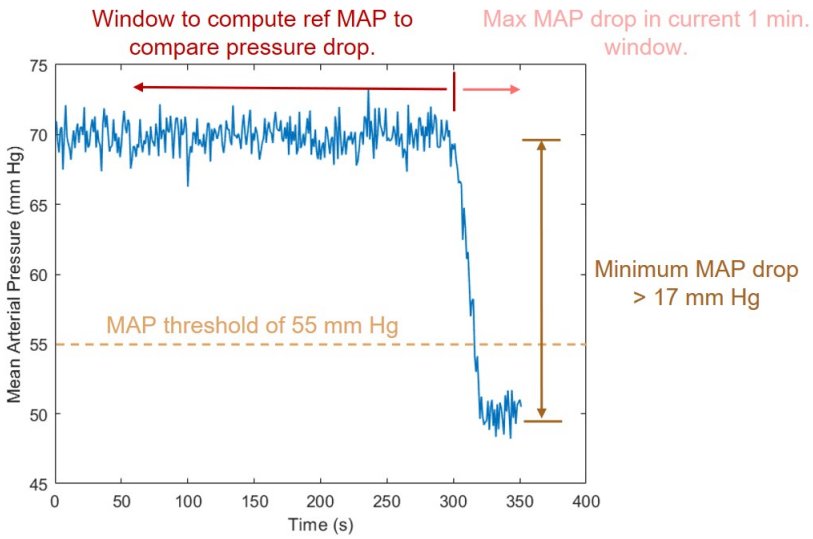

Figure 4.3: A graphical illustration of a drop in MAP corresponding to the optimal hypotensive event for classification discussed in section 7.4.1.

of the body to detect COA. Each of the neonates with COA was started on a prostaglandin infusion to maintain patency of the ductus-arteriosus before surgery. These patients were matched with an equal number of controls who met inclusion and exclusion criteria for admission. Controls with age greater than 30 days at the time of admission, with concurrent left heart obstructive lesions or a patent ductus arteriosus (PDA) were excluded. Single-ventricle patients and those with a significant anatomic abnormality of the great vessels were also excluded.

PPG waveforms were digitally recorded from upper and lower extremities of neonates at different times for the duration of their intensive care stay. Patients with inadequate recordings due to poor signal quality or lack of recording were omitted from the analysis. The PPG waveform was recorded at least at 125 Hz to maintain waveform fidelity. Waveforms that were recorded at 250 Hz were resampled at 125 Hz to maintain consistency and for ease of use due to file size. Nursing notes documented the pulse oximetry probe acquisition site. We allowed a 30-minute grace period to minimize risk of any imprecise documentation of the timing of the site change. If at least 1 hour of data from a single acquisition site was recorded, that continuous waveform was saved for further analysis.

These signals were then bandpass filtered with a 0.5–8 Hz passband to remove baseline drift and high-frequency noise [136]. The continuous waveform for each site was analyzed incrementally in 1-minute windows that met the criteria for a clean waveform defined as having a high signal quality index, as described in previously published work [137]. Clean windows were normalized by amplitude to eliminate confounding effects of acquiring pulse oximetry with different devices. Each waveform characteristic was corrected for heart rate to reduce physiologic differences in the patient's condition from moment to moment.

The four main waveform features evaluated are illustrated in figure 4.4. The slope of a line connecting points at 20% and at 80% of the maximum PPG wave amplitude on the up-slope produced the average rate of of rise (AR) and on the down-slope produced the average rate of fall (AF). This slope represented the average rate of rise and fall of the blood flow rate based on the method by Itu *et al.* to estimate the blood flow rate in the descending aorta [17]. The maximum rate of rise (MR) and maximum rate of fall (MF) were calculated incrementally over short 40-ms windows along the waveform and the greatest value was reported. This method allowed estimation of the maximum rate of rise/fall while filtering against noise, compared to the evaluation of the maximum rate from the first derivative of the PPG wave [18]. Waveform features for each site were computed by taking the median of all the indexed median values for that feature for each 1-min segment. The process of feature evaluation was repeated for each PPG site change of sufficient duration and signal quality, as defined above.

The differences between the upper and lower extremities was calculated to express the difference between those two site locations for each patient, see figure 4.5. Each of these waveform features was evaluated for each patient's PPG signal. The resultant median wave features were analyzed in two main group analyses. First, we compared patients with pre-surgical COA to the unaffected controls, and second, we compared pre-surgical COA to themselves as post-surgical COA following surgical repair.

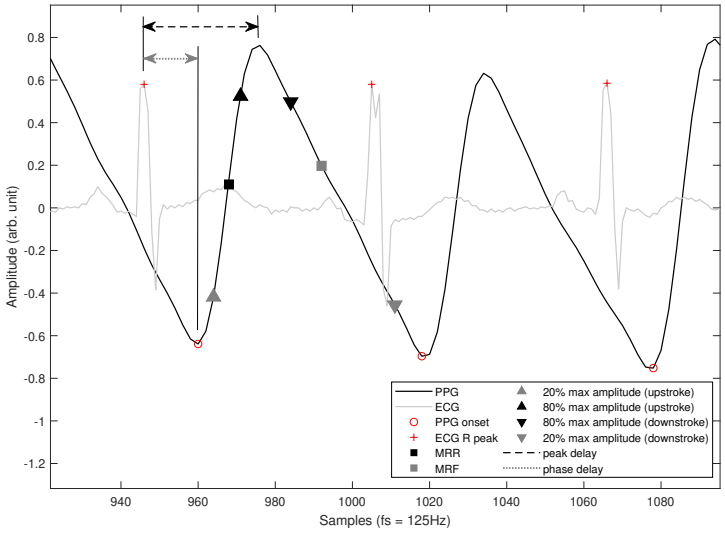

Figure 4.4: Schematic of waveform analysis. A pulse oximetry waveform with a superimposed ECG is demonstrated. The rate of rise and fall were determined by specific points for each waveform cycle. The maximum (rate of rise or fall) was calculated over a rolling 40-ms window between the points at the trough and peak. The average (rate of rise or fall) was calculated between points located at the 20^{th} and 80^{th} percent locations of the waveform amplitude. Phase delay and peak delay were the time intervals between the peak R wave of the ECG to the trough or peak of the pulse oximetry waveform as indicated. The figure was reprinted from [22]. Creative commons license: http://creativecommons.org/licenses/by/4.0/

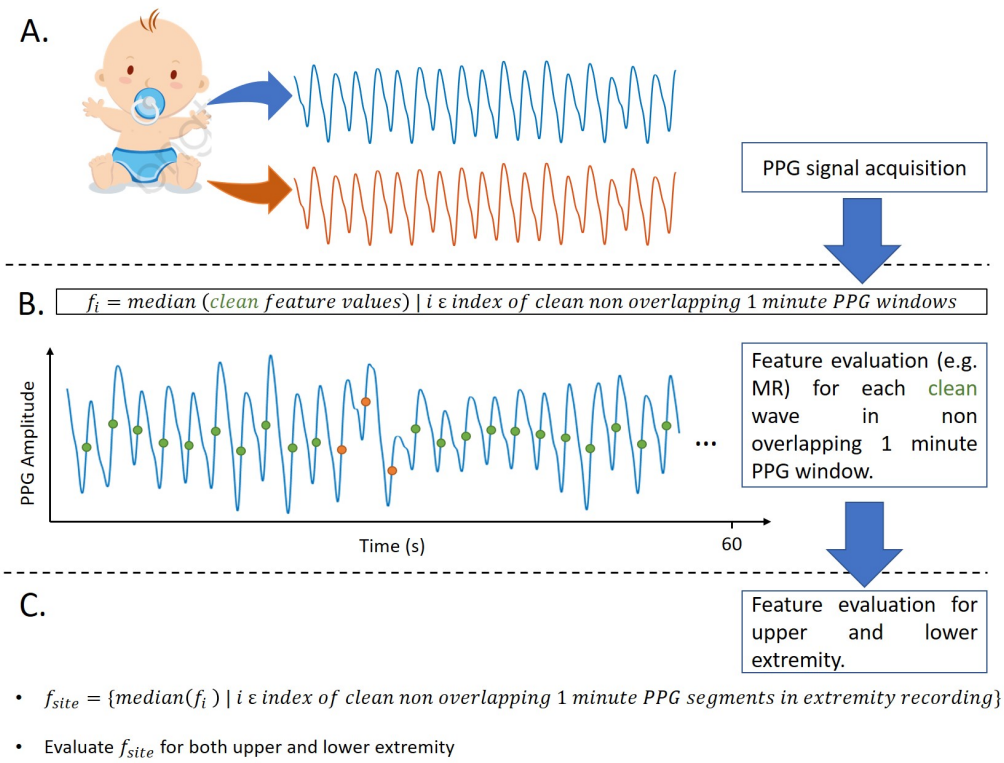

Figure 4.5: Schematic of how PPG waveforms were analyzed from the upper and lower extremities of each patient to evaluate features. The image of cartoon infant reprinted with permission from pngtree.com.

CHAPTER 5
CONFOUNDING FACTORS WHEN MEASURING MORPHOLOGICAL VARIABILITY IN PHYSIOLOGICAL WAVEFORMS

The sources of noise affecting a physiological signal were divided into 2 categories, first due to the motion of the recorded individual and second due to physiological changes within the individual. Additive noise caused by external factors was elaborated further in section 5.1 and due to physiologic sources in section 5.2.

5.1 Movement

The sources of external additive noise included baseline wander (BW), electrode movement (EM) and muscle artifact (MA). Removal of each of these noise types was important for an accurate interpretation of the ECG. An explanation for each origin is detailed as follows.

BW is a low-frequency artifact in ECG signal recordings due to movement of the individual or the electrodes and respiration [138] usually having a frequency of less than 1 Hz [139], figure 5.1a. EM artifacts are mainly caused by intermittent forces applied to the electrodes. EM artifacts shared the signal characteristics of BW but are more troublesome to handle as they resemble features of the ECG waveform, figure 5.1b. MA noise is more prevalent in ECG recordings acquired during exercise and low amplitude waveforms may become difficult to detect, figure 5.1c. In contrast to BW and narrowband interference (50/60 Hz), the spectral content of EM and MA noise overlapped with an ECG and extends to higher frequencies [140]. Therefore removing EM and MA noise is a more involved task. The ECG is a repetitive signal and signal averaging can be used to reduce MA. However, this approach is limited to one particular beat morphology and requires many ECG beats. There is still a need to develop more effective algorithms for MA removal [141, 142].

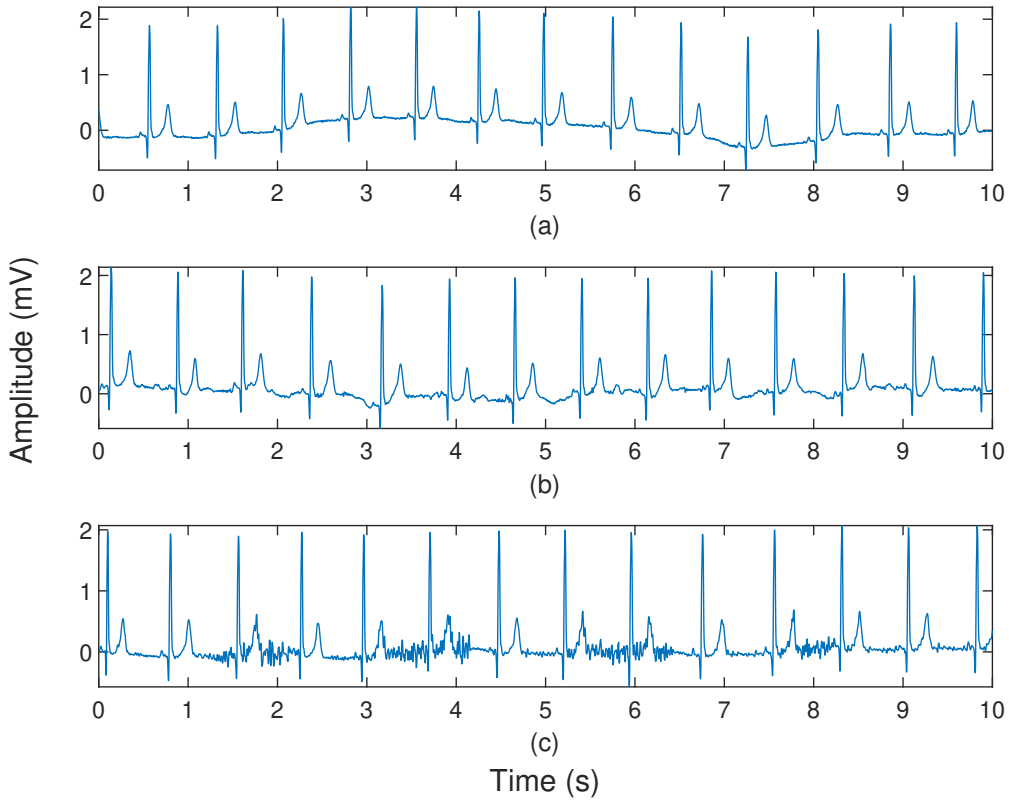

Figure 5.1: **(a)** Baseline wander, **(b)** electrode movement and **(c)** muscle artifact noise in an ECG signal.

5.2 Physiological sources

The confounding effects of HR and BR on morphological variability measured in an ECG were determined on an ECG data set which comprised ten artificial 'subjects' described below.

5.2.1 Artificial ECG database

The methods for measuring MV were tested on artificial ECG signals generated using the simulator developed by Clifford *et al.* [77]. The artificial ECGs were generated for a specified HR, BR and morphology determined by a set of Gaussian coefficients. Twelve lead ECG data, five minutes in duration, was generated with the lead I being used in the

analysis. The ECG data generated had a sampling frequency (f_s) of 1 kHz and an amplitude resolution of 16-bits per sample, sufficiently high to limit quantization noise [143]. The generation of high-resolution ECG enabled evaluating morphological variability on a finer scale.

A description of how the artificial ECG was generated is given as follows. A cardiac dipole vector in 3 dimensions was generated, $d(t) = x(t).\hat{a}_x + y(t).\hat{a}_y + z(t).\hat{a}_z$. The x, y and z were time-varying components in the 3 orthogonal directions. The orthogonal directions were aligned with the axes of the torso and the electrical activity was considered to be a VCG. The dynamics of the model were given in equation array 5.1,

$$\begin{aligned}
\dot{\theta} &= \omega, \\
\dot{x} &= -\sum_i \frac{\alpha_i^x \omega}{(b_i^x)^2} \Delta\theta_i^x \exp[-\frac{(\Delta\theta_i^x)^2}{2(b_i^x)^2}], \\
\dot{y} &= -\sum_i \frac{\alpha_i^y \omega}{(b_i^y)^2} \Delta\theta_i^y \exp[-\frac{(\Delta\theta_i^y)^2}{2(b_i^y)^2}], \\
\dot{z} &= -\sum_i \frac{\alpha_i^z \omega}{(b_i^z)^2} \Delta\theta_i^z \exp[-\frac{(\Delta\theta_i^z)^2}{2(b_i^z)^2}]
\end{aligned} \tag{5.1}$$

θ was the cardiac phase and sweeped between [-π,π] for each beat. ω (the rate of change of θ) depended on the instantaneous HR, measured in beats per minute (bpm), for the current beat (*h*) and was computed as $\omega = 2\pi h/60$. The instantaneous HR was derived from the RR interval tachogram. The changes in the $\hat{a}_x$ direction could be written as a sum of Gaussian functions indexed with i and amplitude $\alpha_{\mathrm{i}}^{\mathrm{x}}$, width $b_{\mathrm{i}}^{\mathrm{x}}$, located at rotational angle $\theta_{\mathrm{i}}^{\mathrm{x}}$ and $\Delta\theta_{\mathrm{i}}^{\mathrm{x}} = (\theta - \theta_{\mathrm{i}}^{\mathrm{x}} + \pi)\mathrm{mod}(2\pi) - \pi$. The rotational angle corresponded to when the Gaussian function peaked during the cardiac cycle. The intuition behind these equations was the variation along each orthogonal direction, assumed to be continuous functions, could be approximated arbitrarily well with a finite number of Gaussian functions [144]. The dipole vector coordinates, originally at a baseline or zero mV, were driven above or below the baseline as they approached the center of the Gaussian functions. This generated a variable length dipole vector that moved in three-dimensional (3D) space, forming the VCG signal

along each of the orthogonal x, y and z axes. Moreover, small random deviations could be added to Gaussian parameters used for generating these vectors to simulate realistic ECG with inter-beat variability. Two forms of variability affecting the ECG beat were built into the model so it resembled realistic signals. First, dynamic heart rate variability, where the instantaneous HR for a given ECG signal could change bidirectionally with a standard deviation of 5 bpm between consecutive beat intervals. Dynamic HRV resulted in QT interval variability in the simulated ECG [145, Fig. 10], where the QT interval was inversely related to the HR [146, 147].

Second, the breathing effect caused amplitude modulation of the QRS complex and T wave with a period determined by the HR and BR. In order to explain how breathing was added to the 12 lead artificial *ECG*, it could be decomposed as in equation 5.2,

$$ECG(t) = H.R.\Lambda.s(t) + w(t) \tag{5.2}$$

$s(t)$ was the VCG signal obtained from the cardiac dipole in 3D. $w(t)$ was additive noise. H was a $\mathbb{R}^{12\times3}$ matrix corresponding to the Dower transform to create 12 lead ECG from the VCG [148]. Λ was a $\mathbb{R}^{3\times3}$ diagonal matrix used for scaling each VCG lead to the correct amplitude and R was a $\mathbb{R}^{3\times3}$ matrix that captured changes like the rotation of the dipole vector in 3D, similar to the breathing effect. H captured stationary information like body conductance and electrode locations. R and Λ captured short term variation within the ECG and could vary with time. By varying the rotational angle for each lead in matrix R according to Givens rotation [149], corresponding periodic amplitude modulation of the ECG signal was introduced. The amplitude changes due to the breathing effect were added to each lead on a per sample basis.

The rotational angle for lead X, $\Phi_x(n)$ was varied according to equation array 5.3.

$$\Phi_x(n) = \sum_{p=0}^{\inf} \zeta_x \frac{1}{1+\exp^{-\lambda_i(p)(n-\kappa_i(p))}} \frac{1}{1+\exp^{\lambda_e(p)(n-\kappa_e(p))}},$$
$$\lambda_i(p) = 20\frac{f_r(p)}{f_s}, \kappa_i(p) = \kappa_i(p-1) + \frac{f_s}{f_r(p-1)}, \kappa_i(0) = 0.35 f_s, \tag{5.3}$$
$$\lambda_e(p) = 15\frac{f_r(p)}{f_s}, \kappa_e(p) = \kappa_e(p-1) + \frac{f_s}{f_r(p-1)}, \kappa_e(0) = 0.6 f_s,$$

where n denoted the sample index, p the breathing cycle index, $1/\lambda_i(p)$ and $1/\lambda_e(p)$ were the duration for inhalation and exhalation periods respectively, $\kappa_i(p)$ and $\kappa_e(p)$ were the delays for the inhalation and exhalation in the sigmoidal functions for breathing cycle p, f_s was the sampling rate, $f_r(p)$ the breathing frequency in breaths per second and ζ_x the maximum angular variation for lead X, which was set to 9 degrees. Φ_x(n) was ζ_x times the summation over each breathing cycle, a product of 2 sigmoidal functions, one for inhalation and exhalation each. Due to the behaviour of the product of the sigmoidal functions, the angle $\Phi_x(n)$ changed with the sample number. It started from zero, rose to the maximum value at peak inhalation and dropped back towards zero near peak exhalation in each cardiac cycle. The same procedure was applied for the rotation of leads Y and Z, $\zeta_y = \zeta_z = \zeta_x$. Adding the breathing effect in this manner resulted in realistic amplitude variations in each lead, observed as variation in QRS area and RS amplitude [150]. The ECG was generated according to equation 5.2. The methodology for the artificial ECG generation was explained in further detail in the original works by McSharry *et al.* [145], Sameni *et al.* [149] and Clifford *et al.* [77].

The ECG simulator also had been shown to accurately generate abnormalities such as TWAs of varying amplitudes [77]. By slightly increasing the amplitude of the Gaussian functions with index i = 9, 10 and 11 in equation array 5.1 for every other beat, the affected T waves were generated with a slightly larger amplitude and artificial ECG with TWAs could be generated. The code for the ECG simulator was provided as part of the open-source toolbox [3]. Additionally, external recorded noise available in the noise stress test database (NSTDB) [138] on PhysioNet was added to the generated ECG. The NSTDB

comprised three types of noise, i.e. BW, EM and MA. A five-second window of a simulated ECG with a HR of 80 bpm, BR of 10 respirations per minute (rpm) and TWA amplitude of 28 μV is plotted in figure 5.2a. Figure 5.2b and figure 5.2c show an enlarged view of how breathing affected the amplitude of the QRS complex and T wave. The morphological variability analysis algorithms measured variations due to the periodic modulation of the ECG beat amplitude and compared them with changes measured in the absence of breathing affects, at the same heart rate to determine statistically significant differences.

To improve the generalization of our results, 10 ECG signals with different morphologies were generated. The QRS complexes and T waves had different R peak amplitudes, Q point, S point amplitudes, T peak amplitudes and shape / QRS axis. Following Clifford and McSharry [145] and Nemati *et al.* [52], the morphologies were derived from a variety of example beats so that the effects of HR and BR leading to elevated MV estimates were considered over a broad range of potential morphologies. These morphologies were derived using a least-square fit of Gaussian parameters (in the VCG representation) to subjects in the Physikalisch-Technische Bundesanstalt database (PTBDB) [151]. The ECGBeatFitter algorithm, included as part of the Open-Source Electrocardiogram Toolbox (OSET) [78], was used to perform a least square fit of the amplitude and variance of the expert placed Gaussian centers to best approximate the VCG. The Dower transform was then applied to map these beats into the 12-lead representation. Hereafter these 10 ECG morphologies were referred to as the 'artificial ECG database'. Five-second windows for each artificial VCG, figures A.1 - A.10, and the Gaussian parameters used for generating the VCG signals, tables A.1 and A.2, could be found in the appendix. For each of these 10 signals, different HR and BR combinations were analyzed to determine when significant elevations in morphological variability of the QRS complex and T wave were observed. The process was repeated for different SNRs to determine at which noise levels the changes observed remained significantly elevated. Conditions of SNR, HR and BR which led to significantly elevated MV in a large fraction of the artificial ECG database, were expected to lead to

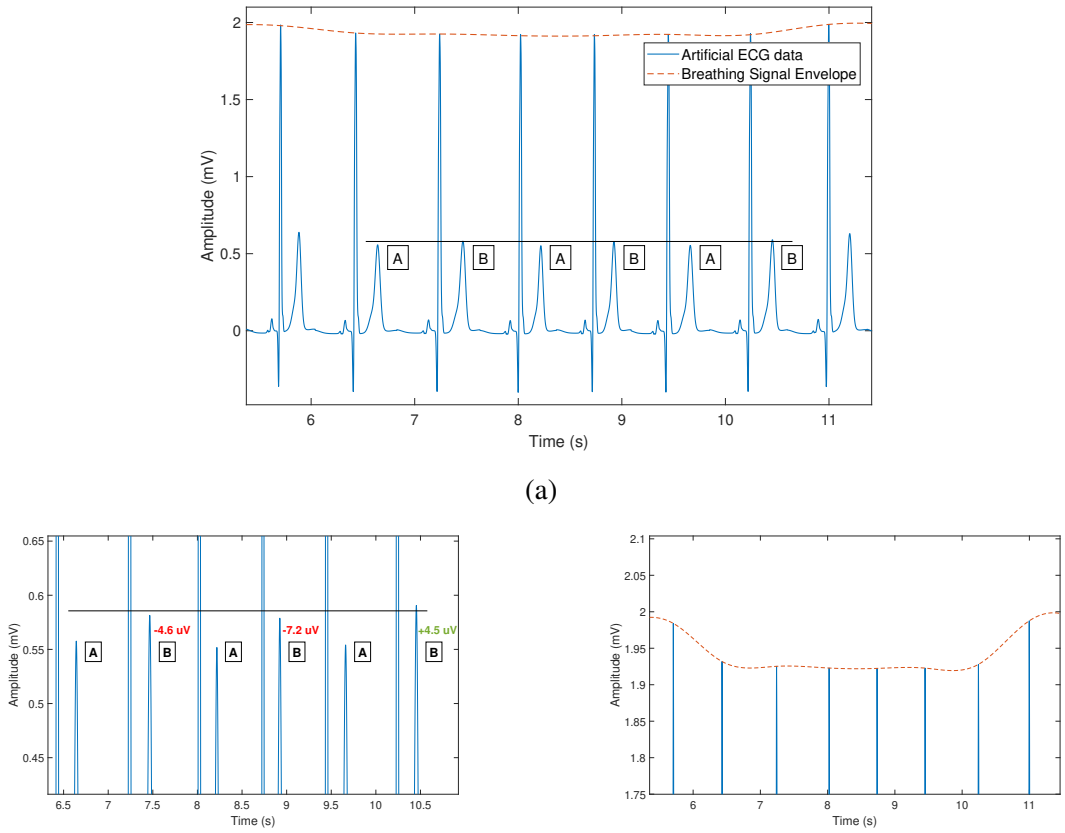

(a)

(b)

(c)

Figure 5.2: **(a)** Plot of a five-second window of artificial ECG at HR 80 bpm, BR of 10 rpm and TWA amplitude of 28 μV. The T waves were assigned to groups A or B, depending on the beat index. A horizontal line corresponding to the higher amplitude of T waves in group B without breathing was drawn to observe the TWAs. The breathing signal corresponding to the envelope of the QRS complex amplitudes was marked with a dashed line. **(b)** An enlarged view of the T wave peaks. Breathing modulated the T wave amplitude causing it to rise above or below the indicated level. The change in amplitude for T waves in group B caused by the breathing effect was marked in red if it dropped below the given level and green if it rose above the level during exhalation. **(c)** An enlarged view of the envelope of the amplitudes of the QRS complexes. Breathing affected the amplitudes of the QRS complexes and T waves. The figure was reprinted from [21] with permission.

falsely elevated MV in a larger sample population.

5.2.2 Statistical test for evaluating significantly elevated morphological variability

HRs and BRs that caused elevated MV were determined using the statistical test described as follows. MV due to the combined effect of HR and BR was computed in the ECG signal with a breathing effect. A significance threshold was computed from a similar ECG signal with no breathing effect, but had other forms of variability like dynamic HRV and additive noise affecting the signal morphology. The significance threshold was used to determine whether the MV measured was significantly elevated than normal in the signal with breathing effect.

We computed a non-parametric statistic described by Nemati *et al.* [52], to determine HR, BR and SNR combinations that caused significantly elevated MV of the QRS complex and T wave when compared to MV measured in an artificial ECG without breathing effect. The QRS complexes in the ECG without breathing effect were randomly reshuffled and the cumulative energy was computed in the band of interest to evaluate the significance threshold for MVM. The order of the QRS complexes was reshuffled 250 times and each time the cumulative energy in the band of interest was computed. The 95^{th} percentile of all 250 energy measurements was the significance threshold. MVM measurements in the signal with breathing above this threshold were statistically significantly elevated with a p-value < 0.05. The process is summarized in figure 5.3a and figure 5.3b. The significance threshold for MVM evaluation was computed for a given heart rate. The signal with the breathing effect was not used for estimating the significance threshold as a random reshuffling of the QRS complexes could cause MV energy due to breathing to spill into the beat-quency band of interest. To compare MV measured due to breathing to a significance threshold measured in the absence of breathing, we determined conditions under which breathing-driven changes would significantly elevate MV compared to MV measured in the absence of breathing effects.

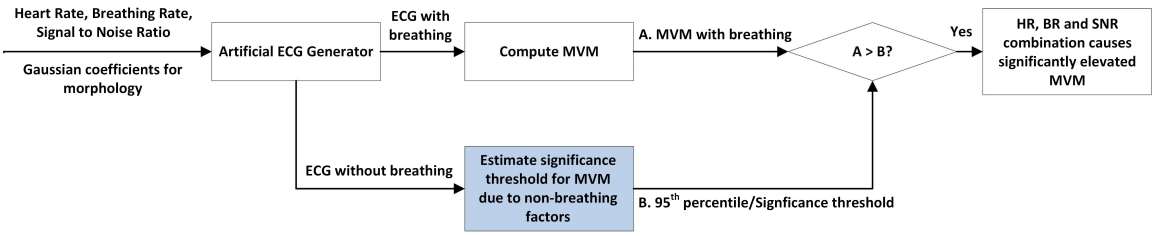

(a)

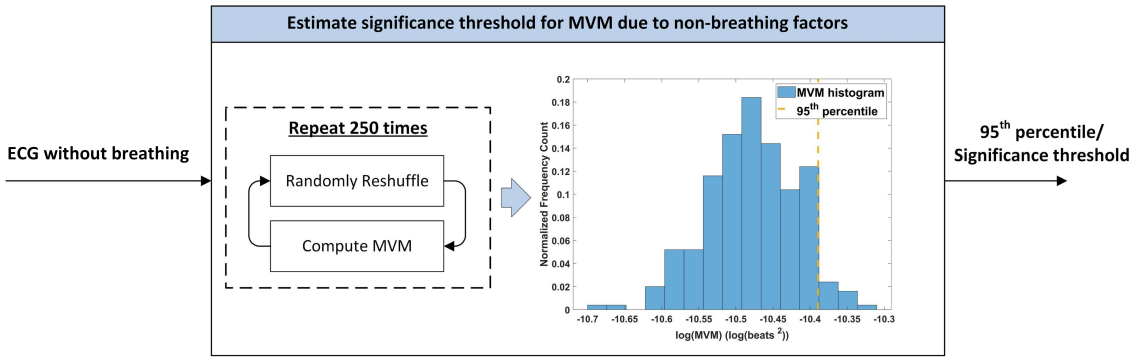

(b)

Figure 5.3: **(a)** A flow diagram of the procedure to determine if MVM measured from a signal with breathing was significantly elevated compared to a significance threshold estimated from a signal without the breathing effect. **(b)** The process in the blue box in (a) of repeatedly reshuffling and estimating MVM to estimate the significance threshold was illustrated. The figure was reprinted from [21] with permission.

TWAs were analyzed using the algorithm developed by Nemati *et al.* [52] with TWAs considered significant at the 5% significance level. The order of the T waves was reshuffled 250 times and the TWA amplitude was estimated after each reshuffle. The 95th percentile of the gamma distribution fitted to the TWA amplitude estimates was considered to be the significance threshold. The significance threshold was estimated from the signal with breathing. When estimating the significance threshold, the TWA significance test reshuffled the T waves in the original sequence to effectively remove any oscillatory behavior, except that likely by pure chance. If we repeated this 100 times and observed less than 5 sequences with higher or equivalent MV as the original sequence, then we could say that the likelihood of observing a true event was 4%, or significant at $p < 0.05$. Since the reshuffled sequence was constructed from the original data, it preserved all statistics except temporal correlations, providing an accurate non-parametric earmarked for the distribution

of the noise at any given moment. Therefore, estimating the significance threshold for TWA from a separate breathing free signal was not needed.

5.2.3 Confounding effect of breathing rate, heart rate and noise on morphological variability in artificial ECG data

ECGs were generated with HRs varying from 40 to 120 bpm in 20 bpm increments and BRs varying as 0, 4 and 6 - 30 rpm in increments of 3 rpm, for each ECG morphology in the artificial ECG database. The BR of 0 referred to the signal without a breathing effect. The QRS complex and T wave MV in the breathing-free signal was due to dynamic HRV and additive noise. The energy in the signal with breathing measured in a narrow band around the dominant beat-quency was referred to as MVM_{nb}, when analyzing HR, BR and SNR combinations for their effects on falsely elevated MVM. The dominant beat-quency was calculated as BR/HR, e.g., for a HR of 80 bpm and a BR of 20 rpm the dominant beat-quency was 0.25 $beats^{-1}$. If the beat-quency aliased, as for the case of HR 40 bpm and BR 30 rpm, the energy was measured in the energy band around the aliased beat-quency, in this case 0.25 $beats^{-1}$. The significance threshold was measured over the narrow band used for evaluating MVM_{nb} and was estimated from the breathing-free signal using the surrogate statistical test, as explained in section 5.2.2.

MVM_{nb} was computed for the set of HR and BR combinations mentioned above and compared with the corresponding significance threshold for each of the 10 morphologies in the artificial ECG database. The fraction of morphologies that had MVM_{nb} above the corresponding significance threshold was computed for the specified HR and BR combinations at 10, 15 and 30 dB SNRs. This fraction of morphologies with significantly elevated MVM_{nb} were presented as contour plots for HR vs BR for a given SNR in section 5.2.3A. The results were used to determine the HR, BR and SNR combinations expected to cause significantly elevated MVM_{nb}, resulting in falsely elevated MVM for a large sample of individuals.

Similar to MVM, the HR, BR and SNR combinations that caused false-positive TWA detection were studied in the artificial ECG database for each ECG morphology. TWAs were analyzed in 60 beat windows with a 50% overlap. The number of overlapping 60 beat windows in a five-minute ECG was dependent on HR. Therefore the number of windows with significant detection was divided by the total number of windows analyzed and called the false detection rate (FDR). The FDR was our detection statistic for falsely elevated TWA at a given HR, BR and SNR. The FDR was averaged for each HR and BR combination across the signals in the artificial ECG database and presented as a filled contour plot for each SNR in section 5.2.3B.

A. Effects of breathing rate, heart rate and noise on morphological variability magnitude

The fraction of signals in the artificial ECG database with MVM_{nb}, explained in section 5.2.3, above the corresponding significance threshold are shown in figures 5.4a-c as filled contour plots. In each plot for a given HR and BR combination, the fraction of artificial ECGs with significantly elevated MVM_{nb} was 1 when all ten artificial ECGs had significantly elevated MVM_{nb} and 0 when none of the signals had significantly elevated MVM_{nb} compared to the corresponding significance threshold. The SNR varied as 30, 15 and 10 dB in figures 5.4 a, b and c. HR and BR combinations for which an abnormally large fraction of at least 8 of the 10 signals had MVM_{nb} above the corresponding significance threshold were enclosed by a white dotted contour. A small fraction of signals had significantly elevated MVM_{nb} energy for high HRs and low BRs at a SNR of 30 dB. At high HRs, the changes in ECG amplitude caused by breathing were small between consecutive beats. The changes caused by breathing were comparable to general morphology changes between QRS complexes and were not significant. For a SNR of 30 dB, HRs between 60-80 bpm and BRs between 15-21 rpm caused significantly elevated MVM_{nb} in at least 8 of the artificial ECGs. These HR and BR combinations were commonly observed in healthy individuals. For a SNR of 15 dB, for HRs between 60-80 bpm, BRs above 17 rpm caused

falsely elevated MVM in at least six artificial ECGs. For a SNR of 10 dB, HR/BR pairs of 40/24 and 100/30 bpm/rpm caused falsely elevated MVM in at least eight artificial ECGs. However, these HR/BR pairs were outside the physiological range of healthy individuals.

B. Effects of breathing rate, heart rate and noise on T-wave alternans

For different SNRs, HR and BR combinations which falsely elevate TWA were determined. The FDR, explained in section 5.2.3, was computed over a range of HR and BR combinations for each signal in the artificial ECG database and averaged for each SNR. The averaged result was presented as a filled contour plot. For a given SNR, HR, and BR, the average FDR was 1 when all of the analyzed windows in each artificial ECG had a significant TWA detection and 0 when none of the signals had significant TWA detection in any analysis window. For a SNR of 30 dB, figure 5.5a, the false elevation of TWAs was observed at HR/BR pairs of 60/30 bpm/rpm, 60/15 bpm/rpm and 120/30 bpm/rpm. The HR/BR of 60/30 bpm/rpm was obvious as the breathing rate was exactly half the HR, which would induce T wave amplitude modulation with period 2. The HR/BR pair of 60/15 bpm/rpm was not as obvious. When the BR was $1/4^{th}$ the HR, the breathing cycle caused a difference in amplitude between the average even and average odd indexed T wave. This difference was detected by the MMA method used for TWA evaluation. This observation was confirmed by the significant number of false elevations at a HR/BR pair of 120/30 bpm/rpm. For a SNR of 15 dB, figure 5.5b, there was false elevation of TWA observed at a HR/BR pair of 60/30 bpm/rpm. At a SNR of 10 dB, figure 5.5c, the signal was too noisy for reliable TWA detection. For each SNR, HR and BR combinations, which caused significant false TWA detection in at least 40% of all analyzed windows, were enclosed by the dotted white contour in the respective plot.

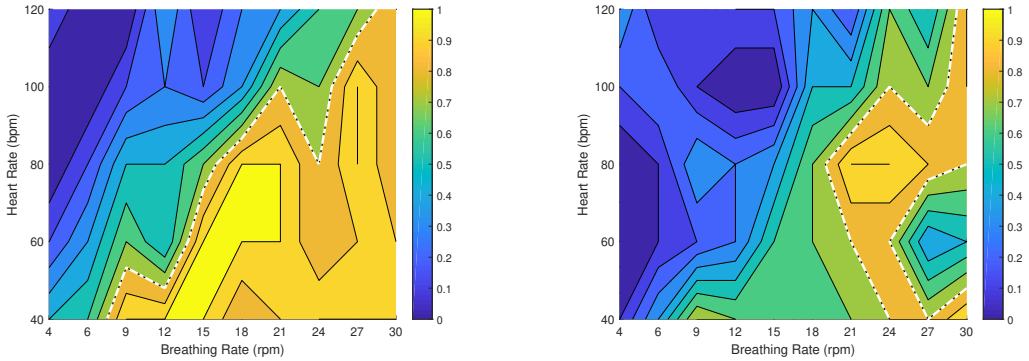

(a)

(b)

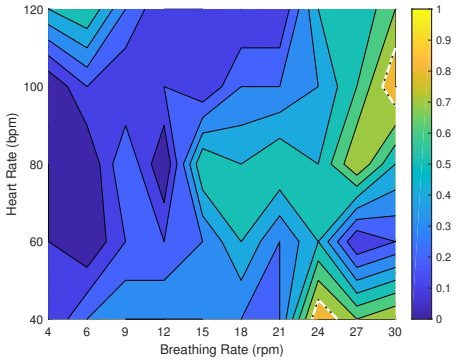

(c)

Figure 5.4: For different HR, BR and SNR combinations, MVM_{nb}, section 5.2.3, was measured in each signal in the artificial ECG database. For each SNR, the fraction of 10 signals with significantly elevated MVM_{nb} compared to the corresponding significance threshold were plotted for HR versus BR. The white dotted contour encloses HR and BR combinations which caused significantly elevated MVM_{nb} in at least 8 of the 10 signals in the artificial ECG database. **(a)** For a SNR of 30 dB, low HRs and high BRs resulted in significantly elevated MVM_{nb} for a large fraction of signals. **(b)** For a SNR of 15 dB, HR/BR pairs in a healthy individual's physiological range, i.e. 60/15, 60/18, 80/18 and 80/20 bpm/rpm caused significantly elevated MVM_{nb} in at least 6 artificial ECGs. **(c)** For a SNR of 10 dB, HR/BR pairs outside the physiological range of healthy individuals, i.e. 40/24 and 100/30 bpm/rpm, caused significantly elevated MVM_{nb} in a large fraction of signals.

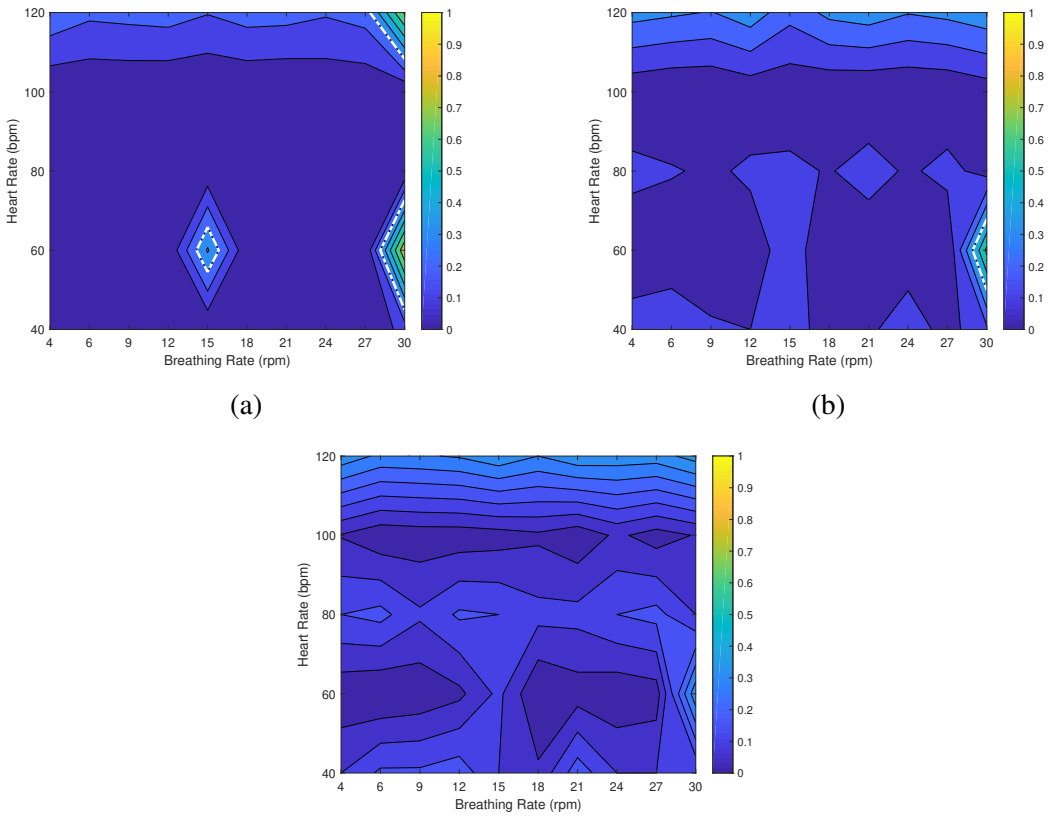

(a) (b)

(c)

Figure 5.5: The FDR for TWA, explained in section 5.2.3, was computed for each signal in the artificial ECG database over a range of HR and BR combinations for a given SNR. The FDRs were averaged across the 10 signals for each SNR and presented as a filled contour plot for HR versus BR. **(a)** The average FDR was measured at a SNR of 30 dB. Falsely elevated TWAs were observed for HR and BR pairs of 60/30 bpm/rpm, 120/30 bpm/rpm and 60/15 bpm/rpm. **(b)** The average FDR was measured at a SNR of 15 dB. Falsely elevated TWAs were observed at the HR and BR pair of 60/30 bpm/rpm. **(c)** The average FDR was measured at a SNR of 10 dB. Falsely elevated TWAs were not observed for any HR and BR pair suggesting the signal was too noisy for reliable TWA detection. In each figure, a white dotted contour enclosed HR and BR combinations which falsely elevated TWA detection.

5.2.4 Confounding effects of BR when measuring morphological variability in arterial blood pressure

A drop in systolic blood pressure during inspiration is observed in normal individuals [152]. During the inspiration the decrease in pressure in the chest cavity results in an increase in venous return causing an increase in pressure in the right ventricle. Since more blood remains within the lungs during inspiration their is a resultant drop in the systolic blood pressure. In diseases like 'tamponade', their is external pressure built on the right ventricular wall which results in an increase in pressure on the ventricular septum instead of the right ventricular wall. This causes a decrease in the left ventricle filling and stroke volume, which results in a much lower systolic blood pressure. A drop in systolic blood pressure of greater than 10 mm Hg is associated with 'pulsus paradoxus'. In pulsus paradoxus, a greater confounding effect of respiration can be expected when measuring MV of ABP [153, 154].

5.2.5 Confounding effects of HR when measuring morphological variability in photoplethysmogram

The heart rate confounds slope based features measured from the PPG waveform. The AR and MR were determined to be positively correlated with the HR. The AF and the MF were observed to be negatively correlated with the HR. Scatter plots of the MF and MR against HR for a control individual are given in figure 5.6a and figure 5.6b respectively.

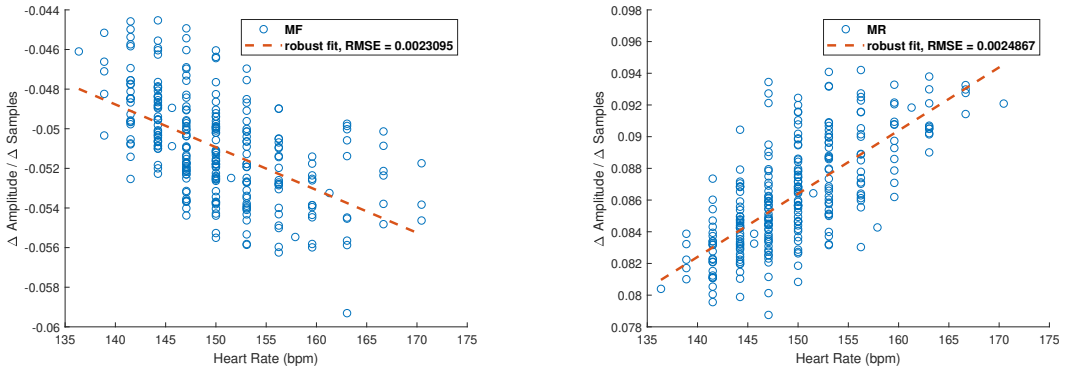

(a) (b)

Figure 5.6: The dependance of slope based features derived from photoplethysmogram waveforms on heart rate is illustrated. **(a)** The maximum rate of fall during the PPG wave downstroke is negatively correlated with the heart rate. **(b)** The maximum rate of rise during the PPG wave upstroke is positively correlated with the heart rate. The figure was reproduced from [21] with permission.

5.3 Framework for mitigating noise and confounding factors

The additive noise from external sources was handled as follows. For each ECG signal the baseline wander was removed using the median filter implemented by De Chazal *et al.* [129]. When evaluating MV over the human ECG data, after baseline wander removal the signal was passed through a SQI package [126] to ensure morphological changes measured were minimally affected by noise. Figure 5.7 illustrates how the SQI of the ECG signal dropped as it became noisier. For the clean signals, fiducial points were detected by the automatic fiducial point detection algorithm developed by Martinez *et al.*. Details on the preprocessing of the ECG signal to account for noise were added to section 4.3.1.

Possible mitigation strategies of accounting for confounding from physiological sources included discarding ECG windows determined to be significantly affected by the effects of HR and BR. Section 5.4.1 explained the analysis performed on individuals from the NSR database on PhysioNet, to determine the fraction ECG windows in channel 1 of the entire database significantly affected by the effects of HR and BR. A simple approach could be to correct MV measurements for BR and HR, similar to QT interval correction for heart rate

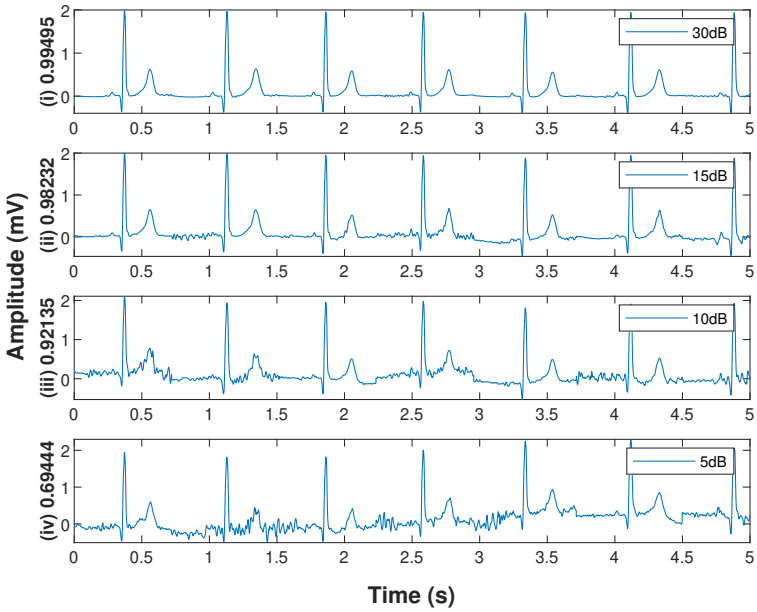

Figure 5.7: A five-second window of simulated ECG with SNRs of 30,15,10 and 5 dB is plotted in subplots (i), (ii), (iii) and (iv) respectively. The signal quality index for each signal is also given as the y-axis label for each plot. For each subplot, the y-axis is plotted as amplitude in mV. The x-axis is plotted as time in seconds.

[155]. Simulations can be used to determine the relationship between BR, HR, breathing signal amplitude and the MV measurements. The MV measurements expected due to BR and HR effects can be subtracted from the MV measurements made from the actual ECG signal being analyzed. This approach is somewhat ad hoc, though. A more principled, but data-intensive approach could be to measure the breathing rate and heart rate in ECG windows and present them to the prediction model (with the MVM and TWA measurements) as independent parameters at the time of training. In this way, the model will learn to adjust the decision boundary for the effect of BR and HR on non-pathologically elevated TWA and MVM, for a given population. Section 5.4.2 explained the analysis where a previously published metric MVB_{90} [30] was evaluated on ECGs from individuals with and without PTSD. Adding HR and BR as independent predictors to the model resulted in an increase in classification AUROC. HR and BR can also affect the MV measured in ABP waveform. Strategies similar to those used when evaluating MV in ECG can also account for HR and BR effects when computing MV in ABP.

When evaluating changes in slope based features from the PPG waveform, the confounding effects of HR can be negated by resampling each wave to a fixed length. The PPG waveform can be normalized to unit amplitude before feature computation, to account for variability in signal amplitude between different PPG acquisition devices.

5.4 Evaluating the effects of heart rate and breathing rate on morphological variability of ECG

Section 5.2.3 explains how the morphological variability measurement algorithms were applied to the artificial ECG database to determine HR and BR combinations, at a given SNR, that led to elevated MV of the QRS complex and T wave.

Once HR, BR and SNR combinations that led to artificially inflated MV had been determined, MV was evaluated in the NSR ECG database on PhysioNet [20], section 5.4.1. The fraction of analyzed windows with elevated MVM and TWA due to the combined effects of HR and BR was computed. The fraction of windows with TWAs above a critical threshold of 47 μV was computed, before and after accounting for analysis windows expected to have elevated MV due to HR and BR. The procedure was explained in section 5.4.1. The methods used to evaluate the classification between individuals with and without PTSD using MVB_{90}, HR and BR were described in detail in section 5.4.2.

5.4.1 Normal sinus rhythm ECG database

We tested our algorithm on data acquired from the NSR database on PhysioNet [20, 156]. The database contained two-channel ECG for each of 18 subjects sampled at 128 Hz. Each recording was approximately 24 hours in duration from healthy individuals, including 13 women, between the age of 20 and 50, and 5 men, between the age of 26 and 45.

A. Analysis

We used channel 1 of ECG for each subject in our analysis. ECG data for each subject was upsampled to 1 kHz before analysis. For MVM analysis, non-overlapping five-minute windows in the ECG with a high SQI value were analyzed. Analyzing windows with a high SQI avoided measuring any erroneously elevated MVM due to noise and allowed accurate measurement of HR and BR for each window. TWA detection was considered significant after computing the non-parametric statistic, described in section 5.2.2. The significance threshold estimated by the non-parametric statistic was adaptive with respect to the level of noise in the ECG. A noisy ECG led to estimating a higher significance threshold, reducing the chance for a significant TWA detection. As mentioned in section 5.2.2, TWAs evaluated on the NSR ECG database were considered to be significant at a 5% significance level. To accurately estimate the distribution of noise at any instant for MVM using the non-parametric statistic, the QRS complexes' sequence needed to be reshuffled to remove any oscillatory behavior and temporal correlations except those likely due to random chance. The sequence of QRS complexes needed to be reshuffled to prevent oscillatory behavior in the original sequence in every 2-7 beat band from reappearing in the every 2-7 beat band after reshuffling. The application of the non-parametric statistic for MVM was more involved than for TWAs, which measured variability in the T wave strictly over a period of two beats. The SQI was considered a standard for rejecting noisy ECG analysis windows. Previous works that used SQI to reject noisy ECG windows in their MV analysis included Liu *et al.* [30]. For TWAs, the analysis was conducted on windows with HRs below 120 bpm since TWAs measured at high heart rates could also be falsely detected due to the effects of breathing. For MVM and TWA analysis, the fraction of analyzed windows with MV significantly affected by HR and BR was computed. Since windows with a high SQI were analyzed, the HR and BR could be reliably measured. The HR and BR combinations causing elevated MV at a SNR of 30 dB, enclosed by the white dotted contour in figures 5.4a and 5.5a, were used for determining the affected windows. The BR in each analysis

window was estimated using open-source software by Charlton *et al.* [76]. The following method, which was reported as measuring breathing rate most accurately from the ECG was used. Specifically, the breathing signal was estimated in each analysis window from the variation in baseline, amplitude, and frequency of the ECG (mean amplitude of Q point and proceeding R-peak, R-peak amplitude and RR interval time series) [76]. For each of these three estimated breathing activity sources, the breathing rate was determined using the 'Count-Orig' method described by Schafer *et al.* [157], explained as follows. Each breathing signal estimate was bandpass filtered with a 10th order Butterworth filter, with a passband of 0.1 - 0.5 Hz. The local maxima and minima were then determined in this filtered signal. A threshold level was defined as 0.2 x 75th percentile of all maxima ordinate values. Each breathing cycle was considered to have begun and ended at consecutive local maxima above this threshold level. A breathing cycle was considered valid if there was only one minimum below zero and no other extrema between the maxima initiating and terminating the breathing cycle. The breathing frequency was estimated from the reciprocal of the average length (in seconds) of all valid breathing cycles. Each breathing rate estimate from each of the three sources (baseline, R-peak amplitude and RR interval time series) was fused using an averaging approach per Karlen *et al.* [158] to obtain a breathing rate estimate for the analysis windows. The HR was computed as the reciprocal of the median R peak to R peak interval in seconds in each analysis window divided by 60. For TWA analysis, the fraction of analyzed windows above a 'critical' threshold was reported, before and after correcting the effects of HR and BR. The corrected fraction of analyzed windows was computed by discarding data windows with TWA significantly affected due to HR and BR - see figure 5.5a. Following Verrier *et al.* [96], we chose a critical threshold of 47 μV. This allowed us to demonstrate how TWA measurements may be falsely detected at elevated levels associated with poor health outcomes when impacted by these factors.

B. Results

The fraction of MVM and TWA windows significantly affected by HR and BR were 66.76% and 8.33% respectively. The results suggested a significant part of the data had MV confounded by the effects of HR and BR. As noted in section 5.4.1, TWA presence and magnitude was estimated in analysis windows with HRs less than 120 bpm. The fraction of significant TWA amplitudes above 47 μV before and after adjusting for HR and BR were 1.75% and 1.34% respectively. The fraction dropped after adjustment indicating HR and BR effects could falsely inflate TWA amplitudes to elevated levels associated with poor health outcomes. TWAs above a threshold of 47 μV were predictive of SCD [96].

5.4.2 Post-traumatic stress disorder ECG database

The PTSD database consisted of 32 individuals with PTSD and 179 controls with no history of PTSD. Each individual had a 12 lead Holter ECG recording approximately 24 hours in duration. Increased levels of stress were reported to be correlated with increased MV of the ECG [11, 12], therefore PTSD individuals were expected to have elevated MVB of the ECG compared to controls. MVB was evaluated for each individual in the PTSD database for each analyzable non-overlapping 5-minute window in each lead. For each individual, the 90$^{\text{th}}$ percentile computed for the MVB measurements (MVB_{90}) in each lead, in addition to the HR and BR estimate for the corresponding window, was used as a feature to perform classification between the individuals with and without PTSD. The previously published MVB_{90} metric [30] was evaluated to determine if adding HR and BR as features led to an expected increase in classification performance.

A. Analysis

The MVB was measured for each non-overlapping 5-minute window, determined to be analyzable using the SQI algorithm, in each lead. For each lead, the MVB value closest to MVB_{90} was considered as a feature to classify individuals with and without PTSD. HR

and BR were added as additional features and it was hypothesized adding these features led to an increase in the classification performance. HR was estimated as described in section 5.4.1. BR was estimated using the 'Count-Orig' method applied to the breathing signal estimated from the amplitude changes. The fused estimate was evaluated when the BR estimate from each amplitude, frequency and baseline variation was close. It was therefore missing in a few of the windows for which MVB_{90} was included as a feature. Ten-fold CV with a logistic regression classifier was used to evaluate each feature set's performance. Thirty-two control individuals were randomly sampled from the whole group of controls to create a balanced dataset of PTSD and control individuals for performing classification. The process of sampling controls and performing classification was repeated eight times, and the average AUROC was reported. The average AUROC was reported for classification performed using MVB_{90} separately and MVB_{90}, HR and BR combined. The distribution of AUROCs for classification with MVB_{90}, HR, BR was compared to that with MVB_{90} only. Classification was performed with the average HR and average BR for each individual to determine if the features were independently predictive of PTSD.

B. Results

The highest average AUROC, across leads, evaluated using MVB_{90} in lead II as a feature was 0.54, with PTSD individuals having higher MVB_{90} than controls in lead II. After adding the HR and BR estimated for each corresponding analysis window, the average AUROC increased to 0.62. The results suggested that adding HR and BR as additional parameters improved separation between the PTSD and control individuals, compared to when independently using MVB_{90} for classification. The distribution for eight repeated AUROCs evaluated using MVB_{90}, HR and BR was significantly higher than that evaluated using MVB_{90} only with a p-value < 0.05. The two-sample Kolmogorov-Smirnov test was used to determine a significant difference. Classification using the average HR and average BR yielded eight repeated average AUROCs of 0.53 and 0.48 respectively, suggesting both

features were not independently predictive of PTSD.

5.5 Discussion

Our study shows, for the first time, the need to consider BRs in addition to HRs and SNR when measuring MV. Other studies have used alternative methods to exclude confounding observations, (notably using high heart rate thresholds or statistical rejection techniques) but do not explicitly consider breathing. Nearing *et al.* measure MV in T waves in an alternating pattern and only exclude analyses at high heart rates [71]. Nemati *et al.* add a non-parametric statistical significance test to reduce the false positive detection based on noise, but this method does not consider breathing effects [52]. However, their work does consider the effect of heart rate on TWA and they notice a paradoxical rise in TWA during sleep / at low heart rates, which can be explained by the confounding effect of breathing [159]. Liu *et al.* measure MV of the entire ECG beat including the QRS complex and the T wave in a non-alternating pattern, and use a signal quality index (developed by Li and Clifford and published in [3, 160]) to reduce any false-positive detections of elevated MV due to noise [30]. Similar to other studies, they also ignore breathing effects, or rather, these are implicitly captured in the analysis and may even dominate the metric. Our work demonstrates significant effects on MV of ECG due to breathing (at specific HR's and SNR's) and therefore highlights an important gap in previous work, which may well have included false triggers related to breathing rate, heart rate and noise. Such covariance between HR, BR and condition/outcome often differs between populations and can lead to false conclusions, both positive and negative.

Our findings are consistent with previous literature that demonstrates alterations in QRS complex and T wave morphology with breathing [161] and heart rate variability [162]. These morphological changes in the QRS complex and T wave correlate with those in MVM and TWA, respectively. Breathing causes changes in chest impedance and the position of the heart with respect to the ECG electrodes, both of which lead to amplitude

modulation of the QRS complex and T wave [163]. Moody *et al.* build upon these principles and estimate the breathing signal from QRS complex amplitude modulations due to breathing [161]. For TWA, false positives are observed when the ratio of the heart rate and breathing rate is a factor of 2. For these heart rate and breathing rate pairs, the T wave amplitudes are modulated so that there is a significant difference in amplitude between average even and average odd indexed beats being analyzed. It is important to note these HR and BR combinations will not necessarily cause false positive detection for other TWA detection algorithms. For example, the spectral method [96] will only detect falsely elevated TWAs at HR to BR ratios of 2, since variability with periods 4, 8, ... are measured at the separate frequency intervals 0.25, 0.125, ... Hz respectively. Increased false-positive detection of MVM is detected for low heart rates and high breathing rates. Under these conditions, there is higher beat-to-beat variability measured in the beat-quency domain. Situations in which false-positive elevations occur are plausible. As shown in figures 5.4a and 5.4b, many elevations in MVM occurred at breathing rates and heart rates that are considered physiologically normal, including 12-20 rpm and 60-80 bpm. For TWA, breathing rate and heart rate pairs of 15 rpm and 60 bpm or 20 rpm and 80 bpm are likely a common occurrence. There is a greater confounding effect in MV observed at high values of SNRs for both QRS complexes and T waves, figure 5.4 and figure 5.5 respectively. The confounding effect of heart rate and breathing rate are observable in MV for SNRs above 15 dB. For lower values of SNR, the effects of breathing are less apparent. Nonetheless, these signals are more likely excluded from analysis because of poor quality.

These findings are subject to certain limitations. First, our findings are based on simulated ECG data and normal patients. Although this may be thought of as a limitation, it is a necessary step in defining a ground truth and produces an extensive analysis. Experiments are performed on realistic simulated ECG with dynamic heart rate variability and breathing effect built into the model. Notably, the ECG morphologies are derived from signals in the PTBDB on PhysioNet. These signals are considered to be the gold standard, to determine

conditions of HR and BR expected to cause false-positive detection of MV on a larger sample size. The analysis was performed for different SNRs to determine how noise affects the rate of false-positive detection. Also note that experiments are then performed on real data from the NSR database, and the existence of 'natural' T Wave Alternans is significantly reduced in this normal population, casting doubt on the notion of such non-pathological variability.

Future studies need to consider adjusting for breathing rate and heart rate when measuring MV. Currently, when evaluating TWAs, MV measurements are corrected by removing windows significantly affected by HR and BR, thus resulting in data loss that may cause a bias itself.

To investigate the effect of HR and BR as features in addition to MVB, a cohort of individuals with and without PTSD is analyzed. The addition of HR and BR to MVB_{90} as features for classifying PTSD individuals from controls results in a 8% increase in average classification AUROC. Although the database's size is limited, with only 32 individuals with PTSD, the results encourage and motivate investigation on a larger balanced database with a higher number of patients. Both average HR and BR independently are not predictive of PTSD.

The study aimed to improve methods for calculation of MVM and TWA by closely examining the extent to which BR coupled with HR and noise may artifactually inflate results and falsely indicate increased arrhythmic risk due to cardiovascular disease. By doing so, we may underscore the importance of evaluating breathing separately and recognize its potentially independent effects in classifying arrhythmia risk. This is particularly important when considering interventions focused on the heart versus lungs, for example. To facilitate further examination of this paradigm, we also provided an open-source toolbox that has been stress tested to accurately measure morphological variability in realistic simulated ECG under varying amounts of noise. This toolbox will allow others to repeat the work presented here and examine new data for the confounding factors of HR and BR [3, 160].

CHAPTER 6
APPLICATION OF NOVEL MORPHOLOGICAL VARIABILITY ANALYSIS FRAMEWORK TO ECG IN A PTSD POPULATION

6.1 Benchmarking the MVM algorithm on a public database

Before application to the PTSD data, the MVM algorithm is benchmarked on the NSR, CHF and SCD databases on Physionet [20]. Based on the severity of the heart disease the MVM_{90} metric was expected to be lowest in the individuals with NSR, followed by the CHF database and individuals in the SCD database having the highest MVM_{90}. The distributions of MVM_{90} measured in channels 1 and 2 of each database are plotted in figures 6.1a and 6.1b, respectively. For channel 1, MVM_{90} was significantly elevated in the CHF and SCD groups compared to the NSR groups with a p-value < 0.001. In channel 2, MVM_{90} was significantly elevated in the CHF and SCD groups compared to NSR with p-values of < 0.05 and < 0.001, respectively. The MVM_{90} in channel 2 was significantly elevated in the SCD group compared to the CHF group with a p-value < 0.05. The two-sided Wilcoxon rank-sum test was used to test for significant differences. The parameters for the distributions were consistent with expected results. It is to be noted channel 1 was less affected by external noise. Hence a greater number of individuals were analyzed in channel 1.

6.2 Morphological variability of ECG in a population with or without a history of PTSD

6.2.1 Data

The data was acquired from 233 male individuals with an average age of 67.49 ± 2.54 years. The records were divided into 33 active/current PTSD, 21 recovered from/past PTSD

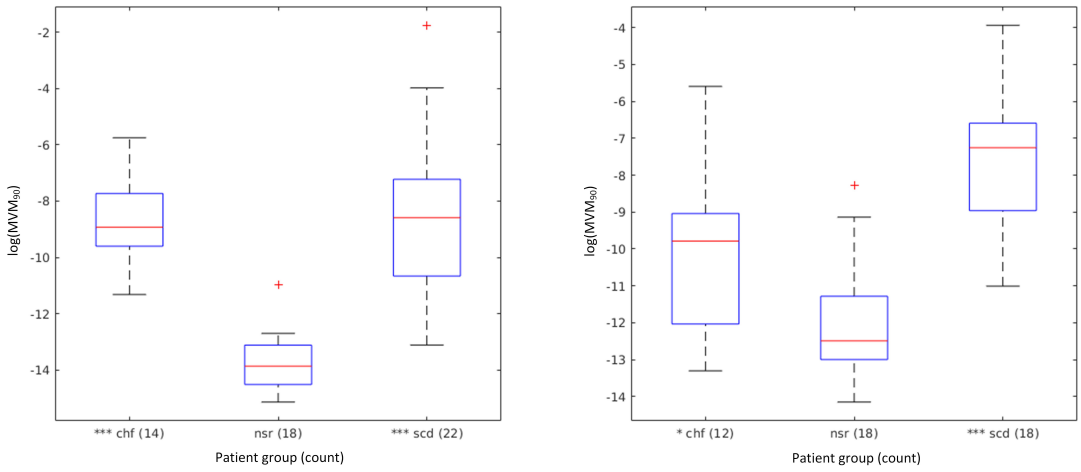

(a) (b)

Figure 6.1: The natural log of the distributions for MVM_{90} in normal sinus rhythm, congestive heart failure and sudden cardiac databases on Physionet is plotted [20]. Distributions that are significantly elevated compared with the NSR distribution with a p-value < 0.05 are indicated with a * and p-value < 0.001 are indicated with ***. **(a)** Channel 1. **(b)** Channel 2.

individuals and 179 controls. Control individuals were age-matched with the individuals with a history of PTSD. The PTSD status of individuals was determined using the CAPS-5 clinical score [155]. Twelve lead Holter ECGs, sampled at 128 Hz, were recorded for each individual. The minimum amplitude resolution for the recordings was 3.2 μV. The average duration of the recordings was 28.08 ± 1.72 hours.

6.2.2 Statistical Analysis

The distributions of MVM_{90}, mean significant TWA in each lead and HRV features were compared between the current PTSD, past PTSD and control groups. The Mann-Whitney U-test was used to test for statistical significance when comparing with the past PTSD group. Given the low number of individuals in the past PTSD group, a non-parametric test was used. The two-sample t-test was used to compare the current PTSD with the control group. The current PTSD group was expected to have elevated MV in the ECG compared to past PTSD and control individuals. P-values ≤ 0.05 were considered to be statistically

significant.

6.2.3 Classification

The classification was performed using linear discriminant analysis (LDA). HRV based features were used separately and in combination with MV features for classification. The log was computed for all features before training the classifier. The 0 values were assigned the minimum value observed for each feature. Taking the log caused the distribution of each feature to be less skewed and improved the classification performance of the LDA classifier.

When classifying with LDA, HRV and MV based features were determined using the wrapper method explained in figure 6.2. In the outer loop, 10-fold CV was performed on the data to evaluate the performance of the main classifier. In the inner loop, the training data for each outer loop iteration was used for feature selection. Backward sequential feature selection with 5-fold CV was used to find the optimal number of features 'N_f' and the associated feature set, for training and testing the main classifier. N_f was varied as 20, 15, 10, 8, 6, 4 and 2. Rad *et al.* adopted a similar method for determining the optimal feature set for their classification task [164].

The above-mentioned nested CV procedure was repeated 8 times to sufficiently sample from the control group. The data in the outer loop was repartitioned for each repetition, using a stratified split into training and test data. The frequency of a feature training the main classifier was stored and used to judge the importance of HRV and MV-based features for classification. The average 10-fold CV AUROC and feature importance after 8 repetitions were reported for each classification task.

Classification tasks

Classification between the current PTSD or past PTSD and current PTSD or control groups was performed. HRV features were considered independently and combined with MV fea-

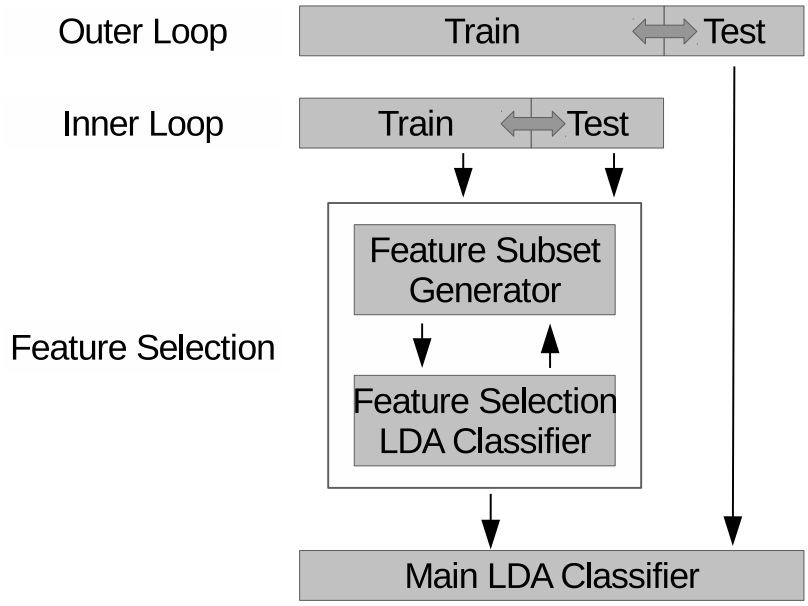

Figure 6.2: The nested cross validation algorithm used to evaluate the classification using HRV and MV features.

tures when evaluating the classification performance of a LDA classifier. HRV features were known to differentiate between individuals with and without PTSD. The goal of the experiment was to determine if including MV features improved this classification. Also, classification was performed between current PTSD and past PTSD individuals. The literature on a comparison between these groups was less common. A quantitaitve comparison was performed for HRV and MV features evaluated for past PTSD individuals compared to current PTSD and control individuals.

6.3 Results

6.3.1 Classification

Table 6.1 gives the average 8-repeated 10-fold CV AUROC for classification as current PTSD or past PTSD and current PTSD or control. The classification was performed using only HRV features and after combining MV features with HRV features. An improvement in the average AUROC was observed for each classification task after including MV features in addition to HRV features. A greater improvement of 10% was observed for clas-

sification as current PTSD or past PTSD after including MV features. For the classification as current PTSD or past PTSD, 10 features were most frequently selected to train the main LDA classifier in the outer loop. The top 15 features based on the frequency of selection were added to table 6.2. Adding the mean significant TWA amplitude measured in leads V1 and V4 improved classification results. For the classification as current PTSD or control individuals, 15 features were most frequently selected to train the main LDA classifier. The top 15 features based on the frequency of selection were added to table 6.3. Adding the MVM_{90} measured in leads III and aVF, and the mean significant TWA measured in lead II resulted in a 5% increase in classification performance.

For classifying current PTSD and controls, features like AC and LF were previously reported as being informative. NN_{mode} was expected to be lower in individuals with PTSD as they had higher resting heart rates compared to control individuals. MV features, i.e. MVM and TWA, measured from the ECG were expected to be higher in individuals with PTSD compared to controls, thereby improving the classification. NN_{IQR}, DC and SDNN were informative in classifying current PTSD from past PTSD individuals. These results were consistent with previous findings [4, 25, 11, 12, 89].

The strongest set of features based on the mode of the N_f distribution was used to train a LDA model and evaluate the classification performance. The top 10 features in table 6.2 were used to classify current and past PTSD individuals. Each feature could be selected at most 80 times. The average 8-repeated 10-fold CV AUROC for this classification is 0.84, see table 6.1. Similarly, the top 15 features in table 6.3 were used to classify current PTSD and control individuals, achieving an AUROC of 0.74.

6.3.2 Computational biomarkers for tracking PTSD status

The following section analyzes the distribution of the MV and HRV features measured in the current PTSD, past PTSD and control individual groups. The ranges of the features were compared between the groups to determine how well PTSD status could be tracked

Table 6.1: The average AUROCs for the classification performance of a LDA classifier trained using HRV and MV features are listed. Combining both sets of features resulted in improved performance. The average AUROC is listed when only HRV features were used for training and HRV in combination with MV features were used.

Current PTSD vs. Past PTSD	**Average 8-Repeated 10 Fold CV AUROC** $\pm \sigma^2$
HRV	0.60 ± 0.08
HRV + MV	0.70 ± 0.06
Suggested Classifier	0.84 ± 0.04
Current PTSD vs. Controls	**Average 8-Repeated 10 Fold CV AUROC** $\pm \sigma^2$
HRV	0.62 ± 0.05
HRV + MV	0.67 ± 0.05
Suggested Classifier	0.74 ± 0.04

Table 6.2: The importance of HRV and MV features in terms of frequency of selection is listed, when performing classification between current and past PTSD individuals.

Feature	**N**	**Feature**	**N**	**Feature**	**N**
NN_{IQR}	54	SDNN	38	LF	32
HF	52	DC	36	ULF	28
NN_{skew}	52	TTLPWR	36	TWA_{V3}	28
TWA_{V1}	43	LF/HF	35	AC	27
VLF	38	TWA_{V4}	35	MVM_{V6}	26

using these features. The hypothesis was each feature would be closest to normal in the control individuals and the deviation from normal would be highest in the current PTSD individuals. The values of the features for past PTSD individuals were expected to lie in between the current PTSD and control individuals. It is important to note the MVM and HRV features were measured over a shorter time duration, i.e., 5-minute and 10-minute windows, respectively. In contrast, the mean significant TWA amplitude was averaged over the entire Holter ECG recording, approximately 28 hours.

Table 6.4 lists the 25^{th}, 50^{th} and 75^{th} percentiles for the distribution of HRV features measured in the current PTSD, past PTSD and control individuals. When comparing to control individuals, the $NN_{variance}$, NN_{IQR}, SDNN, TTLPWR and DC were observed to be significantly lower in the current PTSD individuals with a p-value < 0.05. Frequency domain features other than HF, mean, mode and median of the NN intervals were also observed to be lower in the current PTSD individuals however the difference was not statisti-

Table 6.3: The importance of HRV and MV features in terms of frequency of selection is listed, when performing classification between current PTSD and control individuals.

Feature	**N**	**Feature**	**N**	**Feature**	**N**
NN_{mode}	64	NN_{mean}	46	$NN_{variance}$	37
NN_{median}	62	TTLPWR	45	MVM_{III}	36
LF/HF	57	RMSSD	45	TWA_{II}	36
AC	49	HF	42	ULF	34
VLF	48	LF	40	MVM_{aVF}	33

cally significant. The LF/HF ratio was significantly lower in the current PTSD individuals than past PTSD individuals with a p-value < 0.05. When comparing the ranges of features across the 3 groups, the median of NN_{mean}, NN_{mode}, NN_{median}, $NN_{variance}$, SDNN, ULF, VLF, LF and TTLPWR were observed to be the highest in the control individuals followed by the past PTSD individuals and lowest in the current PTSD individuals. These results suggested PTSD status could be tracked using computational biomarkers for HRV.

Table 6.5 lists the 25^{th}, 50^{th} and 75^{th} percentiles for the distribution of MVM_{90} measured in each of the 12 Holter ECG leads. MVM_{90} in leads V2, V5 and V6 was significantly elevated in current PTSD compared to control individuals with a p-value < 0.05. For lead V2, MVM_{90} was significantly elevated in current PTSD compared to past PTSD individuals with a p-value < 0.05. For lead aVF, MVM_{90} was significantly elevated in current PTSD compared to control individuals with a p-value < 0.01 and past PTSD individuals were significantly elevated than control individuals with a p-value < 0.05. These results suggested MVM_{90} was highest in current PTSD individuals followed by past PTSD individuals and lowest in the controls. Thus MVM_{90} could also be used to distinguish between the 3 different PTSD states.

The 25^{th}, 50^{th} and 75^{th} percentiles for the distribution of mean significant TWA amplitude, measured as explained in section 4.2.1, for each analysis group are listed in table 6.6. The mean significant TWA amplitude in the current PTSD group was significantly elevated than the control group in lead V4 with a p-value < 0.05, leads II, III, V3 with a p-value < 0.01 and leads aVF, V5, V6 with a p-value < 0.001. Current PTSD individuals

Table 6.4: The 25th (Q1), 50th (median) and 75th (Q3) percentiles for the distributions of the heart rate variability features measured in the current PTSD, past PTSD and control groups are listed. Features indicated with a * were significantly lower in the current PTSD group when compared to the past PTSD group with a p-value ≤ 0.05. Features indicated with a † were significantly lower in the current PTSD group when compared to the control group with a p-value ≤ 0.05.

Feature	Median [Q1, Q3]		
	Current PTSD (33)	Past PTSD (21)	Controls (179)
NN_{IQR} (ms)	54.69, [33.11, 72.07] †	64.06 [48.73, 83.79]	63.28 [50.00, 82.81
SDNN (ms)	46.78 [29.51, 72.84] †	52.86 [44.80, 66.83]	61.98 [49.48, 76.85]
LF (ms^2)	391.96 [158.91, 1161.28]	746.54 [431.40, 1238.95]	788.67 [446.63, 1209.54]
AC (ms)	-10.42 [-15.14, -7.73]	-12.11 [-13.44, -9.80]	-11.51 [-16.38, -8.64]
DC (ms)	9.51 [6.02, 12.58] †	11.19 [8.98, 13.86]	11.05 [7.80, 14.80]
LF/HF	1.61 [0.77, 2.60] *	3.16 [1.82, 4.37]	2.73 [1.37, 4.63]
NN_{mean} (ms)	990.28 [875.55, 1122.83]	1008.54 [910.23, 1069.19]	1056.96 [945.99, 1164.46]
NN_{median} (ms)	1000.00 [889.26, 1131.35]	1029.69 [913.67, 1078.52]	1067.77 [951.56, 1164.84]
NN_{mode} (ms)	1000.00, [887.11, 1105.47]	1029.69 [915.67, 1087.50]	1074.80 [964.06, 1176.56]
$NN_{variance}$ (ms^2)	2401.39, [923.24, 5665.37] †	2965.17 [2164.09, 5346.31]	4491.99 [2783.18, 6164.14]
NN_{skew}	-0.61 [-1.58, -0.20]	.0.87 [-1.57, -0.44]	-0.87 [-1.25, -0.43]
NN_{kurt}	4.70 [3.65, 8.09]	4.55 [2.97, 5.70]	4.92 [3.76, 6.87]
RMSSD (ms)	31.52 [17.95, 46.20]	25.60 [20.48, 34.22]	28.12 [23.21, 41.56]
pnn50	0.06 [0.01, 0.17]	0.04 [0.02, 0.09]	0.06 [0.03, 0.16]
ULF (ms^2)	258.31 [82.38, 742.99]	428.45 [181.66, 1172.36]	442.80 [182.08, 862.59]
VLF (ms^2)	1251.74 {458.12, 2731.37]	1429.75 [931.41, 3222.99]	2462.21 [1392.52, 3610.84]
HF (ms^2)	353.20 [93.00, 601.46]	208.48 [115.57, 441.92]	289.22 [132.69, 557.76]
TTLPWR (ms^2)	2531.32 [1077.46, 5786.99] †	2953.81 [2237.75, 5561.45]	4464.26 [2961.70, 6293.46]

Table 6.5: The 25th, 50th and 75th percentiles for the distribution of the natural log of MVM_{90} in the current PTSD, past PTSD and control groups are listed. ECG leads with significantly elevated MVM_{90} in the current PTSD group compared with the past PTSD group were indicated with * for a p-value ≤ 0.05. Leads with significantly elevated MVM_{90} in the current PTSD or past PTSD group compared to the control group were indicated with a † for a p-value ≤ 0.05 and †† for a p-value ≤ 0.01.

	ln(Median MVM_{90}) (ln($beats$))[Q1, Q3]		
ECG lead	**Current PTSD**	**Past PTSD**	**Control**
I	-11.59 [-12.17, -10.75]	-12.14 [-13.79, -10.35]	-11.91 [-12.87, -10.79]
II	-11.77 [-13.44, -10.59]	-11.61 [-12.74, -10.86]	-12.08 [-12.77, -10.94]
III	-10.44 [-11.55, -9.38]	-10.39 [-11.11, -8.92]	-10.13 [-11.32, -8.85]
aVR	-10.19 [-14.24, -8.47]	-9.35 [-14.70, -7.77]	-10.13 [-14.04, -9.00]
aVL	-9.74 [-11.61, -8.40]	-9.38 [-11.48, -8.42]	-10.18 [-11.23, -8.62]
aVF	-11.06 [-12.84, -9.95]††	-10.43 [-11.79, -9.38]†	-11.44 [-12.20, -10.16]
V1	-9.70 [-12.74, -8.28]	-11.24 [-11.63, -10.23]	-10.80 [-12.59, -8.44]
V2	-10.32 [-13.18, -8.82]* †	-12.30 [-13.63, -11.53]	-12.16 [-13.48, -10.33]
V3	-11.20 [-12.74, -9.60]	-11.55 [-13.35, -9.24]	-12.05 [-13.17, -10.55]
V4	-11.83 [-13.52, -10.36]	-12.02 [-13.16, -10.98]	-12.33 [-13.32, -11.21]
V5	-12.34 [-13.59, -10.85]†	-12.00 [-13.46, -10.57]	-12.50 [-13.32, -11.52]
V6	-11.85 [-13.53, -10.06]†	-11.34 [-12.64, -10.59]	-11.89 [-12.84, -10.83]

Table 6.6: The 25th, 50th and 75th percentiles for the distribution of mean significant TWA in the current PTSD, past PTSD and control groups are listed. ECG leads with significantly elevated mean TWA in the current PTSD and control groups compared with the past PTSD group, were indicated with * for a p-value ≤ 0.05 and ** for a p-value ≤ 0.01. ECG leads with significantly elevated mean TWA in the current PTSD group compared to controls were indicated with † for a p-value ≤ 0.05, †† for a p-value ≤ 0.01 and † † † for a p-value ≤ 0.001.

	Median mean TWA (μV) [Q1, Q3]		
ECG lead	**Current PTSD**	**Past PTSD**	**Control**
I	0.87 [0.54, 1.27]	0.62 [0.37, 0.88]	0.83 [0.62, 1.17]*
II	1.74 [1.20, 2.70]* ††	1.20 [0.85, 1.76]	1.67 [1.20, 2.12]*
III	1.55 [1.17, 2.51]††	1.22 [0.71, 1.81]	1.57 [1.12, 2.15]
aVR	0 [0, 1.00]	0.36 [0, 1.55]	0.34 [0, 1.15]
aVL	0.94 [0.41, 1.47]	0.85 [0.40, 1.39]	0.85 [0.42, 1.45]
aVF	1.66 [1.14, 2.92]† † †	1.34 [0.81, 1.80]	1.60 [1.19, 2.28]
V1	0.62 [0, 1.45]	0.88 [0.48, 1.24]	0.88 [0.01, 1.42]
V2	1.20 [0.56, 1.92]	1.05 [0.54, 1.70]	1.38 [0.93, 2.02]
V3	1.58 [1.17, 3.80]* ††	1.19 [0.88, 1.82]	1.58 [1.05, 2.23]
V4	1.49 [1.02, 2.70]* †	0.98 [0.67, 1.41]	1.56 [1.03, 2.14]**
V5	1.38 [0.96, 2.79]* † † †	0.96 [0.60, 1.37]	1.39 [0.99, 1.91]*
V6	1.22 [0.94, 2.56]** † † †	0.88 [0.60, 1.19]	1.19 [0.87, 1.69]**

had significantly elevated mean significant TWA than past PTSD individuals in leads II, V4, V5, V6 with a p-value < 0.05, lead V6 with a p-value < 0.01. In contrast to MVM and HRV features, mean significant TWA amplitude was lower in past PTSD individuals compared to control individuals. The mean significant TWA amplitude was significantly lower in leads I, II, V4, V5 with a p-value < 0.05 and lead V6 with a p-value < 0.01. The results suggested past PTSD individuals experienced less stress over a longer duration of approximately 24 hours. The result could be the result of rehabilitation therapy or medication, through which they were trained to suppress the negative thoughts and emotions that caused stress consciously. This result was consistent with the average HRV measured in 24 hours on past PTSD individuals by Vaccarino *et al.* [10].

6.4 Discussion

Previous studies leveraged HRV to differentiate current PTSD from control individuals [4]. In addition to identifying current PTSD individuals from controls, the analysis presented here attempted to differentiate a more subtle class of PTSD patients - current from past PTSD individuals - by measuring HRV and MV in the ECG. MV of the ECG can be assumed to have a weak correlation with HRV measurements. HRV metrics only measured the variability in the beat-to-beat intervals in ECG, capturing a subset of the information present. MV measurements captured the variability information in the entire ECG beat. This study also showed variability in ECG beats with a period greater than 2 carried prognostic information for PTSD detection in addition to TWAs, which measured variability in a period of 2 beats. This observation was consistent with previous findings [30]. The linear decision boundary formed by a LDA classifier provided satisfactory classification performance as it was less likely to overfit the training data. A data-driven approach was used to identify important features for classifying PTSD status. Many of the HRV features identified as important, i.e. LF, HF, NN_{IQR}, AC, DC, $NN_{mode/median/mean}$ and SDNN, were consistent with previous findings [4, 25, 89]. The chest leads V3, V4, V5, V6 had significantly elevated TWAs in the current PTSD compared to past PTSD individuals. The chest leads V3-V6 were observed to be less noisy and were located closer to the ventricles. Therefore they were more sensitive at recording the depolarization and re-polarization of the ventricles. Mean significant TWA evaluated in leads V1 and V4 were important features for classifying individuals as current and past PTSD. MVM evaluated in leads aVF and III were important in classifying current PTSD individuals and controls, the aVF lead particularly was strongly aligned with the direction of ventricular depolarization. This work reinforced the strength of the repeated nested CV approach, which can be applied to similar classification problems to identify physiologically important features.

Stress-induced increase in MV of ECG was consistent with previous studies [11, 12,

96], which provided the physiological basis for these observations. In this study, we trained an algorithm to measure computational biomarkers for HRV and MV in the ECG to determine the PTSD status of an individual. Automating this detection process improved the chances of early detection, reduced the chances of human error and burden on human intervention, and improved standardization of the PTSD detection test. Currently, PTSD status was determined using the CAPS-5 [155], a 30 item clinician-administered structured interview. Responses were subjective on a scale of 0-4, therefore one individual's response to *In the past week, have you tried to avoid thoughts or feelings about (EVENT)?* as '1-Mild' may not be the same as another individual's. Using biometric data like ECG for computing quantitative bio-markers reduced inter-patient variability when conducting a test to classify an individual as current, recovered PTSD or control.

Comparing MV in the current and past PTSD group to the controls, the current PTSD group had significantly elevated MVM and mean TWA compared to the past PTSD and control groups. MVM_{90} in lead aVF was significantly elevated for current and past PTSD compared to control individuals. For lead V2, MVM_{90} was significantly elevated in current PTSD compared to past PTSD and control individuals, confirming our hypothesis current PTSD individuals showed the highest deviation from control individuals followed by past PTSD individuals. A similar trend was observed in the HRV parameters, i.e., NN_{mean}, NN_{mode}, NN_{median}, $NN_{variance}$, ULF, VLF and LF had the lowest medians in the current PTSD group, followed by the past PTSD group and were highest in the control individuals. NN_{IQR}, SDNN, DC, $NN_{variance}$ and TTLPWR were significantly reduced in the current PTSD than the control individuals, with LF/HF in current PTSD being significantly lower than past PTSD individuals. A slightly different trend was observed for the mean significant TWA amplitude, it was observed to be significantly elevated in current PTSD and controls in leads II, V3, V4, V5 and V6 compared to past PTSD individuals. This could be explained by the fact the mean TWA amplitude was computed over approximately 28 hours. During this duration, treatment and medication received by the past PTSD individ-

uals would have trained them to consciously suppress thoughts or emotions that caused them to feel stressed. MVM_{90} was measured over shorter windows of 5-minutes and was specifically designed to capture moments of heightened stress. HRV parameters were also evaluated over shorter 10-minute windows and did not capture the effects of therapy observable on longer duration recordings of approximately 28 hours. Given the reasonably low number of past PTSD individuals, the experiment could be repeated with a larger number of past PTSD individuals and investigated further. The mean significant TWA was observed to be significantly elevated in current PTSD compared to controls in leads II, III, aVF, V3, V4, V5 and V6, consistent with our initial hypothesis.

CHAPTER 7

APPLICATION OF NOVEL MORPHOLOGICAL VARIABILITY ANALYSIS TO ARTERIAL BLOOD PRESSURE FOR PREDICTION OF SEPSIS

7.1 Data

The blood pressure waveform data obtained from adult patients admitted to the ICU at Emory university hospital, Atlanta, GA, USA, was used in this analysis. The Bedmaster system (Excel Medical Electronics, Jupiter, FL) was used to record the data. The Bedmaster system was a third-party software connected to the hospital's patient monitors for the extraction and storage of high-resolution waveform data, sampled at 240 Hz. The annotation algorithm implemented by Zong *et al.* was used to create automated annotations for the blood pressure signals [134]. The computed annotations were further adjusted to correspond precisely to the valleys between blood pressure signal peaks. A signal quality metric for blood pressure developed by Sun *et al.* [165] was used to identify clean segments in the data for subsequent analysis. Signals with at least 30 minutes of valid data each hour, for 10 hours before sepsis onset, were used to create a group of septic patients. A similar check was used to create a control group of non-septic patients. Non-septic patients were assigned arbitrary times for sepsis onset. These times were sampled from the distribution for the time interval from the beginning of a record to sepsis onset t_0, derived from septic patients. After applying these checks, data from 111 septic patients and 94 non-septic patients remained. Table 7.1 lists patient demographic information. No significant differences between the septic and control individuals were observed in age or length of stay (LOS). The two-sample t-test was used to test for significant differences between groups. We used data from these patients to determine changes in MV of ABP in septic versus non-septic patients. We then evaluated the classification performance of MV of ABP and transient

hypotension to predict sepsis onset.

Table 7.1: The demographic and characteristic information for the patient cohort used in this study is listed. IQR - Interquartile range.

Characteristic	Overall	Sepsis	Controls
Patient, n	205	111	94
Male, n	81	41	40
Age (yr.), median (IQR)	59 (49 - 67)	58 (49.5 - 66.8)	61 (49 - 69)
ICU LOS (days), median (IQR)	11.5 (5-20)	10.5 (5 - 21)	13 (6 - 20)
In hospital deaths, n	23	15	8
Self reported race, n			
Black or African American	70	37	33
White	104	57	47
Unknown/Other	18	10	8
Multiple	5	2	3
Asian	8	5	3
Self reported ethnicity, n			
Not Hispanic or Latino	149	76	73
Hispanic or Latino	8	7	1
Unknown or Declined	48	28	20

7.2 Arterial blood pressure analysis

MV of ABP was calculated as described in section 4.3.2A. Figure 7.1 summarizes the process. Hypotension analysis was performed as described in section 4.3.2B and was used as a benchmark to compare against when classifying individuals as septic or non-septic using MV of ABP.

7.3 Classification

For classification, we used a balanced set of 94 patients from each of the septic and non-septic groups. When computing MV of ABP, we obtained a maximum of 120 MV values for each patient, given all data windows were clean enough for analysis. The 75^{th} percentile (pctl) of the MV energies was measured per hour to characterize the higher MV range. Thus for each patient, 10 MV values, one for each hour, were used to create a feature vector. The

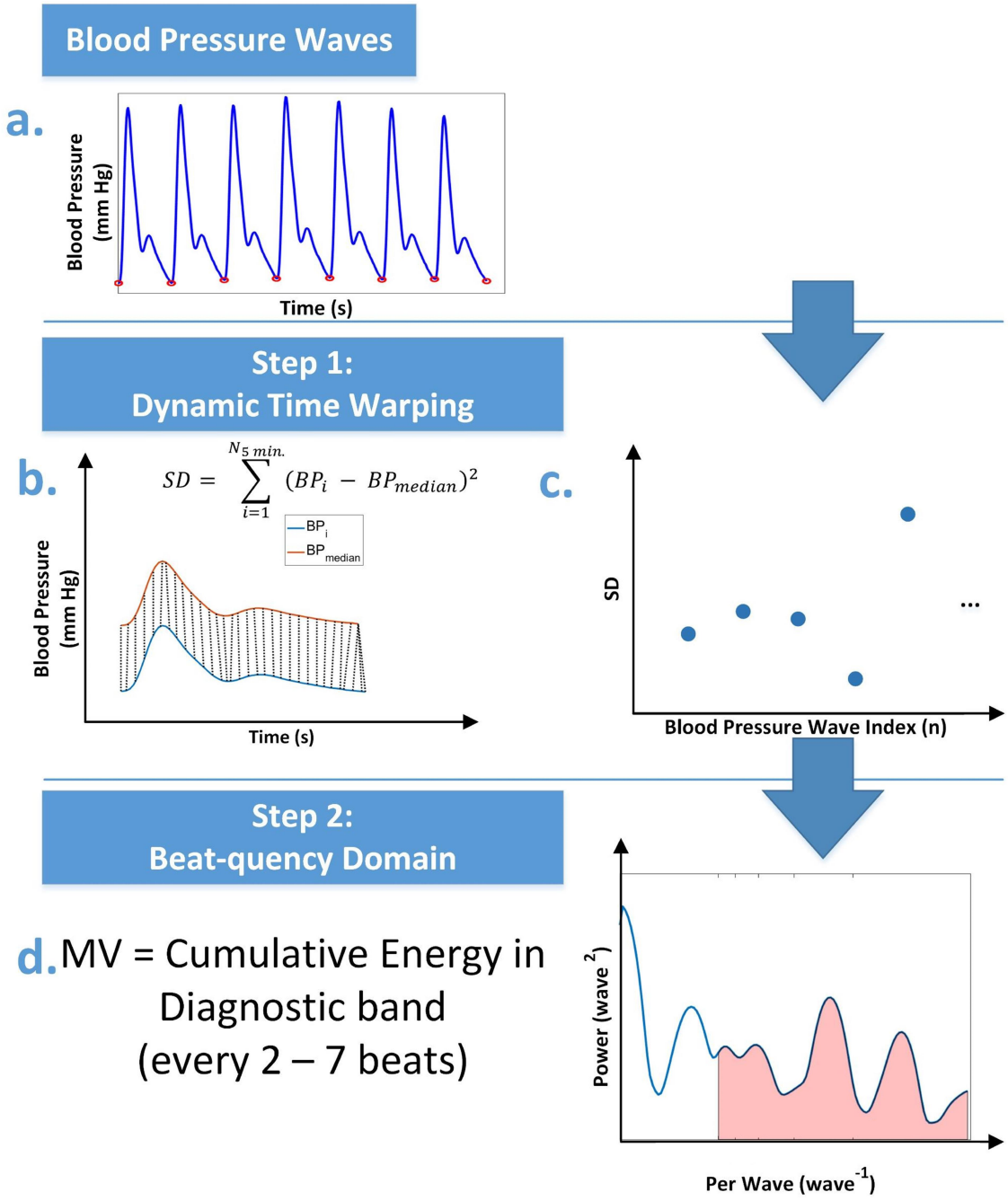

Figure 7.1: A graphical illustration of the process for computing the MV for arterial blood pressure waveform signals.

number of hypotensive event onsets in individual hours for 10 hours was used to create a second set of feature vectors, each with ten elements. A logistic regression classifier was used to perform classification using the MV-based features and hypotension-based feature separately. The average 10-fold CV AUROC was reported for each case.

7.4 Results

The 75^{th} pctl of the MV energy measurements was computed for each hour, giving 10 features per patient. Each set of values was divided by the difference between the set's maximum and minimum value observed in the set. Normalizing by the maximum difference caused the variation in each set to be over a range of 1. An average was computed across the normalized sets to detect a trend in the average septic and average non-septic patient. Figure 7.2a shows the trend in MV in the average septic patient over 10 hours before sepsis onset compared to the average non-septic patient, figure 7.2b. Based on figure 7.2, septic patients, on average, experienced a drop in MV of ABP as they were about to experience sepsis onset.

For the first 8 hours, septic patients experienced a gradual drop in the MV of ABP. An external intervention caused a sharp rise in the final 2 hours, i.e., vasoconstrictors increased the septic patients' blood pressure before sepsis onset. The decreasing trend is apparent with the robust fit line fitted to the data points in figure 7.2a. In non-septic patients, there is no apparent change, figure 7.2b. Figure 7.3a gives the histogram for the hour in which each septic patient experienced the maximum MV of ABP before sepsis onset, consistent with the observation in 7.2a. For non-septic patients, there was no specific hour in which a significant fraction of patients experienced the maximum MV of ABP, observed as a median hour of 5 in figure 7.3b.

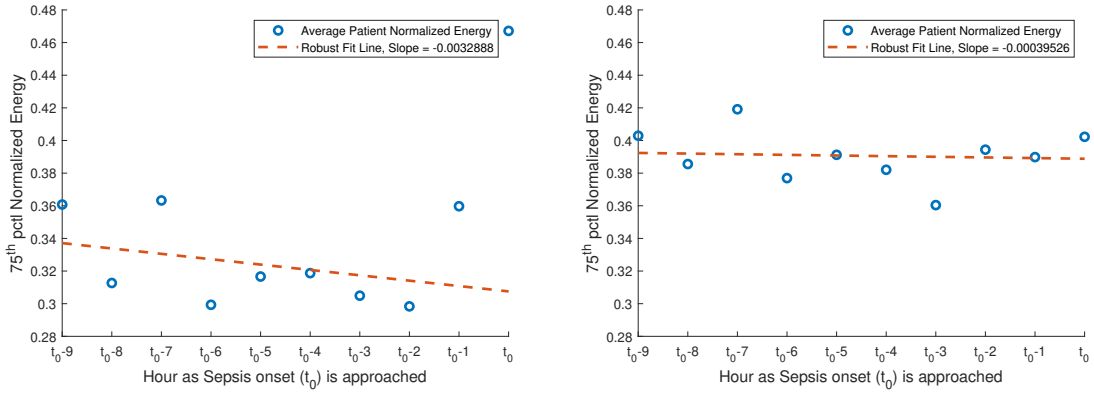

(a) (b)

Figure 7.2: **(a)** The figure shows the average septic patient for the 111 septic records. The 75th percentile of the hourly MV energy measurements was computed, giving ten values for each patient. Each set of 10 measures was divided by the difference between the maximum and minimum value in the set. The resulting normalized energy sets were averaged to create an average patient characterizing the septic class, represented by blue dots. The red dotted robust fit line (RFL) has a negative slope indicating septic patients on average experienced a drop in MV of ABP as they were about to experience sepsis onset. **(b)** The figure shows the average normalized hourly 75th percentile energy measurements for non-septic patients as blue dots and the RFL as a dotted red line. The RFL with a slope of approximately 0 indicated non-septic patients on average experienced no significant trend in MV of ABP.

Table 7.2: Average 10-fold CV AUROC for classification using transient hypotension features and MV of ABP features. The results showed MV of ABP based classification is more predictive of sepsis onset than transient hypotension.

Features	**10-fold CV AUROC**
Hypotension	0.52
MV of ABP	0.67

7.4.1 Classification

For classification using MV of ABP, we used the 75th pctl of energy measurements computed over each hour as an input to our classifier. The classification was performed using logistic regression to find a separating hyperplane in a higher dimension. The average AUROC for 10-fold CV was 0.67, reported in table 7.2.

We compared our classification results for MV with a classifier that detects the number of hypotensive event onsets each hour. To optimize our algorithm for the current case, we

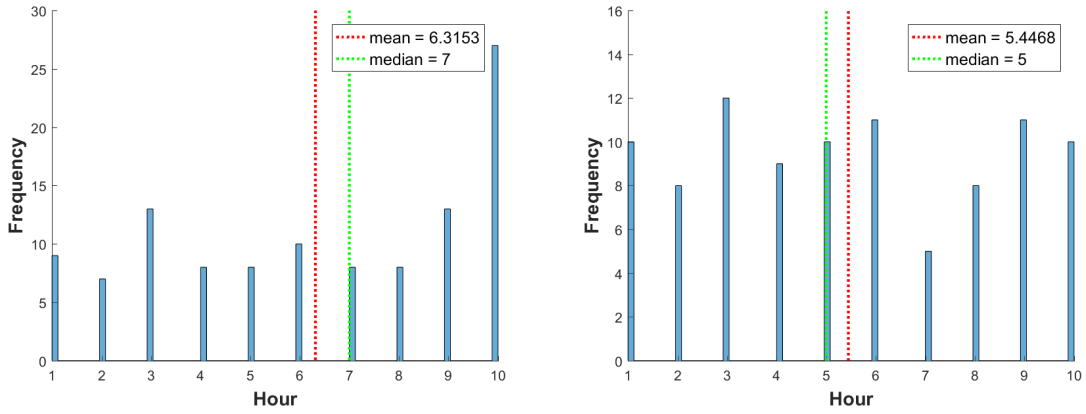

(a) (b)

Figure 7.3: The figure shows the distribution for the hour of occurrence for the maximum 75th percentile MV in **(a)** the septic group and **(b)** non-septic group. A high proportion of septic patients exhibited the highest MV in the final hour before sepsis onset. Non-septic patients experienced their peak MV in any arbitrary hour with a median hour of 5.

varied the length of the window for computing the median blood pressure from which to measure the pressure drop, the threshold below which the MAP and SBP must drop and the minimum drop. For our data set, the highest 10-fold CV AUROC was achieved for a window length of 9 minutes, MAP threshold of 55 mmHg, SBP threshold of 75 mmHg, and pressure drop of 17 mmHg, figure 7.4. The number of hypotensive event onsets per hour evaluated using this set of parameters was used for classification using a logistic regression classifier. The average 10-fold CV AUROC was 0.52, reported in table 7.2.

7.5 Discussion

Until now, MV of ABP waveform data was not considered a predictor of sepsis onset. In this study, a drop in MV of ABP was related to sepsis onset in patients admitted to the ICU. Typically, variations in the dynamics of heart rate and related physiological measures were used to predict or detect diseases, e.g., heart rate variability for heart failure [166] and sepsis [111, 167]. These measurements captured changes similar to those in the R peak to R peak intervals obtained from ECG, a subset of the information present in the physiologic waveform data. Measuring variability in the entire waveform on a beat to beat basis can

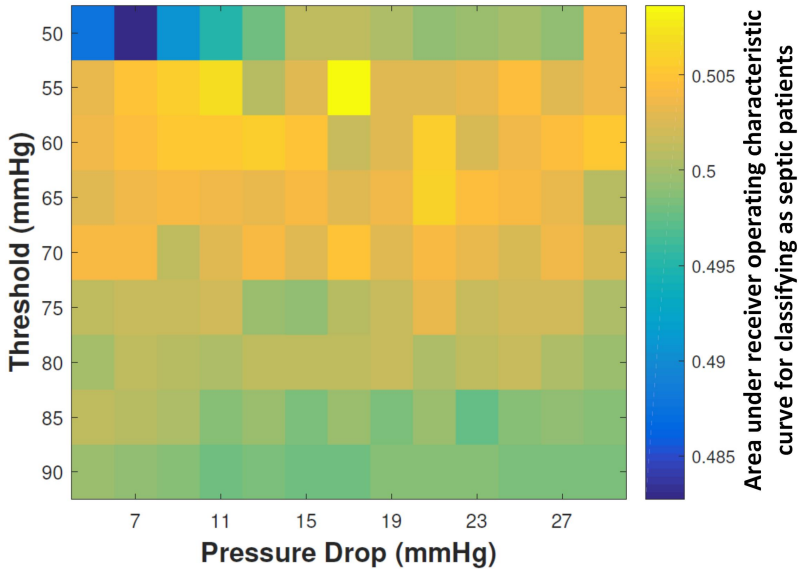

Figure 7.4: The heat map for classification of septic patients using the number of hypotensive event onsets per hour. A 9-minute window was used for evaluating the median pressure reference to compute the drop in MAP and SBP. The average ten-fold CV AUROC is plotted for a window size of 9 minutes used for calculating the reference pressure. The threshold below which MAP drops were classified as low blood pressure and the minimum pressure drop, were varied as shown. The optimal parameter set for hypotension-based classification was a window size of 9 minutes, a MAP threshold of 55 mm Hg (75 mm Hg for SBP), and a pressure drop of 17 mm Hg.

lead to more reliable differentiation between normal and abnormal physiologic signals. Liu *et al.* identified individuals at low to moderate risk of ACS had elevated MV of their ECG [30]. Like the ABP waveform, MV can be applied to other physiologic waveform data to study its predictive value for life-threatening diseases similar to sepsis. These predictive algorithms have intangible value as they allow care providers to apply preventive measures before a more potent manifestation of the disease in patients.

The algorithm looked at 10 hours of data before sepsis onset and differentiated septic individuals from non-septic individuals with an AUROC of 0.67. In contrast, hypotension was considered to be predictive of sepsis onset. However, as an independent variable, the number of hypotensive event onsets in each of 10 hours yielded a predictive AUROC of 0.52. This finding cast doubt on a commonly accepted belief drop in blood pressure, at least independently associated with sepsis onset.

Future work includes using more data, possibly 24 hours [30] before sepsis onset, which may increase prediction accuracy. Additionally, incorporating parameters like patient temperature, HR, BR, oxygen saturation (O_2Sat), white blood cell count and other clinical information shown to be predictive of sepsis [109], with MV of ABP, may improve prediction accuracy several hours before sepsis onset. For high BRs, as experienced by septic individuals, analysis in section 5.2.3 showed the modulation of waveform signals due to respiration caused MV that is statistically significant compared to respiration free signals. Increased energy measured in the every 2 to 7 wave beat-quency band may be affected due to respiration-induced modulation of the blood pressure waves rather than being caused by some underlying physiologic abnormality. In future studies, we aim to account for the effects of BR and HR when measuring and predicting outcomes using MV of the ABP signal. More powerful deep neural network classifiers like recurrent neural networks (RNNs), better suited for sequentially ordered data like MV of ABP evaluated in each hour, will be trained to predict sepsis onset.

CHAPTER 8
APPILCATION OF NOVEL MORPHOLOGICAL VARIABILITY ANALYSIS FRAMEWORK TO PHOTOPLETHYSMOGRAM FOR DETECTION OF COARCTATION OF THE AORTA

8.1 Data

A cohort of 18 neonates with COA requiring surgical repair was identified and matched with 18 control neonates who met inclusion and exclusion criteria listed in section 4.4. Table 8.1 lists patient group characteristics. No significant differences in gender or ethnicity were observed. Gender did not affect the measured PPG waveforms as the underlying vascular anatomy is the same for monitoring PPG. For the control group, 9 patients (50%) had some form of anomalous pulmonary venous return, 4 (22%) had neonatal arrhythmias, 2 (11%) had valvar abnormalities and 3 others had cardiomyopathy, pulmonary hypertension and a pericardial tumor (representing 6% each).

8.2 Results

8.2.1 Preoperative COA vs unaffected controls

An almost linear association between the rates of rise and fall with the heart rate was observed, figure 5.6. Presurgical waveform characteristics were calculated for the COA and control patients and shown in table 8.2. The two significant characteristics were (p-value ≤ 0.01) the MF in the lower extremity and the difference between the MF of the upper extremity and the lower extremity (ΔMF in table 8.2 and figure 8.1). The Mann-Whitney U-test was used to identify statistically significant differences in features evaluated for two different groups.

Table 8.1: The demographic information of each cohort and the primary diagnosis resulting in neonatal admission of the control group to the cardiac intensive care unit are reported.

	Control		**Coarctation**	
Gender				
Male	11	61%	9	50%
Female	7	39%	9	50%
Race/Ethnicity				
African American	8	44%	5	28%
White	8	44%	13	72%
Hispanic	2	11%	3	17%
Other/unanswered	2	11%	0	0%
Diagnoses of control group				
Pulmonary vein	9	50%		
Arrhythmia	4	22%		
Valvar abnormality	2	11%		
Cardiomyopathy	1	6%		
Pulmonary hypertension	1	6%		
Tumor	1	6%		

Table 8.2: The values for the following slope features are reported, the AR, the AF, the MR and the MF. The slope feature units are normalized ampltiude/time and subscripts indicated upper (u) vs lower (l) extremity acquisition site. The median, 1st quartile (Q1) and 3rd quartile (Q3) are reported for each feature. The Δ indicated the difference between the upper and lower extremity for that feature. Features significantly different between the COA and control groups with a p-value < 0.01 are marked with **. The Mann-Whitney U-test was used to test for statistical significance.

	Median (Q1, Q3)		
Preop feature	Control	Coarctation	p-value
AR_u	4.66 (4.38, 5.07)	4.52 (4.41, 4.88)	0.16
AF_u	-1.72 (-1.87, -1.53)	-1.67 (-1.75, -1.53)	0.96
MR_u	5.05 (4.71, 5.46)	4.98 (4.76, 5.26)	0.24
MF_u	-2.63 (-2.81, -2.47)	-2.64 (-2.73, -2.51)	0.60
AR_l	4.90 (4.42, 5.32)	4.90 (4.47, 5.31)	0.91
AF_l	-1.53 (-1.65, -1.41)	-1.49 (-1.59, -1.35)	0.38
MR_l	5.27 (4.77, 5.68)	5.32 (4.87, 5.70)	0.84
MF_l **	-2.60 (-2.67, -2.52)	-2.34 (-2.50, -2.30)	0.009
ΔAR	-0.22 (-0.52, -0.13)	-0.12 (-0.45, 0.02)	0.50
ΔAF	-0.12 (-0.31, -0.02)	-0.20 (-0.26, -0.01)	0.22
ΔMR	-0.22 (-0.44, -0.11)	-0.12 (-0.46, 0.02)	0.54
ΔMF **	-0.07 (-0.2, 0.08)	-0.24 (-0.38, -0.13)	0.004

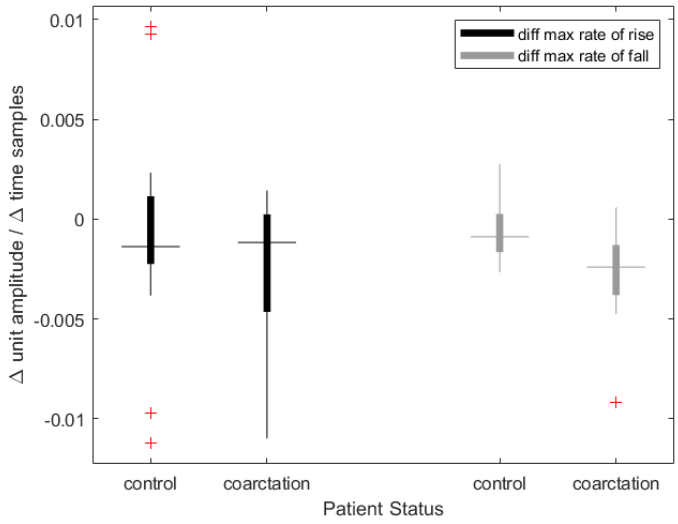

Figure 8.1: Preoperative differences in the maximum rates of rise and fall. The y-axis represents a normalized slope, change in normalized waveform amplitude divided by the change in time. There was no significant difference in the maximum rate of rise between groups (p-value 0.54), but a significant difference in the maximum rate of fall was observed between the control and the coarctation group (p-value 0.004).

8.2.2 Postoperative COA vs unaffected controls

For the 18 neonates with COA, one neonate did not have PPG data recorded from an upper extremity postoperatively. Therefore, they were not included in the postop statistical analysis. Table 8.3 shows the same waveform characteristics evaluated postoperatively. Here, we note statistical significance in the MF in both the upper and lower extremities but not in the ΔMF, indicating that the difference normalized after surgical correction of the COA (see figure 8.2).

8.2.3 Preoperative COA vs postoperative COA

Table 8.4 showed the COA group compared to themselves preoperatively vs postoperatively relative to the COA repair.

Table 8.3: A comparison of values for COA s/p surgical repair and control subjects. The values for the following slope features are reported, the AR, the AF, the MR and the MF. The slope feature units are normalized ampltiude/time and subscripts indicated upper (u) vs lower (l) extremity acquisition site. The median, 1st quartile (Q1) and 3rd quartile (Q3) are reported for each feature. The Δ indicated the difference between the upper and lower extremity for that feature. Features significantly different between the coarctation of the aorta and control groups with a p-value < 0.05 are marked with **. The Mann-Whitney U-test was used to test for statistical significance.

	Median (Q1, Q3)		
Postop feature	Control	Coarctation	p-value
AR_u	4.66 (4.38, 5.07)	4.68 (4.44, 4.86)	0.46
AF_u	-1.72 (-1.87, -1.53)	-1.65 (-1.79, -1.54)	0.59
MR_u	5.05 (4.71, 5.46)	5.04 (4.84, 5.36)	0.44
MF_u **	-2.63 (-2.81, -2.47)	-2.47 (-2.56, -2.26)	0.046
AR_l	4.90 (4.42, 5.32)	4.75 (4.56, 5.21)	0.79
AF_l	-1.53 (-1.65, -1.41)	-1.51 (-1.62, -1.37)	0.40
MR_l	5.27 (4.77, 5.68)	5.12 (4.92, 5.58)	0.62
MF_l **	-2.60 (-2.67, -2.52)	-2.27 (-2.46, -2.23)	0.008
ΔAR	-0.22 (-0.52, -0.13)	-0.04 (-0.32, 0.13)	0.66
ΔAF	-0.12 (-0.31, -0.02)	-0.07 (-0.16, 0.02)	0.99
ΔMR	-0.22 (-0.44, -0.11)	-0.05 (-0.32, 0.17)	0.61
ΔMF	-0.07 (-0.2, 0.08)	-0.04 (-0.29, -0.02)	0.93

Table 8.4: PPG features evaluated for COA before and after surgical repair. The values for the following slope features are reported, the AR, the AF, the MR and the MF. The slope feature units are normalized ampltiude/time and subscripts indicated upper (u) vs lower (l) extremity acquisition site. The median, 1st quartile (Q1) and 3rd quartile (Q3) are reported for each feature. The Δ indicated the difference between the upper and lower extremity for that feature. Features significantly different between the coarctation of the aorta and control groups with a p-value < 0.05 marked with *. The Mann-Whitney U-test was used to test for statistical significance.

	Median (Q1, Q3)		
Waveform feature	Preoperative	Postoperative	p-value
ΔAR	-1.20 (-4.50, 0.19)	-0.16 (-3.30, 2.60)	0.13
ΔAF	-2.00 (-2.60, -0.09)	-0.63 (-1.70, 0.34)	0.20
ΔMR	-1.20 (-4.60, 0.24)	-0.14 (-3.30, 3.00)	0.16
ΔMF *	-2.40 (-3.80, 1.30)	-0.30 (-2.90, 0.71)	0.03

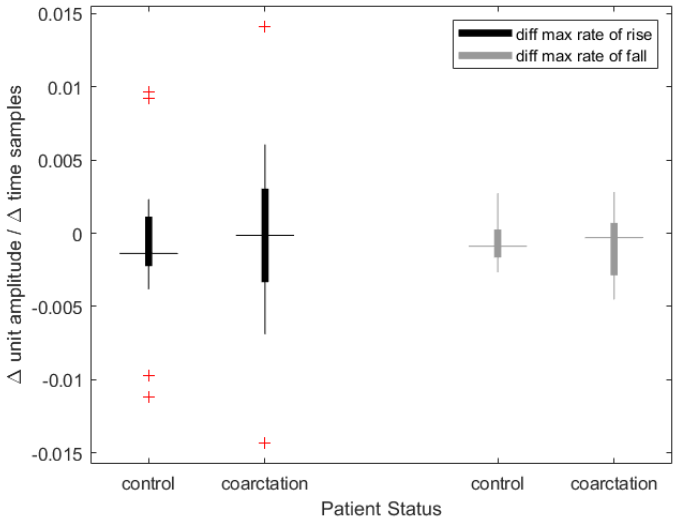

Figure 8.2: Postoperative differences in the maximum rates of rise and fall. The y-axis represents a normalized slope, normalized waveform amplitude divided by time. Following surgical repair of COA, no significant difference was observed in the maximum rate of rise (p-value 0.61) or fall (p-value 0.93) between the groups.

8.3 Leave one out cross validation

To test the ability of our algorithm to identify patients with COA, we implemented LOOCV stratified by patient as the number of subjects was too few to split the data set into a train and test set. The ROC curve was generated for the LOOCV performance of the classifier. The MF in the upper and lower extremity were used to classify subjects in the COA or control groups. A LDA classifier achieved an average accuracy of 72%. The ROC curve was given in figure 8.3. The AUROC was 0.78. The suggested operating point, indicated by a red circle, achieved a sensitivity of 0.61, a specificity of 0.94 and approximately provided a 33% increase in the sensitivity of detection of COA compared to current screening.

8.4 Discussion

Our results showed that it was possible to correctly detect COA by calculating slope discrepancies of PPG waveforms recorded from the upper and lower extremities of neonates. This was most notable when comparing the difference between the maximum rate of fall

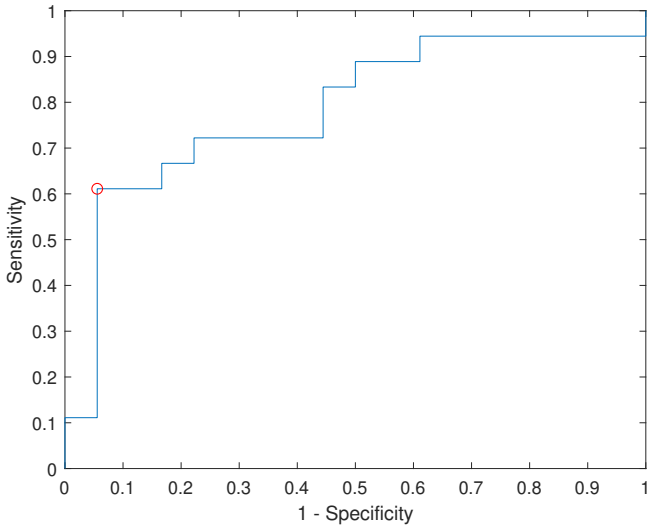

Figure 8.3: The receiver operating characteristic curve for classifying subjects as having a COA or control using linear discriminant analysis. The area under the curve is 0.78. The suggested operating conditions, indicated by the red circle, achieved a sensitivity of 0.61 and a specificity of 0.94.

of the PPG signal in the upper and lower extremities. In our data, the MF remained significant in the lower extremity for the COA group when compared to controls following surgical correction. However, the ΔMF did not, emphasizing the need for a recording from an upper extremity as a reference when measuring the rate of flow in the lower extremity. The observed difference in ΔMF between COA and controls resolved following surgical correction suggesting that the obstruction of COA limited the maximum rate of blood flow in the lower extremities. This corresponded to a well-documented finding on echocardiographic assessment of coarctation of the aorta, known as diastolic tailing [168, 169]. A threshold for this new screening tool was chosen to have a lower false-positive rate. Our results suggested that this detection algorithm improved the sensitivity of screening from 40 to 60% which was a significant improvement from the standard of care.

Our study was limited by the fact that signal acquisition for upper and lower extremities did not occur simultaneously, as was done in the studies of neonates with COA [118] and premature neonates with PDAs [170] with a custom-built photodetector for PPG analysis. Simultaneous acquisition reduces error in the analysis as the clinical situation of a critically

ill neonate fluctuates, especially in terms of HR and blood pressure. However, we attempted to eliminate these confounders in the data by normalizing for HR and minimizing timing changes between acquisition from the upper and lower extremities.

CHAPTER 9

APPLICATION OF A NOVEL ALGORITHM FOR MORPHOLOGICAL VARIABILITY OF ECG IN A VETERAN PTSD POPULATION

Previous studies reported PTSD was associated with heart disease and acute stress may trigger ventricular arrhythmias [11, 171]. Whether or not chronic PTSD is associated with an increased risk for ventricular tachyarrhythmias is not known, however. To investigate this further, we examined the relationship between PTSD and ventricular repolarization abnormalities. The current study trained an end-to-end deep convolutional neural network (DCNN) on ECG waveform data, obtained from the PhysioNet Challenge 2021 ECG database [20, 172, 173] to classify PTSD. The PhysioNet Challenge data consists of over 70,000 ECGs labeled for 25 different cardiac rhythms including normal sinus rhythm and cardiac arrhythmias. Improvement in the classification of PTSD status by pretraining on the arrhythmia data set would demonstrate the strength of the association of myocardial electrical disturbances with PTSD. The classification performance through deep learning was compared to a baseline approach using logistic regression trained on features extracted from significant TWA detection.

9.1 Data

Two data sets were used to train the DCNN. Figure 9.1 summarizes the training of the DCNN. Each of the 2 data sets are explained in the following sections.

9.1.1 PhysioNet/Computing in Cardiology (CinC) Challenge 2021

The first data set used to pretrain the DCNN was the twelve-lead ECG data part of the PhysioNet/CinC Challenge 2021 ECG database [172]. The data set consists of over 70,000 twelve-lead ECGs collected from 6 different hospitals across 3 continents. The recordings

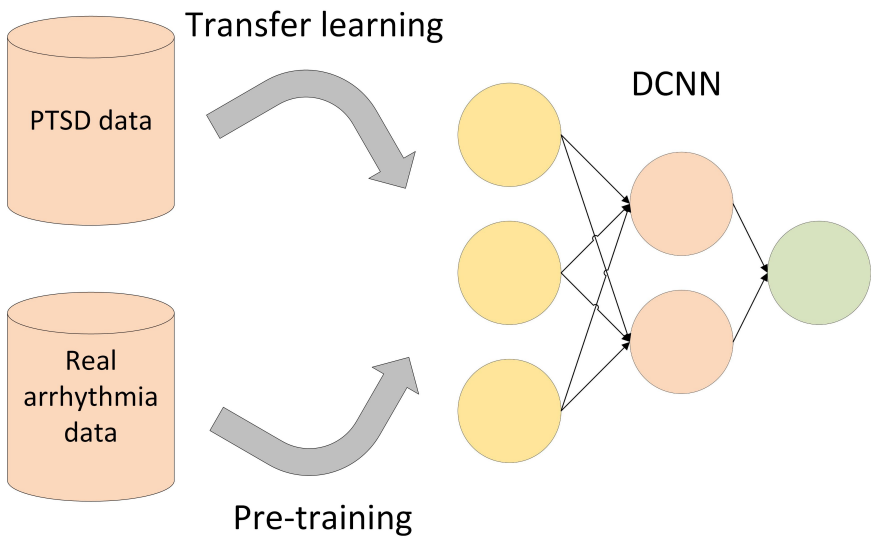

Figure 9.1: The real arrhythmia data and PTSD-related veteran ECG data were used to train a deep convolutional neural network for PTSD classification.

exhibit one or more of twenty-five different labeled arrhythmias, including atrial arrhythmias, ventricular arrhythmias and normal sinus rhythm. The PhysioNet/CinC Challenge 2021 ECG data was referred to as the real *arrhythmia data*. To test whether PTSD was associated with arrhythmogenesis, we pretrain a DCNN on the arrhythmia data before performing transfer learning on a smaller target data set of veterans with or without PTSD, discussed in further in section 9.1.2. Through transfer learning on the veteran data, the DCNN pretrained on the arrhythmia data will discover the relationship between the arrhythmia data and the PTSD label.

9.1.2 Veteran data and preprocessing

The veteran ECG data from the individuals with or without PTSD consisted of 12 individuals with PTSD and 24 controls. The data were recorded at 1000 Hz, consistent with previous algorithms that used deep neural networks trained on ECG data to detect cardiac arrhythmias [174]. The data consisted of single-channel Lead I ECG and the amplitude resolution of the data was measured to be 1.32×10^{-6} mV. Hence the data was high resolution both in the temporal and spatial domains. The veteran ECG data will be referred to as

the veteran data.

Each subject's recording in the veteran data set was segmented into 16-second windows with 20% overlap. Fifty 16-second windows with a SQI of 1 were randomly selected for each individual. The signal quality index by Li *et al.* was used to identify clean ECG analysis windows that were minimally affected by noise [21, 126]. The details of the algorithm are discussed in section 4.3.1. Baseline wander was removed using the 2 stage median filter by De Chazal *et al.* [129].

9.2 Deep convolutional neural network architecture and training

9.2.1 Network architecture

The DCNN used was the one developed by Zhao *et al.* [175]. The network was selected as overall it was the second-best algorithm at the PhysioNet challenge in 2020, and unlike the winning entry, did not require any additional hand-crafted features, particularly ones unrelated to PTSD. The architecture is given in figure 9.2a.

The following models were trained to classify the ECG recordings from the veteran twins using the data sets described in section 9.1.

- **Baseline:** A logistic regression model trained on hand-crafted features was used as the baseline against which transfer/deep learning approaches were compared. A logistic regression classifier was trained on features extracted from TWAs measured using the MMA method. To reject noise-triggered TWA, a surrogate statistical test [52], provided as part of the open source PhysioNet Cardiovascular Signal Processing Toolbox [3] was used. The TWAs were measured in 60 beat windows with 50% overlap. TWAs were considered statistically significant compared to the noise threshold from the surrogate test with a p value ≤ 0.05. The significant TWA detections were divided by HR decile into the following bins: [30,60), [60,70), [70,80), [80,90), [90,100) and [100,110]. For each individual, the mean significant TWA amplitude

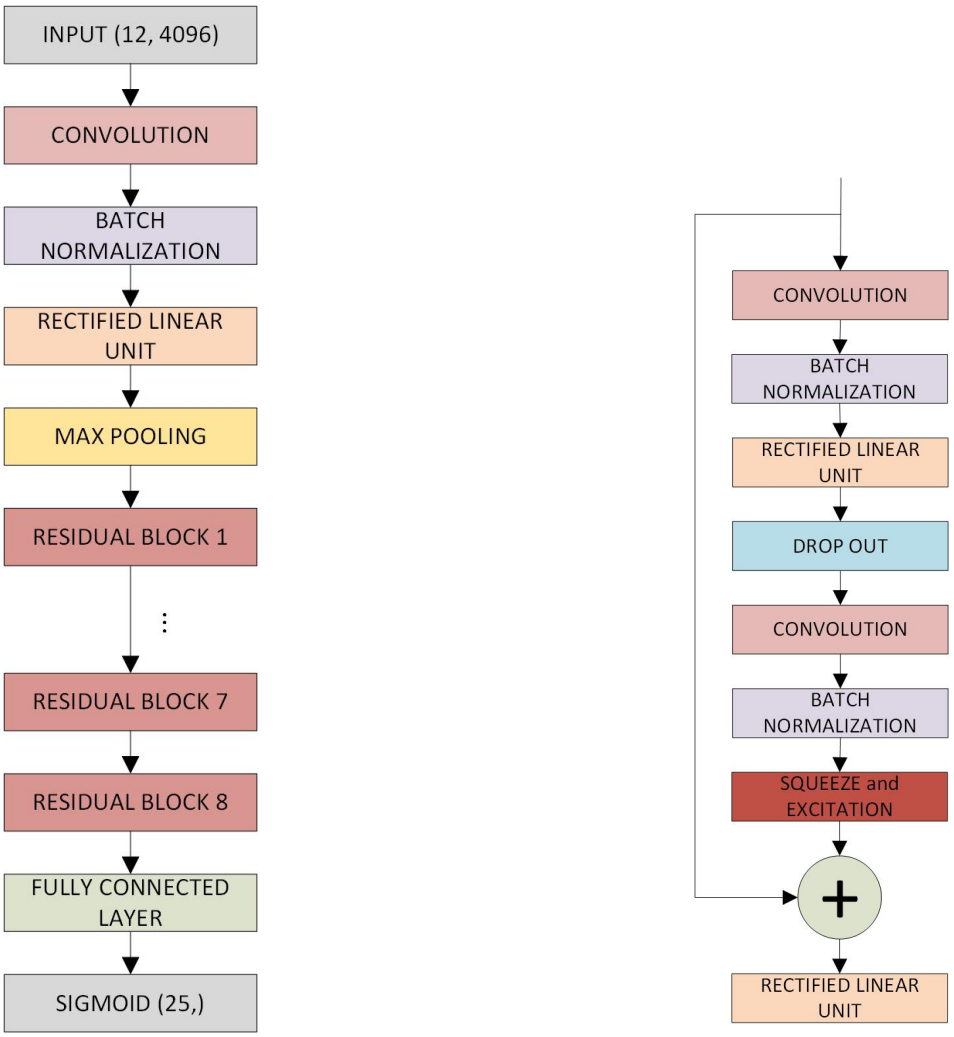

Figure 9.2: (a) ResNet model pre-trained on the real arrhythmia data and used for classifying the PTSD data. (b) Residual block architecture.

was computed in each bin and used as a feature vector. The AUROC was computed for leave one (subject) out testing, i.e., one subject was held out for testing while the features from the remaining subjects were used for training the logistic regression classifier. The process of training and testing the classifier was repeated so each subject was considered as the test subject. **Only the target veteran data was used for training the logistic regression classifier.**

- **Model 1:** The weights of the ResNet model based on Zhao's approach were randomly initialized and only the 7^{th}, 8^{th} residual block (ResB) and the fully connected (FC) layer weights were trained using the veteran data. Training the 7^{th}, 8^{th} ResB and the FC layer allowed direct comparison with model 2 to determine if pre-training of the layers before the 7^{th} ResB with the real arrhythmia data improved classification performance on the target veteran data. **No real arrhythmia data was used in the pre-training, only the target veteran data.**

- **Model 2:** The weights of the ResNet model were randomly initialized before pre-training on the real arrhythmia data. Next transfer learning was performed by training the 7^{th} ResB, 8^{th} ResB and the FC layer using the veteran data only. **The real arrhythmia data and veteran data were used for pre-training and training respectively.**

Figure 9.3 illustrates the data sets used for training each DCNN model. The network layers enclosed in blue were trained on the real arrhythmia data and the network layers enclosed in yellow were trained on the veteran data. Evaluating the performance of model 1 would determine if pre-training on the real arrhythmia data was important for accurate PTSD classification.

9.2.2 Network training

The ECG data were resampled to 257 Hz using an anti-alias filter before training and testing the ResNet classifier to be consistent with the lowest sampling rate of the data sets used in this study and previous work [176]. The ResNet architecture was trained for 50 epochs with an ADAM optimizer. The learning rate was initially set to 0.003 and was reduced by a factor of 0.1 after the 20th and 40th epoch. The batch size was kept at 64. After pre-training on the real arrhythmia data, the final sigmoid function layer was replaced to have 2 outputs. When classifying the veteran data all input leads except lead I were reduced to zero. To account for the class imbalance when training on the veteran data, 25 of the available 50 windows for each control subject not tested, were used to constitute the training data.

9.3 Evaluation methodology: Leave one out testing

Given the limited number of individuals in the veteran data set, the performance was evaluated on unseen data with the following leave-one-out-testing (LOOT) approach. One subject was held out as the test subject and not used for training or validation. The remaining subjects were used for training and validation. Ten percent of each subject's data in the training set was used for validation. 8 twin pairs were identified in the veteran data set. To prevent information leakage due common biology, each of the twin pairs in the veteran data set were included either in the training or testing set. The classifier was trained until the lowest measured validation loss was not observed to decrease for 2 consecutive epochs. Early stopping was used to train the network to prevent it from overfitting to particular trends in the ECGs for the individuals forming the training and validation data. The classifier with the lowest error on the validation data was used for classifying the test subject. The procedure was repeated to test each subject and the fraction of windows for each subject classified as PTSD was used to compute the AUROC. The accuracy (Acc), balanced accuracy (BAcc) and F1-score (F1) for the optimal operating point on the ROC curve were

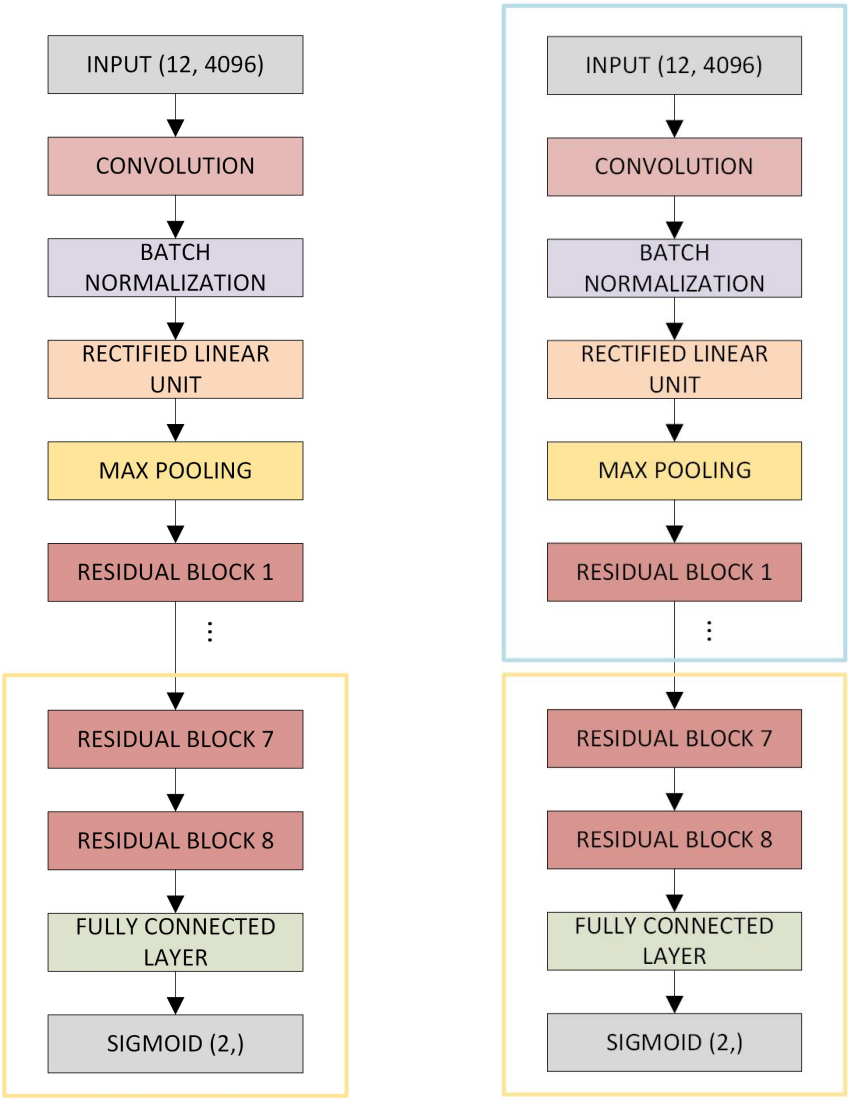

(a) ResNet model 1

(b) Resnet model 2

Figure 9.3: How each deep convolutional neural network model was trained is illustrated. The layers of the network trained on the real arrhythmia data are enclosed in blue. The layers of the network trained on the veteran data are enclosed in yellow.

computed for each model. Due to class imbalance in the veteran data the balanced accuracy was computed as the un-weighted average of sensitivity and specificity. The optimal operating point was computed as follows, a line with a slope of 1 started at the top left corner of the plot and was lowered until it intersected the ROC curve, the point at which the line first intersected was considered the optimal operating point. Defining the slope to be 1 resulted in the equal importance of the sensitivity and specificity, so the determination of the optimal point on the ROC curve was not affected by the imbalance in classes.

9.4 Results

The classification performance for each model described in section 9.2 is summarized in table 9.1. The highest score for each reported metric is in bold. Model 2 provided the best performance results in terms of AUROC, Acc, F1 and BAcc. Performing transfer learning on the network pre-trained on the arrhythmia data resulted in an improvement of 24% in the AUROC, 11% improvement in Acc, 23% improvement in F1 and 16% improvement in BAcc for PTSD classification compared to model 1. The ROC curves for LOOT with the veteran data for each model is plotted in figure 9.4. Classification performance achieved through training and testing model 2 proved accurate PTSD classification from ECG data could be achieved using this approach.

Table 9.1: The AUROC, Acc, F1 and BAcc for LOOT of models BL, 1 and 2 given in section 9.2. Arrhythmia and Veteran refer to the real arrhythmia data and veteran data respectively. Highest performances are bolded.

Model #	Arrhythmia	Veteran	AUROC	Acc	F1	BAcc
BL	No	Yes	0.56	0.67	0.57	0.67
1	No	Yes	0.61	0.75	0.57	0.69
2	Yes	Yes	**0.85**	**0.86**	**0.80**	**0.85**

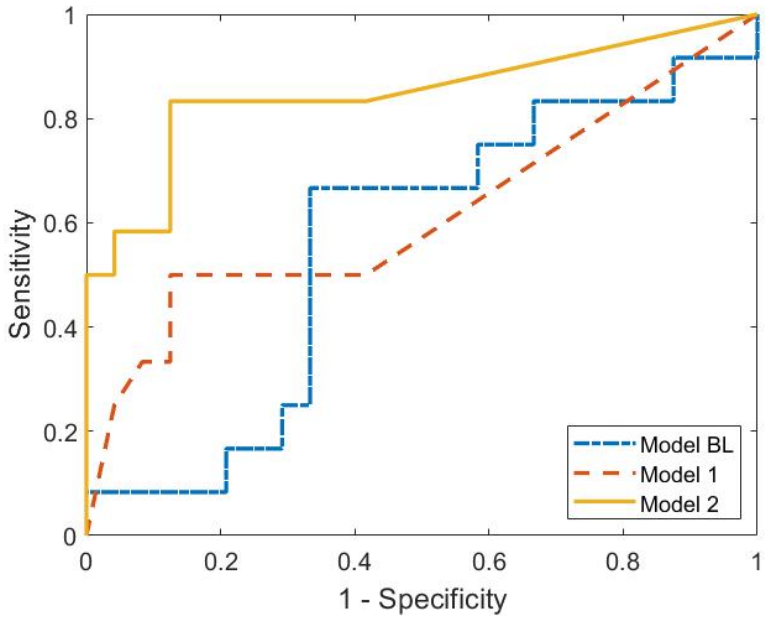

Figure 9.4: The ROC curve for models BL,1,2 for LOOT classification of the veteran data.

9.5 Discussion

The results in table 9.1 clearly indicate that pre-training on a large database of ECGs (over 70,000) with varying arrhythmias and other clinical abnormalities (model 2), provides a significant boost in performance over both standard and DNN-based baseline approaches (model BL and model 1) for the chosen classification problem. As a result of pre-training on the real arrhythmia data, the AUROC rose from 0.61 to 0.85, and an overall increase in all metrics, i.e. AUROC, F1, Acc and BAcc, was observed compared to baseline model 1. Deep learning models have been shown to approach or even improve upon human performance for disease detection [13, 107]. The accurate classification results for model 2 indicate a deep learning model can be accurately trained to automatically classify current PTSD status. The results for a boost in classification achieved are consistent with the literature, where arrhythmias have been shown to be important markers of PTSD [10]. The result of boosting classification through transfer learning is significant for the following reasons. Deep learning is a data-hungry approach. However, in many scenarios, particu-

larly in healthcare, large data sets of a particular disease, e.g. ECG data set of veteran twins with PTSD, can be difficult to obtain because of high costs, legal barriers, social resistance and difficulty accessing populations in remote areas. Additionally, some diseases can be very rare and acquiring an extensive database would be impractical. Transfer learning based-approaches enable training a deep neural network to accurately classify the disease state even on a small data set.

CHAPTER 10
CONCLUSION AND FUTURE WORK

10.1 Conclusion

The overall aim of this dissertation is to demonstrate the utility of measuring variability in the beat-to-beat morphology of physiologic signals (sampled at 100 Hz or more) for improving the performance of disease state detection. Secondly, this work aims to provide a standardized framework for computing morphological variability in physiologic signals that identify and account for the confounding effects from non-physiological sources, both exogenous (e.g. recording noise) and endogenous (e.g., HR and BR). Finally, the work presented aimed to explore non-parametric identification of morphological variability through the use of deep neural networks.

The dissertation developed a framework for a class of algorithms that measured MV in physiologic waveform signals and demonstrated the utility of these algorithms on 3 separate medical problems using waveform recordings from 3 different signal modalities, i.e., ECG, ABP and PPG. For each medical problem measuring variability from waveform data improved results compared to current practices that measured variation in time series data, e.g. RR intervals, SBP/MAP or oxygen saturation values. Methods for identifying and handling non-physiological confounding factors, e.g. additive external noise, were presented. HR and BR combinations that confounded measurements of MV from waveform signals were identified and mitigation strategies were implemented. Previous studies had not accounted for these factors. Therefore an important gap in previous studies was highlighted. Finally, a novel deep learning approach was developed for disease detection by reading an ECG waveform signal as input. The deep learning approach was applied for PTSD detection and accurately detected PTSD despite the small data set analyzed.

In the first part of the thesis we conducted an experimental study of synthesized ECG data comparing MVM and TWA measured at varying HRs, BRs, and SNRs. We found a strong confounding influence at high BRs and low HRs that likely inflated the conventionally measured results. In real data tests in normal individuals, in which little variability due to cardiovascular disease (CVD) was expected, 67% and 8% of the ECG signal showed elevations in MVM and TWA respectively, due to these effects. These results suggested misclassification due to non-cardiac effects, especially for MVM. Furthermore, adjusting for the confounding effects from physiological and non-physiological sources improved classification results for PTSD status in an analysis cohort. Future algorithms need to consider these effects as independent variables when attempting to accurately measure TWA and MVM in the context of CVD or other conditions, rather than the indirect influence of BR, HR, and SNR on MV.

In the second part, MV features evaluated from ECG were added to HRV features measured from RR intervals and improved classification as current PTSD and past PTSD or controls. A greater improvement of 10% in classification AUROC was observed for current or past PTSD as compared to 5% for current PTSD or controls. HRV parameters more strongly distinguished between current PTSD and control individuals as compared to current and past PTSD individuals. The classification results indicated that computational biomarkers can assist in identifying active PTSD in a subject, providing an objective alternate to the CAPS-5. In addition, MV of ABP was shown to drop in septic patients before sepsis onset and was predictive of sepsis onset. Hypotension, which measured drops in SBP and MAP time series data, was commonly associated with sepsis onset. However, results suggested hypotension was independently not predictive of sepsis onset.

In the third part, specific differences in waveform characteristics were identified between PPG signals measured at upper and lower extremities in neonates with COA, using beat-to-beat analysis of upper and lower extremities in the same neonate. This provided a valuable clinical application for data analytics in healthcare by comparing waveform mor-

phology to improve the sensitivity of COA diagnosis compared to the current clinical practice of identifying discrepancies in oxygen saturation values between the upper and lower extremity. This potentially life-saving screening method to identify neonates with COA early enough will eventually be implemented to prevent cardiogenic shock commonly associated with COA.

In the final part of the thesis, classification results improved when the ResNet DCNN model was pre-trained on the cardiac arrhythmia data before transfer learning was applied to classify the target veteran PTSD data. The transfer learning-based approach for boosting classification employed in this study, by pretraining on a large data set characteristic of a smaller target data set has broad applicability for deep learning tasks in medicine and biology.

The paradigm of transfer-learning based boosting proposed in this work is likely to be generalizable to different pathologies and signal modalities. Furthermore, the analysis results demonstrated accurate PTSD classification was achievable through a deep learning approach and encouraged further investigation of PTSD status classification on a more extensive data set.

Evaluating computational biomarkers that measure MV from waveform signals improved disease detection and prediction compared to using features extracted from time-series data. Incorporating these computational biomarkers improves automated tracking of a patient's health status, reduces the fatigue on health care workers, improving their efficiency and alerting them when required. Using quantitative physiological signals from individuals or the computational biomarkers evaluated from these signals can improve the standardization of clinician-administered screening tests, e.g. PCL-5, that are highly subjective.

10.2 Future work

There are several promising areas into which the research can be extended, including:

1. The MV analysis of subjects with or without PTSD can be conducted on an extended data set with more subjects. Training a classifier to learn the decision boundary to account for the effects of HR and BR when classifying PTSD on a larger data set will lead to a more accurate estimate of the decision boundary, resulting in further improvement of PTSD status classification.

2. MV in ABP was shown to be independently predictive of sepsis onset. Additional features, e.g. HR, BR, oxygen saturation and white blood cell count, known to be predictive of sepsis onset, can be added to MV in ABP to determine if this improves the prediction of sepsis onset.

3. The utility of PPG waveform data analysis was demonstrated for detecting COA. The next step can include using the algorithm to detect COA in a larger cohort of unscreened neonates. Two PPG signal measurement devices could be set up, enabling simultaneous data acquisition from the upper and lower extremities of the neonates. Simultaneous acquisition of data is expected to improve the classification results further.

4. The ResNet model was trained in one specific domain using a small data set of 36 subjects with or without PTSD. PTSD classification using deep learning was encouraging and warranted further investigation on a larger data set. Speech signals and video, shown to be strongly predictive of PTSD [101, 102], can be added to ECG signals to obtain an expected improvement for the PTSD classification performance.

Appendices

APPENDIX A

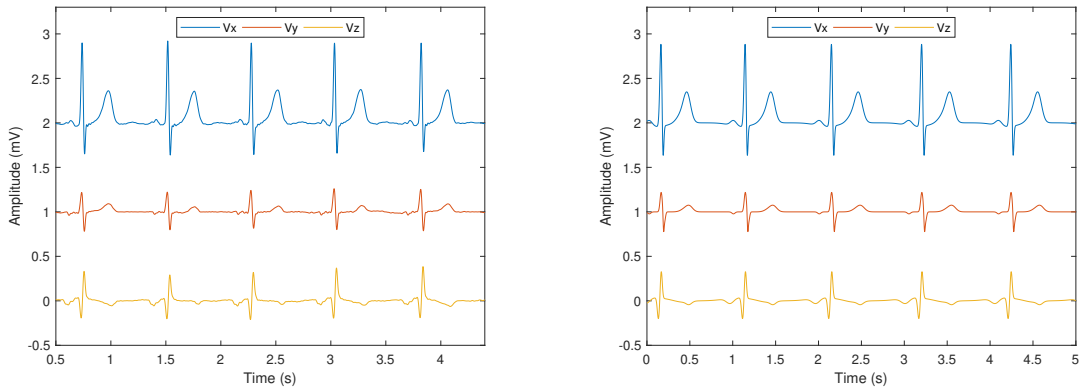

(a) (b)

Figure A.1: (A) A five-beat window of the original VCG for recording s0303lre from patient 105 in the PTBDB. (B) The same VCG approximated using Gaussians.

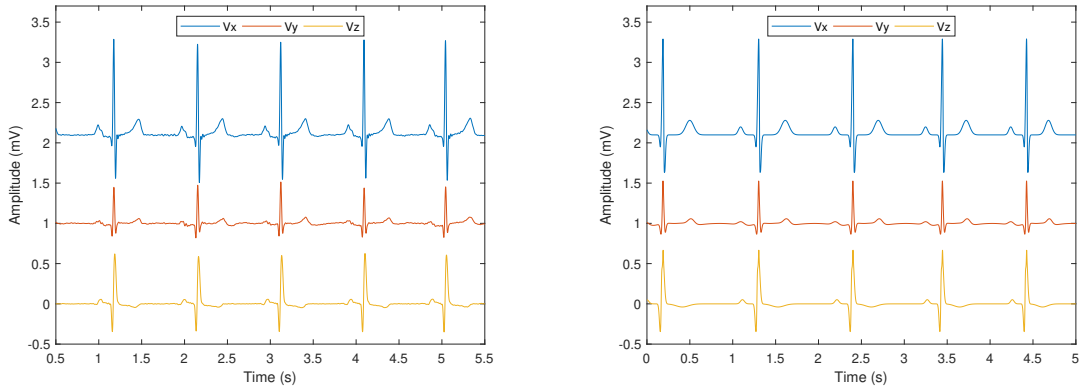

(a) (b)

Figure A.2: (A) A five-beat window of the original VCG for recording s0302lre from patient 116 in the PTBDB. (B) The same VCG approximated using Gaussians.

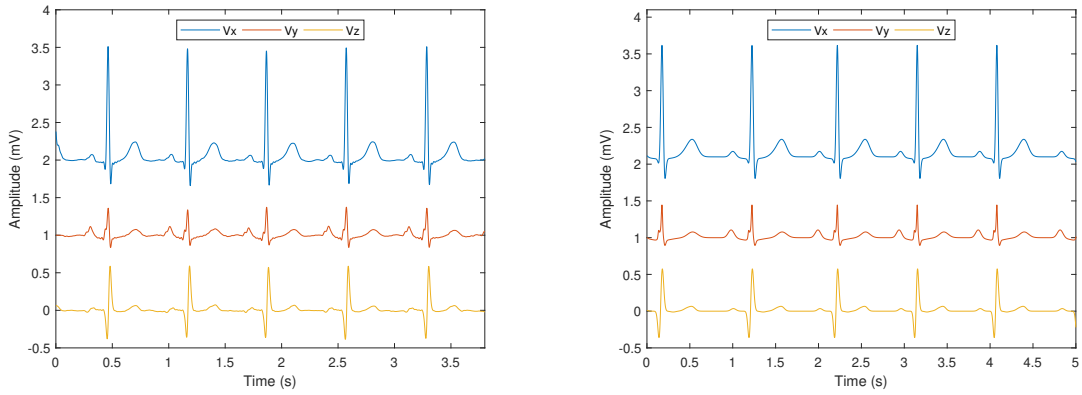

(a) (b)

Figure A.3: (A) A five-beat window of the original VCG for recording s0311lre from patient 121 in the PTBDB. (B) The same VCG approximated using Gaussians.

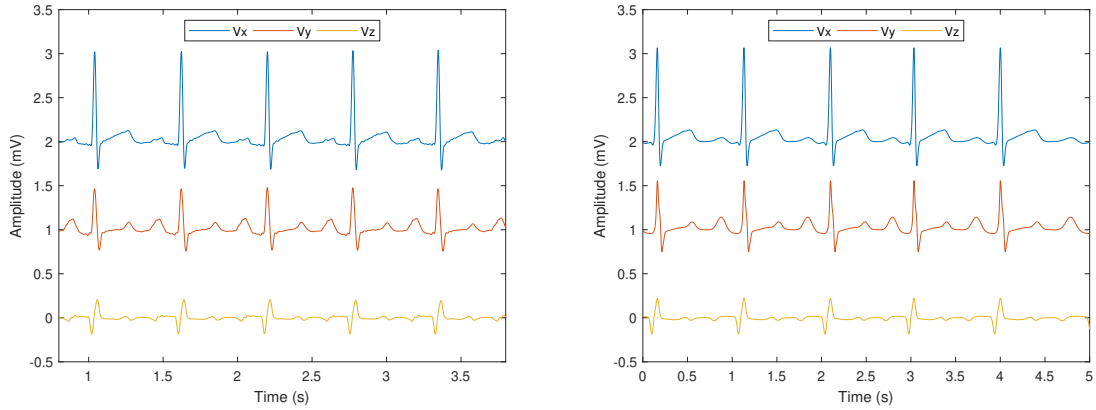

(a) (b)

Figure A.4: (A) A five-beat window of the original VCG for recording s0273lre from patient 131 in the PTBDB. (B) The same VCG approximated using Gaussians.

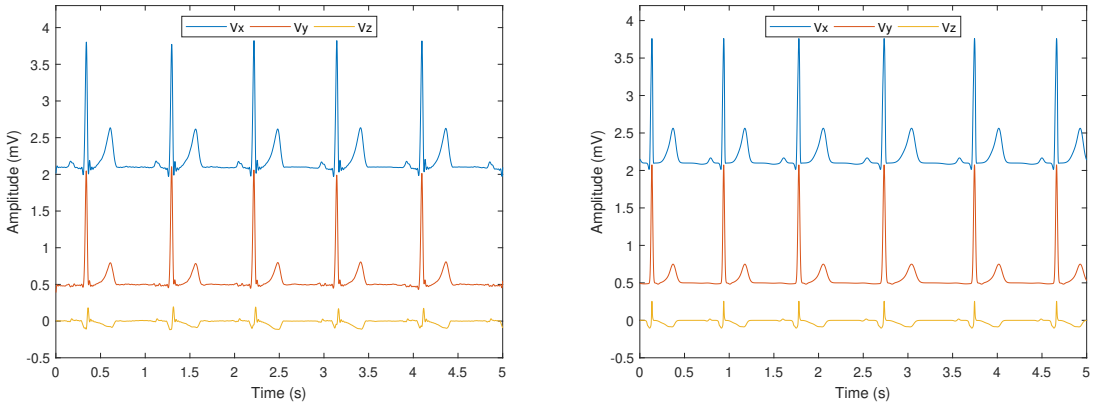

(a) (b)

Figure A.5: (A) A five-beat window of the original VCG for recording s0287lre from patient 150 in the PTBDB. (B) The same VCG approximated using Gaussians.

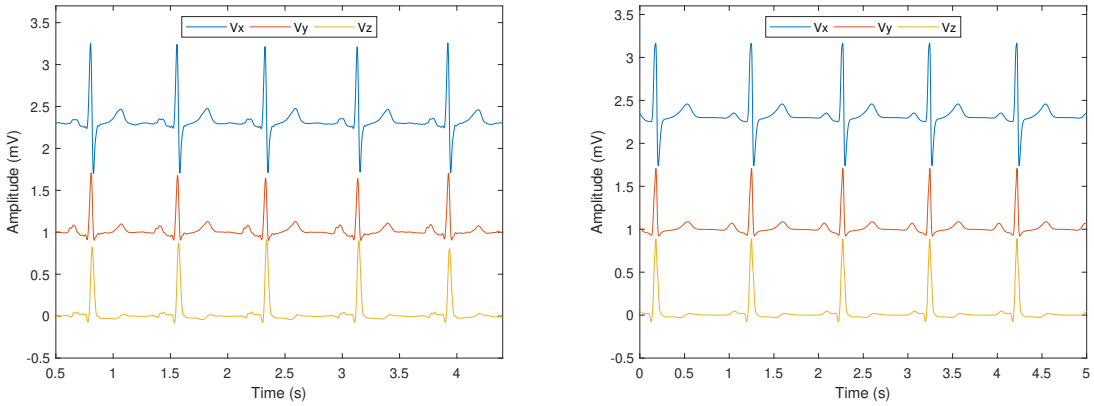

(a) (b)

Figure A.6: (A) A five-beat window of the original VCG for recording s0301lre from patient 155 in the PTBDB. (B) The same VCG approximated using Gaussians.

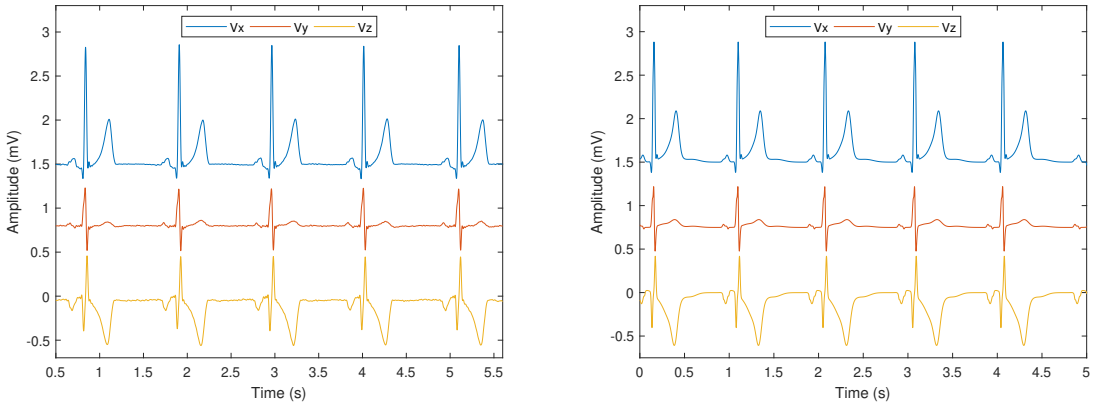

(a) (b)

Figure A.7: (A) A five-beat window of the original VCG for recording s0323lre from patient 165 in the PTBDB. (B) The same VCG approximated using Gaussians.

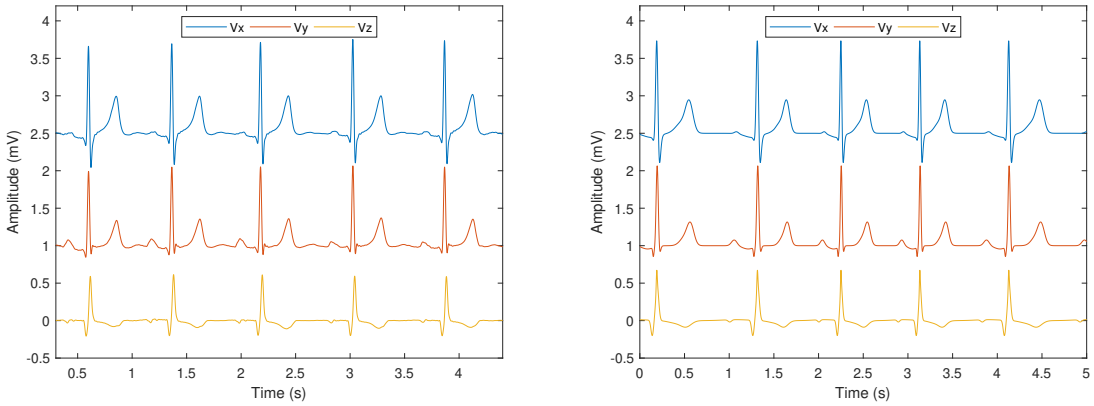

(a) (b)

Figure A.8: (A) A five-beat window of the original VCG for recording s0300lre from patient 174 in the PTBDB. (B) The same VCG approximated using Gaussians.

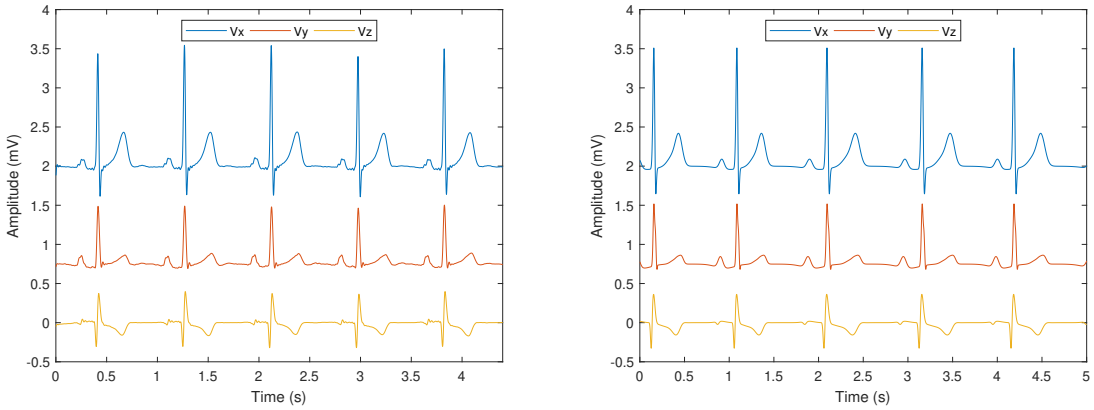

(a) (b)

Figure A.9: (A) A five-beat window of the original VCG recording for s0308lre from patient 182 in the PTBDB. (B) The same VCG approximated using Gaussians.

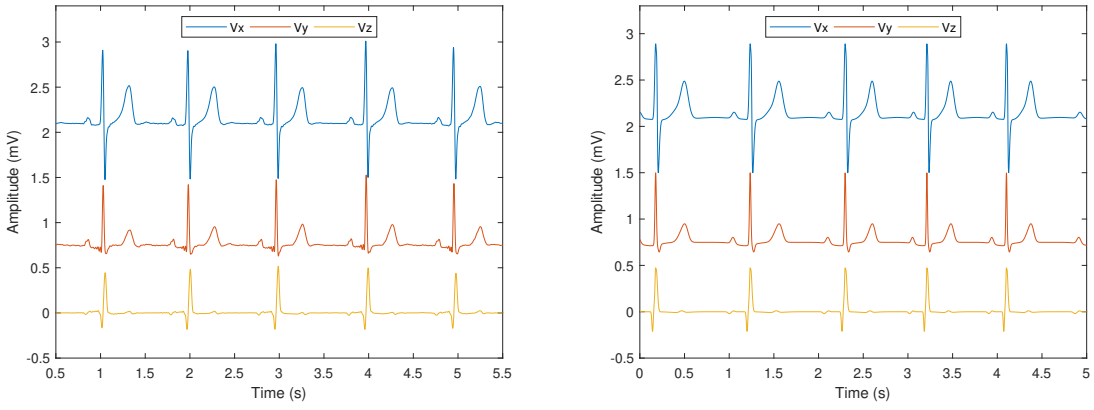

(a) (b)

Figure A.10: (A) A five-beat window of the original VCG for recording s0336lre from patient 185 in the PTBDB. (B) The same VCG approximated using Gaussians.

Table A.1: The Gaussian parameters used for generating the artificial VCGs 1 through 5 are listed.

Record #	Index (i)	1	2	3	4	5	6	7	8	9	10
patient105/s0303lre	α_i^x	-0.04	0.06	0.98	-0.60	0.10	0.29				
	b_i^x	0.78	0.23	0.09	-0.06	0.37	0.26				
	θ_i^x	-0.32	-0.88	0.001	0.13	1.55	1.95				
	α_i^y	0.22	-0.16	-0.11	-0.02	0.04	0.05				
	b_i^y	0.08	0.04	-0.07	0.11	-0.31	0.25				
	θ_i^y	0.005	0.18	0.25	-0.88	1.81	2.13				
	α_i^z	0.31	-0.24	0.04	-0.06	-0.02	-0.03				
	b_i^z	0.07	0.08	0.95	0.28	0.51	0.21				
	θ_i^z	0.01	-0.20	-0.56	-1.13	1.58	2.08				
patient116/s0302lre	α_i^x	2.50	1.38	-0.32	0.18	0.10	-1.83				
	b_i^x	0.05	0.05	0.02	0.26	0.15	0.09				
	θ_i^x	0.01	-0.07	0.07	1.76	-1.19	-0.01				
	α_i^y	-0.19	0.22	0.16	0.10	0.04	0.07	2.22	-1.90		
	b_i^y	0.93	0.03	0.61	0.54	0.20	0.21	0.08	0.09		
	θ_i^y	0.57	-0.01	0.26	1.25	-1.16	1.85	0.01	0.01		
	α_i^z	0.57	-0.44	0.05	-0.04	0.28	0.12				
	b_i^z	0.09	0.07	0.13	0.41	0.03	0.02				
	θ_i^z	-0.004	-0.16	-1.07	1.27	-0.09	0.005				
patient121/s0311lre	α_i^x	3.94	-0.03	-2.43	0.15	0.12	0.08				
	b_i^x	0.10	-0.73	0.12	0.31	0.40	0.20				
	θ_i^x	0.00	-0.05	0.02	2.19	1.85	-1.34				
	α_i^y	0.20	0.08	0.23	-0.04	0.11	0.08	0.17	0.17	-0.23	
	b_i^y	0.03	0.04	0.04	-0.67	0.21	0.35	0.07	0.14	0.10	
	θ_i^y	0.01	-0.24	-0.03	-0.07	-1.46	2.13	0.08	-0.03	0.10	
	α_i^z	1.07	-1.00	-0.01	0.05	0.04	0.04				
	b_i^z	0.12	0.11	0.18	0.28	0.18	0.18				
	θ_i^z	-0.05	-0.14	0.77	1.83	2.15	-1.30				
patient131/s0273lre	α_i^x	1.46	-0.05	-0.62	0.08	0.21	0.06	-0.12	-0.04		
	b_i^x	0.10	-0.32	-0.12	0.54	0.30	0.46	0.22	0.07		
	θ_i^x	0.01	-1.00	0.11	1.51	2.23	-1.43	2.17	-0.32		
	α_i^y	0.35	-0.04	-0.14	0.03	0.07	0.16	-0.23	0.28		
	b_i^y	0.05	0.85	0.08	0.62	0.22	0.30	0.05	0.15		
	θ_i^y	-0.01	-0.42	0.40	1.88	2.53	-1.65	0.30	0.07		
	α_i^z	-0.19	0.22	-0.02	0.03	0.02	0.02	-0.04	-0.03		
	b_i^z	0.10	0.11	-0.64	0.05	0.66	0.19	0.19	0.19		
	θ_i^z	-0.40	-0.003	1.20	-0.22	-1.34	2.05	-2.16	2.42		
patient150/s0287lre	α_i^x	1.14	1.14	0.20	0.64	0.33	-0.02	0.07	-0.20		
	b_i^x	0.04	0.06	-0.34	0.03	0.20	0.35	0.14	-0.11		
	θ_i^x	0.003	-0.08	1.58	0.05	1.89	-1.91	-1.15	-0.13		
	α_i^y	1.58	0.02	-0.02	0.23	0.06	-0.02				
	b_i^y	0.07	-0.37	0.10	0.24	-0.30	-0.64				
	θ_i^y	-0.004	-1.31	0.54	1.87	1.44	-1.08				
	α_i^z	0.04	-0.10	0.27	-0.08	-0.03	-0.01	0.02	-0.02	-0.05	
	b_i^z	-0.04	0.14	0.03	-0.28	-0.24	0.10	0.08	-0.04	0.15	
	θ_i^z	0.05	-0.20	-0.003	1.49	0.89	-1.48	-1.21	-0.38	1.86	

Table A.2: The Gaussian parameters used for generating the artificial VCGs 6 through 10 are listed.

Record #	Index (i)	1	2	3	4	5	6	7	8	9	10	11
patient155/s0301lre	α_i^x	1.11	-0.62	0.06	0.12	0.38	0.38	0.08	-0.05			
	b_i^x	0.08	-0.14	0.36	0.25	0.04	0.04	0.22	0.72			
	θ_i^x	-0.06	0.09	1.73	2.10	0.03	0.03	-1.14	-0.39			
	α_i^y	0.77	0.44	-0.04	0.02	0.09	0.10	-0.10				
	b_i^y	0.06	0.06	0.91	0.21	0.24	0.22	0.20				
	θ_i^y	0.01	-0.11	-0.50	1.67	2.10	-1.28	-0.02				
	α_i^z	0.46	0.27	-0.07	-0.05	-0.08	0.04	0.53	0.07	0.18	-0.11	
	b_i^z	0.06	0.05	0.28	0.21	0.33	0.17	0.05	-0.89	0.10	0.06	
	θ_i^z	-0.09	0.12	0.60	1.72	1.22	-1.13	0.005	0.85	0.05	-0.31	
patient165/s0323lre	α_i^x	0.03	0.08	-0.13	0.85	1.11	0.75	0.06	0.10	0.17	0.39	0.03
	b_i^x	0.09	0.11	0.05	0.04	0.03	0.03	0.04	0.60	0.30	0.18	0.50
	θ_i^x	-1.09	-0.83	-0.19	-0.07	0.00	0.06	0.22	1.20	1.42	1.68	2.90
	α_i^y	0.04	0.02	-0.02	0.32	0.51	-0.32	0.04	0.08	0.01		
	b_i^y	0.07	0.07	0.04	0.06	0.04	0.06	0.45	0.30	0.50		
	θ_i^y	-1.10	-0.90	-0.76	-0.11	-0.01	0.07	0.80	1.58	2.90		
	α_i^z	-0.03	-0.14	-0.04	0.05	-0.40	0.46	-0.12	-0.20	-0.35	-0.04	
	b_i^z	0.03	0.12	0.04	0.40	0.05	0.05	0.80	0.40	0.20	0.40	
	θ_i^z	-1.10	-0.93	-0.70	-0.40	-0.15	0.10	1.05	1.25	1.55	2.80	
patient174/s0300lre	α_i^x	0.03	-0.05	2.07	-0.87	0.38	0.14					
	b_i^x	0.13	0.48	0.08	0.12	0.23	0.38					
	θ_i^x	-1.30	-0.33	0.01	0.06	2.03	1.57					
	α_i^y	-0.10	1.95	-0.88	0.12	0.25	0.08	-0.04				
	b_i^y	0.04	0.08	0.10	0.31	0.21	0.17	0.35				
	θ_i^y	-0.22	0.03	0.04	1.78	2.12	-1.44	-0.57				
	α_i^z	-0.21	0.46	0.23	-0.03	-0.07	-0.03	0.01				
	b_i^z	0.08	0.10	0.03	0.46	0.32	0.11	0.79				
	θ_i^z	-0.28	0.03	0.001	1.21	1.84	-1.72	-1.35				
patient182/s0308lre	α_i^x	-0.04	1.97	-1.18	0.35	0.14	0.12					
	b_i^x	0.85	0.08	0.06	0.25	0.39	0.18					
	θ_i^x	-0.56	0.03	0.11	1.90	1.45	-1.14					
	α_i^y	-0.05	0.79	0.04	0.08	0.07	0.14	-0.06	0.33			
	b_i^y	0.71	0.06	0.26	0.20	0.14	0.18	-0.03	0.04			
	θ_i^y	-0.89	0.01	1.50	1.87	2.12	-1.24	0.23	0.13			
	α_i^z	-0.45	0.38	0.04	-0.05	-0.14	0.02	-0.04				
	b_i^z	0.06	0.11	0.21	0.55	0.31	0.36	0.10				
	θ_i^z	-0.19	-0.03	2.12	1.06	1.73	-1.21	-1.45				
patient185/s0336lre	α_i^x	0.53	1.20	-0.77	0.12	0.35	0.07	-0.03				
	b_i^x	0.03	0.07	0.10	0.39	0.23	0.14	-1.47				
	θ_i^x	0.08	0.01	0.11	1.49	1.93	-1.07	0.79				
	α_i^y	-0.04	0.78	-0.08	0.11	0.13	0.07					
	b_i^y	0.61	0.05	0.07	0.24	0.18	0.12					
	θ_i^y	-0.35	-0.004	0.23	1.73	1.99	-1.15					
	α_i^z	-0.22	0.46	-0.01	0.09	-0.02	0.02	0.01				
	b_i^z	0.04	0.08	-0.59	0.02	0.09	0.14	0.08				
	θ_i^z	-0.21	0.03	-10.99	-0.02	-1.39	1.72	-1.10				

REFERENCES

[1] K. Rishikesan, A. Oguz, H. M. A., A. N. West, R. L. Davis, and S. H. Shah, "Applying artificial intelligence to identify physiomarkers predicting severe sepsis in the PICU," *Pediatric Critical Care Medicine*, vol. 19, no. 10, e495–e503, Oct. 2018.

[2] S. P. Shashikumar *et al.*, "Early sepsis detection in critical care patients using multiscale blood pressure and heart rate dynamics," *Journal of Electrocardiology*, vol. 50, no. 6, pp. 739–743, 2017.

[3] A. N. Vest *et al.*, "An open source benchmarked toolbox for cardiovascular waveform and interval analysis," *Physiological Measurement*, vol. 39, no. 10, p. 105 004,

[4] E. Reinertsen *et al.*, "Heart rate-based window segmentation improves accuracy of classifying posttraumatic stress disorder using heart rate variability measures," *Physiological Measurement*, vol. 38, pp. 1061–1076, Jun. 2017.

[5] R. Kessler, P. Berglund, O. Demler, R. Jin, K. Merikangas, and E. Walters, "Lifetime prevalence and age-of-onset distributions of DSM-IV disorders in the national comorbidity survey replication," *Archives of General Psychiatry*, vol. 62, pp. 593–602, Jul. 2005.

[6] C. Erbes, J. Westermeyer, B. Engdahl, and E. Johnsen, "Post-traumatic stress disorder and service utilization in a sample of service members from Iraq and Afghanistan," *Military Medicine*, vol. 172, pp. 359–63, May 2007.

[7] B. Dohrenwend, B. Turner, N. Turse, B. Adams, K. Koenen, and R. Marshall, "The psychological risks of vietnam for U.S. veterans: A revisit with new data and methods," *Science (New York, N.Y.)*, vol. 313, pp. 979–82, Sep. 2006.

[8] R. Yehuda, "Post-traumatic stress disorder," *New England Journal of Medicine*, vol. 346, pp. 108–114, Feb. 2002.

[9] E. A. Dedert, P. S. Calhoun, L. L. Watkins, A. Sherwood, and J. C. Beckham, "Posttraumatic Stress Disorder, Cardiovascular, and Metabolic Disease: A Review of the Evidence," *Annals of Behavioral Medicine*, vol. 39, no. 1, pp. 61–78, Feb. 2010. eprint: https://academic.oup.com/abm/article-pdf/39/1/61/22057610/12160_2010_article_9165.pdf.

[10] V. Vaccarino *et al.*, "Post-traumatic stress disorder and incidence of coronary heart disease: A twin study," *Journal of the American College of Cardiology*, vol. 62, no. 11, pp. 970–978, 2013.

[11] R. Lampert, "ECG signatures of psychological stress," *Journal of Electrocardiology*, vol. 48, no. 6, pp. 1000–1005, 2015.

[12] R. Costin, C. Rotariu, and A. Pasarica, "Mental stress detection using heart rate variability and morphologic variability of ECG signals," in *2012 International Conference and Exposition on Electrical and Power Engineering*, 2012, pp. 591–596.

[13] A. Y. Hannun *et al.*, "Cardiologist-level arrhythmia detection and classification in ambulatory electrocardiograms using a deep neural network," *Nature Medicine*, vol. 25, no. 1, pp. 65–69, Jan. 2019.

[14] W. Zhou *et al.*, "Ensembled deep learning model outperforms human experts in diagnosing biliary atresia from sonographic gallbladder images," *Nature Communications*, vol. 12, no. 1, p. 1259, Feb. 2021.

[15] M. Singer *et al.*, "The third international consensus definitions for sepsis and septic shock (sepsis-3)," *JAMA*, vol. 315, no. 2, pp. 801–810, Feb. 2016.

[16] P. S. Rao, "Coarctation of the aorta," *Current Cardiology Reports*, vol. 7, no. 6, pp. 425–434, Nov. 2005.

[17] L. Itu *et al.*, "Non-invasive hemodynamic assessment of aortic coarctation: Validation with in vivo measurements," *Annals of Biomedical Engineering*, vol. 41, no. 4, pp. 669–681, Apr. 2013.

[18] H. Shin and S. D. Min, "Feasibility study for the non-invasive blood pressure estimation based on ppg morphology: Normotensive subject study," *BioMedical Engineering OnLine*, vol. 16, no. 1, 2017.

[19] J. P. Martinez and S. Olmos, "Methodological principles of T wave alternans analysis: A unified framework," *IEEE Transactions on Biomedical Engineering*, vol. 52, no. 4, pp. 599–613, Apr. 2005.

[20] A. Goldberger *et al.*, "Physiobank, Physiotoolkit, and Physionet : Components of a new research resource for complex physiologic signals," *Circulation*, vol. 101, E215–20, Jul. 2000.

[21] I. Sadiq, E. A. Perez-Alday, A. J. Shah, and G. D. Clifford, "Breathing rate and heart rate as confounding factors in measuring T wave alternans and morphological variability in ECG," *Physiological Measurement*, vol. 42, no. 1, p. 015 002, Jan. 2021.

[22] M. W. Sorensen, I. Sadiq, G. D. Clifford, K. O. Maher, and M. E. Oster, "Using pulse oximetry waveforms to detect coarctation of the aorta," *BioMedical Engineering OnLine*, May 2020.

[23] I. Sadiq, E. A. Perez-Alday, A. J. Shah, A. B. Rad, R. Sameni, and G. D. Clifford, *Mythological medical machine learning: Boosting the performance of a deep learning medical data classifier using realistic physiological models*, 2021. arXiv: 2112.15442 [cs.LG].

[24] *What is posttraumatic stress disorder?* https://www.psychiatry.org/patients-families/ptsd/what-is-ptsd, Accessed: 2019-05-19.

[25] A. J. Shah, R. Lampert, J. Goldberg, E. Veledar, J. D. Bremner, and V. Vaccarino, "Posttraumatic stress disorder and impaired autonomic modulation in male twins," *Biological Psychiatry*, vol. 73, no. 11, pp. 1103–1110, 2013.

[26] M. Baumert *et al.*, "QT interval variability in body surface ECG: Measurement, physiological basis, and clinical value: Position statement and consensus guidance endorsed by the european heart rhythm association jointly with the ESC working group on cardiac cellular electrophysiology," *Europace*, vol. 18, Jun. 2016.

[27] N. T. Srinivasan and R. J. Schilling, "Sudden cardiac death and arrhythmias," *Arrhythmia and Electrophysiology Review*, vol. 2, no. 7, pp. 111–117, 2018.

[28] C. Granger, R. Goldberg, and O. Dabbous, "Predictors of hospital mortality in the global registry of acute coronary events," *ACC Current Journal Review*, vol. 13, p. 13, Feb. 2004.

[29] E. Antman *et al.*, "The TIMI risk score for unstable angina/non-ST elevation MI: A method for prognostication and therapeutic decision making," *JAMA : The Journal of the American Medical Association*, vol. 284, pp. 835–42, Aug. 2000.

[30] Y. Liu, Z. Syed, B. M. Scirica, D. A. Morrow, J. V. Guttag, and C. M. Stultz, "ECG morphological variability in beat space for risk stratification after acute coronary syndrome," *Journal of the American Heart Association*, vol. 3, no. 3, e000981, 2014. eprint: https://www.ahajournals.org/doi/pdf/10.1161/JAHA.114.000981.

[31] A. C. Guyton and J. E. Hall, *Textbook of Medical Physiology*. 1600 John F. Kennedy Blvd. Ste 1800 Philadelphia, PA 19103-2899: W. B. Saunders Co., 12th edition, 2011, ISBN: 978-1-4160-4574-8.

[32] E. Frank, "An accurate, clinically practical system for spatial vectorcardiography," *Circulation*, vol. 13, no. 5, pp. 737–749, 1956. eprint: https://www.ahajournals.org/doi/pdf/10.1161/01.CIR.13.5.737.

[33] A. J. Goodwin, D. A. Rice, K. N. Simpson, and D. W. Ford, "Frequency, cost, and risk factors of readmissions among severe sepsis survivors," *Critical Care Medicine*, vol. 43, no. 4, pp. 738–746, Apr. 2015.

[34] J. Fong, *Invasive arterial pressure monitoring*, https://www.aic.cuhk.edu.hk/web8/art%20line.htm, Accessed: 2021-01-05, 2010.

[35] E. Rosenthal, "Coarctation of the aorta from fetus to adult: Curable condition or life long disease process?" *Heart*, vol. 91, no. 11, pp. 1495–1502, 2005. eprint: https://heart.bmj.com/content/91/11/1495.full.pdf.

[36] *Facts about coarctation of the aorta*, https://www.cdc.gov/ncbddd/heartdefects/coarctationofaorta.html, Accessed: 2019-04-30.

[37] R.-K. R. Chang, M. Gurvitz, and S. Rodriguez, "Missed diagnosis of critical congenital heart disease," *Archives of Pediatrics and Adolescent Medicine*, vol. 162, no. 10, pp. 969–974, 2008.

[38] P. Araoz, G. Reddy, H. Tarnoff, C. Roge, and C. Higgins, "MR findings of collateral circulation are more accurate measures of hemodynamic significance than arm-leg blood pressure gradient after repair of coarctation of the aorta," *Journal of Magnetic Resonance Imaging*, vol. 17, no. 2, pp. 177–183, Feb. 2003.

[39] J. F. Fernandes *et al.*, "Beyond pressure gradients: The effects of intervention on heart power in aortic coarctation," *PLOS ONE*, vol. 12, no. 1, pp. 1–14, Jan. 2017.

[40] S. F. Kaine, E. O. Smith, A. R. Mott, C. E. Mullins, and T. Geva, "Quantitative echocardiographic analysis of the aortic arch predicts outcome of balloon angioplasty of native coarctation of the aorta," *Circulation*, vol. 94, no. 5, pp. 1056–1062, 1996. eprint: https://www.ahajournals.org/doi/pdf/10.1161/01.CIR.94.5.1056.

[41] A. Mendelsohn, A. Banerjee, L. F. Donnelly, and D. C. Schwartz, "Is echocardiography or magnetic resonance imaging superior for precoarctation angioplasty evaluation?" *Catheterization and cardiovascular diagnosis*, vol. 42, pp. 26–30, Sep. 1997.

[42] A. V. J. Challoner and C. A. Ramsay, "A photoelectric plethysmograph for the measurement of cutaneous blood flow," *Physics in Medicine and Biology*, vol. 19, no. 3, pp. 317–328, May 1974.

[43] A. Murray and D. Marjanovic, "Optical assessment of recovery of tissue blood supply after removal of externally applied pressure," *Medical & Biological Engineering & Computing*, vol. 35, no. 4, pp. 425–427, Jul. 1997.

[44] D. P. Jones, "Medical electro-optics: Measurements in the human microcirculation," *Physics in Technology*, vol. 18, no. 2, pp. 79–85, Mar. 1987.

[45] J. Allen and A. Murray, "Variability of photoplethysmography peripheral pulse measurements at the ears, thumbs and toes," *IEE Proceedings - Science, Measurement and Technology*, vol. 147, 403–407(4), 6 Nov. 2000.

[46] L. M. Nilsson, "Respiration signals from photoplethysmography," *Anesthesia & Analgesia*, vol. 117, no. 4, 2013.

[47] K. Bartels and R. H. Thiele, "Advances in photoplethysmography: Beyond arterial oxygen saturation," *Canadian Journal of Anesthesia/Journal canadien d'anesthésie*, vol. 62, no. 12, pp. 1313–1328, Dec. 2015.

[48] U. Baber, A. S. Kini, S. K. Sharma, M. C. Kim, M. E. Farkouh, and P. Muntner, "Thrombolysis in myocardial infarction (TIMI) risk score and mortality in patients with advanced chronic kidney disease and on dialysis," *American Journal of Cardiology*, vol. 103, no. 11, pp. 1513–1517, Jun. 2009.

[49] B. E. Backus, A. J. Six, J. H. Kelder, W. B. Gibler, F. L. Moll, and P. A. Doevendans, "Risk scores for patients with chest pain: Evaluation in the emergency department," *Current Cardiology Reviews*, vol. 7, no. 1, pp. 2–8, 2011.

[50] S. M. Narayan, "T-wave alternans and the susceptibility to ventricular arrhythmias," *Journal of the American College of Cardiology*, vol. 47, no. 2, pp. 269–281, 2006.

[51] P. Brugada and J. Brugada, "Right bundle branch block, persistent ST segment elevation and sudden cardiac death: A distinct clinical and electrocardiographic syndrome," *Journal of the American College of Cardiology*, vol. 20, no. 6, pp. 1391–1396, 1992.

[52] S. Nemati, O. Abdala, V. Monasterio, S. Yim-Yeh, A. Malhotra, and G. D. Clifford, "A nonparametric surrogate-based test of significance for T-wave alternans detection," *IEEE Transactions on Biomedical Engineering*, vol. 58, no. 5, pp. 1356–1364, 2011.

[53] H. E. Hering, "Experimentelle studien an säugetieren über das elektrocardiogram," *Zeitschrift für experimentelle Pathologie und Therapie*, no. 7, pp. 363–378, 1909.

[54] T. Lewis, "Notes upon alternation of the heart," *Quart. J. Med*, no. 4, pp. 141–144, 1910.

[55] H. H. Kalter and M. L. Schwartz, "Electrical alternans," *N. Y. State J. Med.*, no. 1, pp. 1164–1166, 1948.

[56] W. W. Hamburger, L. N. Katz, and O. Saphir, "Electrical alternans: A clinical study with a report of two necropsies," *JAMA*, no. 106, pp. 902–905, 1936.

[57] A. Khaustov, S. Nemati, and G. Clifford, "An Open-Source Standard T-Wave Alternans Detector for Benchmarking.," *Computers in Cardiology*, vol. 2008, pp. 509–512, Sep. 2008.

[58] V. Monasterio Bazán, G. Clifford, P. Laguna, and J. P. Martínez, "A multilead scheme based on periodic component analysis for T-wave alternans analysis in the ECG," *Annals of Biomedical Engineering*, vol. 38, pp. 2532–41, Apr. 2010.

[59] J. Nemec, "Nonalternans repolarization variability and arrhythmia - the calcium connection," *Journal of Electrocardiology*, vol. 49, no. 6, pp. 877–882, 2016.

[60] J. Ramirez, M. Orini, D. Tucker, E. Pueyo, and P. Laguna, "Variability of ventricular repolarization dispersion quantified by time-warping the morphology of the T-waves," *IEEE Transactions on Biomedical Engineering*, vol. PP, no. 99, pp. 1–1, 2017.

[61] M. S. Fuller *et al.*, "Estimates of repolarization dispersion from electrocardiographic measurements," *Circulation*, vol. 102, no. 6, pp. 685–691, 2000.

[62] Z. Syed *et al.*, "Abstract 2850: Morphological variability: A new electrocardiographic technique for risk stratification after NSTEACS," *Circulation*, vol. 116, no. Suppl 16, 2015.

[63] Z. Syed, B. Scirica, S. Mohanavelu, D. Morrow, C. Stutz, and J. Guttag, "Association of heart rate turbulence, deceleration capacity, and morphologic variability with sudden cardiac death following non-ST-elevation acute coronary syndrome: Results from the MERLIN-TIMI 36 trial," in *American Heart Association Annual Meeting*, 2010.

[64] Z. Syed, B. Scirica, C. Stultz, and J. Guttag, "Electrocardiographic prediction of arrhythmias," in *2009 36th Annual Computers in Cardiology Conference (CinC)*, Published by Computers in Cardiology, 2009, pp. 741–744, ISBN: 9781424472819.

[65] B. E. Backus *et al.*, "Risk scores for patients with chest pain: Evaluation in the emergency department," *Current Cardiology Reviews*, vol. 7, no. 1, pp. 2–8, Feb. 2011.

[66] P. Sung, Z. Syed, and J. Guttag, "Quantifying morphology changes in time series data with skew," in *2009 IEEE International Conference on Acoustics, Speech and Signal Processing*, IEEE, Apr. 2009, pp. 477–480, ISBN: 978-1-4244-2353-8.

[67] H. Costin, C. Rotariu, and A. Pasarica, "Atrial fibrillation onset prediction using variability of ECG signals," *Proc. of the 8th Int. Symp. on Advanced Topics in Electrical Engineering (ATEE)*, May 2013.

[68] C.-C. Chia, M. Saeed, C. Stultz, J. Guttag, and Z. Syed, "Abstract 18756: Association of morphologic variability with 6-month mortality in a general cohort of intensive care unit patients: Results from the MIMICII database," *Circulation*, vol. 126, no. Suppl 21, 2016.

[69] Z. Syed *et al.*, "Relation of death within 90 days of non-ST-elevation acute coronary syndromes to variability in electrocardiographic morphology," *The American Journal of Cardiology*, vol. 103, no. 3, pp. 307–311, Feb. 2009.

[70] Z. Syed, B. M. Scirica, C. M. Stultz, and J. V. Guttag, "Risk-stratification following acute coronary syndromes using a novel electrocardiographic technique to measure variability in morphology," in *Computers in Cardiology*, vol. 35, IEEE, Sep. 2008, pp. 13–16, ISBN: 1424437067.

[71] B. D. Nearing and R. L. Verrier, "Modified moving average analysis of T-wave alternans to predict ventricular fibrillation with high accuracy," *Journal of Applied Physiology*, vol. 92, no. 2, pp. 541–549, 2002, PMID: 11796662.

[72] C. Lieber and V. Mohsenin, "Cheyne-Stokes respiration in congestive heart failure.," *The Yale Journal of Biology and Medicine*, vol. 65, no. 1, pp. 39–50, 1992.

[73] G. D. Clifford, "Advanced methods and tools for ECG data analysis," in Artech House, 2006, ch. 3 "ECG Statistics, Noise, Artifacts, and Missing Data", pp. 55–99.

[74] R. Bailón, L. Sörnmo, and P. Laguna, "Advanced methods and tools for ECG data analysis," in Artech House, 2006, ch. 8 "ECG-Derived Respiratory Frequency Estimation", pp. 215–244.

[75] S. Nemati, A. Malhotra, and G. D. Clifford, "T-wave alternans patterns during sleep in healthy, cardiac disease and sleep apnea patients," *Journal of Electrocardiology*, vol. 44, pp. 126–30, Dec. 2010.

[76] P. Charlton, T. Bonnici, L. Tarassenko, D. Clifton, R. Beale, and P. J Watkinson, "An assessment of algorithms to estimate respiratory rate from the electrocardiogram and photoplethysmogram," *Physiological measurement*, vol. 37, pp. 610–626, Mar. 2016.

[77] G. D. Clifford, S. Nemati, and R. Sameni, "An artificial vector model for generating abnormal electrocardiographic rhythms," *Physiological Measurement*, vol. 31, no. 5, pp. 595–609, Mar. 2010.

[78] R. Sameni, *OSET: The open-source electrophysiological toolbox. Version 3.14, URL: \NoCaseChange{http://www.oset.ir}*, version 3.14, Accessed: 2017-09-12.

[79] *The veterans health administration's treatment of PTSD and traumatic brain injury among recent combat veterans*, https://www.cbo.gov/publication/42969, Accessed: 2021-09-10.

[80] S. Maguen, E. Madden, T. Neylan, B. Cohen, D. Bertenthal, and K. Seal, "Timing of mental health treatment and PTSD symptom improvement among Iraq and Afghanistan veterans," *Psychiatric Services (Washington, D.C.)*, vol. 65, Aug. 2014.

[81] S. Priebe *et al.*, "Consequences of Untreated Posttraumatic Stress Disorder Following War in Former Yugoslavia: Morbidity, Subjective Quality of Life, and Care Costs," *Croatian Medical Journal*, vol. 50, pp. 465–75, Oct. 2009.

[82] N. Lakusic, K. Fuckar, D. Mahovic Lakusic, D. Cerovec, M. Majsec, and N. Stancin, "Characteristics of heart rate variability in war veterans with post-traumatic stress disorder after myocardial infarction," *Military Medicine*, vol. 172, pp. 1190–3, Nov. 2007.

[83] A. Minassian, M. Geyer, D. Baker, C. Nievergelt, D. O'Connor, and V. Risbrough, "Heart rate variability characteristics in a large group of active-duty marines and relationship to posttraumatic stress," *Psychosomatic Medicine*, vol. 76, May 2014.

[84] B. Lown, R. Verrier, and S. Rabinowitz, "Neural and psychologic mechanisms and the problem of sudden cardiac death," *The American Journal of Cardiology*, vol. 39, no. 6, pp. 890–902, May 1977.

[85] J. Gradus *et al.*, "Associations between stress disorders and cardiovascular disease events in the danish population," *BMJ Open*, vol. 5, e009334, Dec. 2015.

[86] J. Sumner *et al.*, "Trauma exposure and posttraumatic stress disorder symptoms predict onset of cardiovascular events in women," *Circulation*, Jun. 2015.

[87] D. Edmondson, S. Richardson, L. Falzon, K. Davidson, M. Mills, and Y. Neria, "Posttraumatic stress disorder prevalence and risk of recurrence in acute coronary syndrome patients: A meta-analytic review," *PLOS One*, vol. 7, e38915, Jun. 2012.

[88] A. Levine, L. Levine, and T. Levine, "Posttraumatic stress disorder and cardiometabolic disease," *Cardiology*, vol. 127, pp. 1–19, Oct. 2013.

[89] C. Forneris, M. Butterfield, and H. Bosworth, "Physiological arousal among women veterans with and without posttraumatic stress disorder," *Military Medicine*, vol. 169, pp. 307–12, May 2004.

[90] I. Kobayashi, J. Boarts, and D. Delahanty, "Polysomnographically measured sleep abnormalities in PTSD," *Psychophysiology*, vol. 44, pp. 660–9, Aug. 2007.

[91] S. Woodward *et al.*, "Estimating heart rate and RSA from the mattress-recorded kinetocardiogram," *Psychophysiology*, vol. 44, pp. 635–8, Aug. 2007.

[92] A. Cakmak *et al.*, "An unbiased, efficient sleep-wake detection algorithm for a population with sleep disorders: Change point decoder," *Sleep*, Feb. 2020.

[93] A. Bourla, S. Mouchabac, W. El-Hage, and F. Ferreri, "E-PTSD: An overview on how new technologies can improve prediction and assessment of posttraumatic stress disorder (PTSD)," *European Journal of Psychotraumatology*, vol. 9, p. 1 424 448, Dec. 2017.

[94] C. Marmar *et al.*, "Speech-based markers for posttraumatic stress disorder in US veterans," *Depression and Anxiety*, vol. 36, Apr. 2019.

[95] C. Mackersie and N. Calderon-Moultrie, "Autonomic nervous system reactivity during speech repetition tasks: Heart rate variability and skin conductance," *Ear and Hearing*, vol. 37 Suppl 1, 118S–125S, Jul. 2016.

[96] R. Verrier *et al.*, "Microvolt T-wave alternans physiological basis, methods of measurement, and clinical utility-consensus guideline by international society for Holter and noninvasive electrocardiology," *Journal of the American College of Cardiology*, vol. 58, pp. 1309–24, Sep. 2011.

[97] T. Jiang *et al.*, "Toward reduced burden in evidence-based assessment of PTSD: A machine learning study," *Assessment*, vol. 0, no. 0, 2020, PMID: 32762342. eprint: https://doi.org/10.1177/1073191120947797.

[98] S. Wshah, C. Skalka, and M. Price, "Predicting posttraumatic stress disorder risk: A machine learning approach," *JMIR Ment Health*, vol. 6, no. 7, e13946, Jul. 2019.

[99] S. İ. Omurca and E. Ekinci, "An alternative evaluation of post traumatic stress disorder with machine learning methods," in *2015 International Symposium on Innovations in Intelligent SysTems and Applications (INISTA)*, 2015, pp. 1–7.

[100] L. Breiman, J. Friedman, C. J. Stone, and R. A. Olshen, *Classification and Regression Trees*. Boca Raton, Florida, USA: Chapman & Hill/CRC, 1984, ISBN: 9780412048418.

[101] C. R. Marmar *et al.*, "Speech-based markers for posttraumatic stress disorder in US veterans," *Depression and Anxiety*, vol. 36, no. 7, pp. 607–616, 2019. eprint: https://onlinelibrary.wiley.com/doi/pdf/10.1002/da.22890.

[102] K. Schultebraucks, V. Yadav, A. Y. Shalev, G. A. Bonanno, and I. R. Galatzer-Levy, "Deep learning-based classification of posttraumatic stress disorder and depression

following trauma utilizing visual and auditory markers of arousal and mood," *Psychological Medicine*, pp. 1–11, 2020.

[103] A. Kumar *et al.*, "Duration of hypotension before initiation of effective antimicrobial therapy is the critical determinant of survival in human septic shock," *Critical Care Medicine*, vol. 34, no. 6, 2006.

[104] R. Bone, R. Balk, F. Cerra, R. Dellinger, A. Fein, and W. Knaus, "Definitions for sepsis and organ failure and guidelines for the use of innovative therapies in sepsis the ACCP/SCCM consensus conference committee," *American College of Chest Physicians/Society of Critical Care Medicine*, vol. 136, e28, Jan. 1992.

[105] J. Gardner-Thorpe, N. Love, J. Wrightson, S. Walsh, and N. Keeling, "The value of modified early warning score (MEWS) in surgical in-patients: A prospective observational study," *Annals of the Royal College of Surgeons of England*, vol. 88, pp. 571–5, Nov. 2006.

[106] A. E Jones, S. Trzeciak, and J. A Kline, "The sequential organ failure assessment score for predicting outcome in patients with severe sepsis and evidence of hypoperfusion at the time of emergency department presentation," *Critical Care Medicine*, vol. 37, pp. 1649–54, Apr. 2009.

[107] M. Islam, T. Poly, B. Walther, H.-C. Yang, C.-C. Wu, and Y.-C. Li, "Prediction of sepsis patients using machine learning approach: A meta-analysis," *Computer Methods and Programs in Biomedicine*, vol. 170, Dec. 2018.

[108] M. Faisal *et al.*, "Development and external validation of an automated computer-aided risk score for predicting sepsis in emergency medical admissions using the patient's first electronically recorded vital signs and blood test results," *Critical Care Medicine*, vol. 46, p. 1, Jan. 2018.

[109] S. Nemati, A. Holder, F. Razmi, M. Stanley, G. Clifford, and T. Buchman, "An interpretable machine learning model for accurate prediction of sepsis in the ICU," *Critical Care Medicine*, vol. 46, p. 1, Dec. 2017.

[110] L. Mayaud, "Predictive power of heart rate complexity to estimate severity in severe sepsis patients," *Journal of Critical Care*, vol. 28, no. 6, 2013.

[111] F. Wyk, A. Khojandi, A. Mohammed, E. Begoli, R. Davis, and R. Kamaleswaran, "A minimal set of physiomarkers in high frequency real-time physiological data streams predict adult sepsis onset earlier," *International Journal of Medical Informatics*, vol. 122, Dec. 2018.

[112] C. W. Hug, G. D. Clifford, and A. T. Reisner, "Clinician blood pressure documentation of stable intensive care patients: an intelligent archiving agent has a higher as-

sociation with future hypotension," *Critical care medicine*, vol. 39, no. 5, pp. 1006–1014, 2011.

[113] C. L. Diller, M. S. Kelleman, K. G. Kupke, S. C. Quary, L. K. Kochilas, and M. E. Oster, "A modified algorithm for critical congenital heart disease screening using pulse oximetry," *Pediatrics*, vol. 141, no. 5, 2018. eprint: https://pediatrics.aappublications.org/content/141/5/e20174065.full.pdf.

[114] B. L. Stone, "Chapter 38 - hypoxemia," in *Comprehensive Pediatric Hospital Medicine*, L. B. Zaoutis and V. W. Chiang, Eds., Philadelphia: Mosby, 2007, pp. 181–189, ISBN: 978-0-323-03004-5.

[115] E. C Ailes, S. Gilboa, M. Honein, and M. E Oster, "Estimated number of infants detected and missed by critical congenital heart defect screening," *Pediatrics*, vol. 135, May 2015.

[116] C. Peterson *et al.*, "Late detection of critical congenital heart disease among US infants: Estimation of the potential impact of proposed universal screening using pulse oximetry," *JAMA Pediatrics*, vol. 168, no. 4, pp. 361–370, Apr. 2014.

[117] K. Lannering, M. Bartos, and M. Mellander, "Late diagnosis of coarctation despite prenatal ultrasound and postnatal pulse oximetry," *Pediatrics*, vol. 136, no. 2, e406–e412, 2015. eprint: https://pediatrics.aappublications.org/content/136/2/e406.full.pdf.

[118] L. Palmeri *et al.*, "Photoplethysmographic waveform characteristics of newborns with coarctation of the aorta," *Journal of Perinatology*, vol. 37, no. 1, pp. 77–80, Jan. 2017.

[119] S. Goudjil *et al.*, "Noninvasive technique for the diagnosis of patent ductus arteriosus in premature infants by analyzing pulse wave phases on photoplethysmography signals measured in the right hand and the left foot," *PLOS ONE*, vol. 9, no. 6, pp. 1–9, Jun. 2014.

[120] C. R. Amirtharaj *et al.*, "Photoplethysmographic assessment of pulse transit time correlates with echocardiographic measurement of stroke volume in preterm infants with patent ductus arteriosus," *Journal of Perinatology*, vol. 38, no. 9, pp. 1220–1226, Sep. 2018.

[121] L. M. Itu *et al.*, "Non-invasive hemodynamic assessment of aortic coarctation: Validation with in vivo measurements," *Annals of Biomedical Engineering*, vol. 41, Dec. 2012.

[122] J. Nielsen, A. Powell, K. Gauvreau, E. Marcus, A. Prakash, and T. Geva, "Magnetic resonance imaging predictors of coarctation severity," *ACC Current Journal Review*, vol. 14, pp. 66–67, Aug. 2005.

[123] G. Chan, P. Middleton, N. Lovell, and B. Celler, "Extraction of photoplethysmographic waveform variability by lowpass filtering," in *2005 IEEE Engineering in Medicine and Biology 27th Annual Conference*, 2005, pp. 5568–5571.

[124] E. Sharkey *et al.*, "Innovative multi-site photoplethysmography measurement and analysis demonstrating increased arterial stiffness in paediatric heart transplant recipients," *Physiological Measurement*, vol. 39, Aug. 2018.

[125] L. Sierra-Galan, G. Gomez-Garza, R. García-Buen-Abad, L.-C. J, A. Rey-Rodriguez, and L.-H. E, "Cardiovascular magnetic resonance with pharmacological induced stress to evaluate the hemodynamic response of a previously dilated aortic coarctation.," *Society for Cardiovascular Magnetic Resonance*, May 2014, Number: 14-08.

[126] Q. Li, C. Rajagopalan, and G. D. Clifford, "A machine learning approach to multi-level ECG signal quality classification," *Computer Methods and Programs in Biomedicine*, vol. 117, Sep. 2014.

[127] R. L. Verrier, K. Kumar, and B. D. Nearing, "Basis for sudden cardiac death prediction by T-wave alternans from an integrative physiology perspective," *Heart Rhythm*, vol. 3, no. 6, pp. 416–22, 2008.

[128] V. Monasterio Bazán, P. Laguna, and J. P. Martínez, "Multilead analysis of T-wave alternans in the ECG using principal component analysis," *IEEE Transactions on Biomedical Engineering*, vol. 56, pp. 1880–90, Apr. 2009.

[129] P. Chazal, M. O'Dwyer, and R. Reilly, "Automatic classification of heartbeats using ECG morphology and heartbeat interval features," *IEEE Transactions on Biomedical Engineering*, vol. 51, pp. 1196–206, Aug. 2004.

[130] J. P. Martinez, R. Almeida, S. Olmos, A. P. Rocha, and P. Laguna, "A wavelet-based ECG delineator: Evaluation on standard databases," *IEEE Transactions on Biomedical Engineering*, vol. 51, no. 4, pp. 570–581, Apr. 2004.

[131] H. Sakoe and S. Chiba, "Dynamic programming algorithm optimization for spoken word recognition," *IEEE Transactions on Acoustics, Speech, and Signal Processing*, vol. 26, no. 1, pp. 43–49, 1978.

[132] M. J. Lisenby and P. C. Richardson, "The beatquency domain: An unusual application of the fast Fourier transform," *IEEE Transactions on Biomedical Engineering*, vol. BME-24, no. 4, pp. 405–408, Jul. 1977.

[133] J. Sun, A. Reisner, and R. Mark, "A signal abnormality index for arterial blood pressure waveforms," *Computers in Cardiology*, no. 33, pp. 13–16, 2006.

[134] W. Zong, T. Heldt, G. Moody, and R. Mark, "An open-source algorithm to detect onset of arterial blood pressure pulses," vol. 30, Oct. 2003, pp. 259–262, ISBN: 0-7803-8170-X.

[135] L. Ballester *et al.*, "Differences in hypotensive vs. non-hypotensive sepsis management in the emergency department: Door-to-antibiotic time impact on sepsis survival," *Medical Sciences*, vol. 6, p. 91, Oct. 2018.

[136] Q. Zhang, D. Zhou, and X. Zeng, "Highly wearable cuff-less blood pressure and heart rate monitoring with single-arm electrocardiogram and photoplethysmogram signals," *BioMedical Engineering OnLine*, vol. 16, no. 1, 2017.

[137] Q. Li and G. D. Clifford, "Dynamic time warping and machine learning for signal quality assessment of pulsatile signals," *Physiological Measurement*, vol. 33, no. 9, pp. 1491–1501, Aug. 2012.

[138] G. B. Moody, W. E. Muldrow, and R. G. Mark, "A noise stress test for arrhythmia detectors," *Computers in Cardiology*, vol. 11, pp. 381–384, 1984.

[139] K. Brzostowski, "An algorithm for estimating baseline wander based on nonlinear signal processing," in *2016 IEEE 18th International Conference on e-Health Networking, Applications and Services (Healthcom)*, 2016, pp. 1–5.

[140] S. Abbaspour and A. Fallah, "A combination method for electrocardiogram rejection from surface electromyogram," *The Open Biomedical Engineering Journal*, vol. 8, pp. 13–19, Mar. 2014.

[141] L. Sörnmo and P. Laguna, "Chapter 7 - ECG signal processing," in *Bioelectrical Signal Processing in Cardiac and Neurological Applications*, ser. Biomedical Engineering, L. Sörnmo and P. Laguna, Eds., Burlington: Academic Press, 2005, pp. 453–566, ISBN: 978-0-12-437552-9.

[142] L. Sörnmo and P. Laguna, "Chapter 8 - ECG signal processing: Heart rate variability," in *Bioelectrical Signal Processing in Cardiac and Neurological Applications*, ser. Biomedical Engineering, L. Sörnmo and P. Laguna, Eds., Burlington: Academic Press, 2005, pp. 567–631, ISBN: 978-0-12-437552-9.

[143] L. Burattini, W. Zareba, J. P. Couderc, J. A. Konecki, and A. J. Moss, "Optimizing ECG signal sampling frequency for T-wave alternans detection," in *Computers in Cardiology 1998. Vol. 25 (Cat. No.98CH36292)*, Sep. 1998, pp. 721–724.

[144] J. Ben-Arie and K. R. Rao, "Nonorthogonal signal representation by Gaussians and Gabor functions," *IEEE Transactions on Circuits and Systems II: Analog and Digital Signal Processing*, vol. 42, no. 6, pp. 402–413, 1995.

[145] P. E. McSharry, G. D. Clifford, L. Tarassenko, and L. A. Smith, "A dynamical model for generating synthetic electrocardiogram signals," *IEEE Transactions on Biomedical Engineering*, vol. 50, no. 3, pp. 289–294, 2003.

[146] P. Davey, "A new physiological method for heart rate correction of the QT interval," *Heart*, vol. 82, no. 2, pp. 183–186, 1999. eprint: https://heart.bmj.com/content/82/2/183.full.pdf.

[147] J. W. Mason, D. G. Strauss, M. Vaglio, and F. Badilini, "Correction of the QRS duration for heart rate," *Journal of Electrocardiology*, vol. 54, pp. 1–4, 2019.

[148] G. E. Dower, "A lead synthesizer for the Frank system to simulate the standard 12-lead electrocardiogram," *Journal of Electrocardiology*, vol. 1, no. 1, pp. 101–116, 1968.

[149] R. Sameni, G. D. Clifford, C. Jutten, and M. Shamsollahi, "Multichannel ECG and noise modeling: Application to maternal and fetal ECG signals," *EURASIP Journal on Advances in Signal Processing*, vol. 2007, Dec. 2007.

[150] R. Bailón, L. Sörnmo, and P. Laguna, "A robust method for ECG-based estimation of the respiratory frequency during stress testing," *IEEE Transactions on Biomedical Engineering*, vol. 53, pp. 1273–85, Aug. 2006.

[151] R. Bousseljot, D. Kreiseler, and A. Schnabel, "Nutzung der EKG-Signaldatenbank CARDIODAT der PTB über das Internet," *Biomedizinische Technik*, vol. 40, pp. 317–318, Jan. 1995.

[152] A. C. Dornhorst, P. Howard, and G. L. Leathart, "Respiratory variations in blood pressure," *Circulation*, vol. 6, no. 4, pp. 553–558, 1952. eprint: https://www.ahajournals.org/doi/pdf/10.1161/01.CIR.6.4.553.

[153] W. G. Guntheroth, B. C. Morgan, G. L. Mullins, G. A. McGough, and D. G. Breazeale, "Effect of respiration on venous return and stroke volume in cardiac tamponade," *Circulation Research*, vol. 20, no. 4, pp. 381–390, 1967. eprint: https://www.ahajournals.org/doi/pdf/10.1161/01.RES.20.4.381.

[154] *Pulsus Paradoxus & Blood Pressure Measurement*, https://stanfordmedicine25.stanford.edu/the25/bppp.html, Accessed: 2021-07-05.

[155] F. Weathers *et al.*, "The clinician-administered PTSD scale for DSM-5 (CAPS-5): Development and initial psychometric evaluation in military veterans," *Psychological Assessment*, vol. 30, no. 3, pp. 383–395, May 2018.

[156] *Normal Sinus Rhythm database*, "https://www.physionet.org/content/nsrdb/1.0.0/", 1999 (accessed September 3, 2019).

[157] A. Schäfer and K. Kratky, "Estimation of breathing rate from respiratory sinus arrhythmia: Comparison of various methods," *Annals of Biomedical Engineering*, vol. 36, pp. 476–85, Apr. 2008.

[158] W. Karlen, S. Raman, J. M. Ansermino, and G. A. Dumont, "Multiparameter respiratory rate estimation from the photoplethysmogram," *IEEE Transactions on Biomedical Engineering*, vol. 60, no. 7, pp. 1946–1953, 2013.

[159] S. Nemati, A. Malhotra, and G. D. Clifford, "Data fusion for improved respiration rate estimation," *EURASIP J. Adv. Signal Process*, vol. 2010, no. 926305 (2010), Feb. 2010.

[160] A. N. Vest *et al.*, *Physionet Cardiovascular Signal Toolbox*, 2018b.

[161] G. B. Moody, R. G. Mark, A. Zoccola, and S. Mantero, "Derivation of respiratory signals from multilead ECGs," *Computers in Cardiology*, vol. 12, pp. 113–116, 1985.

[162] J. Leino *et al.*, "Combined assessment of heart rate recovery and T-wave alternans during routine exercise testing improves prediction of total and cardiovascular mortality: The Finnish Cardiovascular Study," *Heart Rhythm : the official Journal of the Heart Rhythm Society*, vol. 6, pp. 1765–71, Dec. 2009.

[163] W. Einthoven, G. Fahr, and A. de Waart, "On the direction and manifest size of the variations of potential in the human heart and on the influence of the position of the heart on the form of the electrocardiogram," *American Heart Journal*, vol. 40, no. 2, pp. 163–211, 1950.

[164] A. Bahrami Rad *et al.*, "ECG-based classification of resuscitation cardiac rhythms for retrospective data analysis," *IEEE Transactions on Biomedical Engineering*, vol. PP, Mar. 2017.

[165] J. Sun, A. Reisner, and R. Mark, "A signal abnormality index for arterial blood pressure waveforms," *Computers in Cardiology*, pp. 13–16, Oct. 2006.

[166] R. Mahajan, T. Viangteeravat, and O. Akbilgic, "Improved detection of congestive heart failure via probabilistic symbolic pattern recognition and heart rate variability metrics," *International Journal of Medical Informatics*, vol. 108, pp. 55–63, 2017.

[167] M. Samsudin *et al.*, "A novel heart rate variability based risk prediction model for septic patients presenting to the emergency department," *Medicine*, vol. 97, e10866, Jun. 2018.

[168] W. W. Lai, *Echocardiography in Pediatric and Congenital Heart Disease: From fetus to adult, 2nd Ed.* 101 Station Landing #300, Medford, MA 02155: John Wiley & Sons, Ltd, 2016, p. 928, ISBN: 9781118742440.

[169] R. H. Thiele and M. E. Durieux, "Arterial waveform analysis for the anesthesiologist: Past, present, and future concepts," *Anesthesia & Analgesia*, vol. 113, no. 4, pp. 766–776, 2011.

[170] C. R. Amirtharaj *et al.*, "Photoplethysmographic assessment of pulse transit time correlates with echocardiographic measurement of stroke volume in preterm infants with patent ductus arteriosus," *Journal of Perinatology*, vol. 38, no. 9, pp. 1220–1226, Sep. 2018.

[171] V. Vaccarino *et al.*, "Posttraumatic stress disorder and incidence of coronary heart disease: A twin study," *Journal of the American College of Cardiology*, vol. 62, Jun. 2013.

[172] M. A. Reyna *et al.*, "Will two do? varying dimensions in electrocardiography: The PhysioNet/computing in cardiology challenge 2021.," *Computing in Cardiology 2021*, vol. 48, pp. 1–4,

[173] E. A. P. Alday *et al.*, "Classification of 12-lead ECGs: The PhysioNet/computing in cardiology challenge 2020," *Physiological Measurement*, vol. 41, no. 12, p. 124 003, Jan. 2021.

[174] L. Fu, B. Lu, B. Nie, Z. Peng, H. Liu, and X. Pi, "Hybrid network with attention mechanism for detection and location of myocardial infarction based on 12-lead electrocardiogram signals," *Sensors*, vol. 20, no. 4, 2020.

[175] Z. Zhao *et al.*, "Adaptive lead weighted ResNet trained with different duration signals for classifying 12-lead ECGs," in *2020 Computing in Cardiology*, 2020, pp. 1–4.

[176] A. Mahdi, G. Clifford, and S. Payne, "A model for generating synthetic arterial blood pressure," *Physiological Measurement*, vol. 38, no. 3, 2017.